

Alma Mater Studiorum – Università di Bologna

DOTTORATO DI RICERCA IN INGEGNERIA ELETTROTECNICA

---

Ciclo XXVII

**Settore Concorsuale di afferenza:** 09/E1

**Settore Scientifico disciplinare:** ING-IND/31

ENHANCEMENT OF INDUCTIVE POWER TRANSFER  
WITH FLAT SPIRAL RESONATORS

**Presentata da:** GIOVANNI PUCETTI

**Coordinatore Dottorato**

**Prof. Domenico Casadei**

**Relatore**

**Prof. Ugo Reggiani**

**Correlatore**

**Dott. Ing. Leonardo Sandrolini**

**Esame finale anno 2015**





## **Ringraziamenti**

*Il mio primo ringraziamento lo rivolgo al Prof. Ing. Ugo Reggiani e al Dr. Ing. Leonardo Sandrolini per avermi dato la possibilità di fare il dottorato e per essermi sempre stati vicini in questi ultimi anni: mi avete trasmesso la passione per la ricerca e la cura nei dettagli che mi hanno reso una persona più professionale e attenta dal punto di vista lavorativo.*

*Un sentito ringraziamento va anche al Dr. Chris Stevens per avermi accolto nel suo gruppo di lavoro presso il Department of Engineering Science dell' Università di Oxford e aver contribuito significativamente a farmi ottenere importanti risultati nella mia tesi. Un doveroso ringraziamento lo rivolgo anche al Dr. S. Arvas, Senior Research Engineer presso Sonnet Software, che mi ha gentilmente concesso la possibilità di utilizzare un importante programma utile alle mie ricerche.*

*Desidero infine ringraziare Telecom Italia che ha supportato il mio Dottorato di Ricerca e in particolare il Dr. Valter Bella, il quale si è costantemente dimostrato vicino e interessato al mio lavoro*

# Contents

|   |           |
|---|-----------|
| <b>1. Introduction</b>  | <b>11</b> |
| <b>2. Wireless Power Transfer and Magnetoinductive Waves (MIW)</b>                                  | <b>13</b> |
| 2.1. Circuital analysis between two coupled resonators . . . . .                                    | 13        |
| 2.2. Multiple resonator system . . . . .  | 16        |
| 2.3. MIW: Theoretical background and basic assumptions . . . . .                                    | 17        |
| 2.3.1. Metamaterial with a receiver . . . . .   | 20        |
| 2.3.2. Input and equivalent impedances . . . . .  | 22        |
| <b>3. Transmission Coefficient: experimental analysis of wireless power transfer system</b>         | <b>25</b> |
| 3.1. Numerical modeling and transmission coefficient $S_{21}$ . . . . .                             | 27        |
| 3.1.1. Mutual Inductance Calculation . . . . .  | 29        |
| 3.2. Measurements and comparison with simulations . . . . .   | 31        |
| 3.2.1. Discussion of the results . . . . .  | 33        |
| <b>4. Investigation of Termination Impedance Effects: Experiments and Simulations</b>               | <b>37</b> |
| 4.1. Experimental setup . . . . .   | 37        |
| 4.2. Measurement results . . . . .  | 39        |
| 4.2.1. Measurement at 9mm of distance between metamaterial and receiver (Matching Height) . . . . . | 40        |
| 4.2.2. Comparison with simulations . . . . .  | 45        |
| 4.3. Discussion of the results . . . . .  | 45        |
| <b>5. Design of Metamaterial with Multilayer Flat Spiral Resonators for WPT</b>                     | <b>47</b> |
| 5.1. Modelling of multilayer flat spiral resonator . . . . .  | 47        |
| 5.2. Numerical characterization . . . . .   | 48        |
| 5.2.1. AC Resistance: skin and proximity effects . . . . .  | 49        |
| 5.2.2. Self-Inductance . . . . .  | 52        |
| 5.2.3. Stray capacitance and parallel resistance . . . . .  | 53        |
| 5.3. Sonnet validation . . . . .  | 55        |
| 5.3.1. Results and comparisons . . . . .  | 57        |
| 5.3.2. Discussion of the results . . . . .  | 57        |
| 5.4. Metamaterial modelling . . . . .   | 61        |
| 5.4.1. Investigation on $ kQ $ product . . . . .  | 61        |
| 5.4.2. Matching condition . . . . .   | 63        |

*Contents*

|  |           |
|--|-----------|
| 5.5. Electromagnetic simulations ( $f_0 = 300\text{kHz}$ ) . . . . .                     | 65        |
| 5.5.1. Transmission coefficient and efficiency . . . . .                                 | 66        |
| <b>6. Original Contribution and Conclusions</b>  | <b>71</b> |
| <b>A. Resistance and Self-inductance of Single Layer Solenoid Coil</b>                   | <b>73</b> |
| <b>B. Inductance of Planar Zig-zag Spiral Inductors with Uniform and Nonuniform Arms</b> | <b>83</b> |
| <b>Bibliography</b>  | <b>96</b> |

# List of Figures

|  |    |
|--|----|
| 2.1.1.Circuit topologies for two mutually coupled coils. (a) Parallel-parallel topology. (b) Series-series topology. . . . .   | 14 |
| 2.1.2.Equivalent circuit of the parallel-parallel topology of Figure 2.1.1(a) with compensation sources. . . . .   | 15 |
| 2.1.3.Equivalent circuit of the parallel-parallel topology of Figure 2.1.1(a) seen at the input terminals of the emitter coil. . . . .   | 15 |
| 2.2.1.Equivalent circuit of a system composed of $n$ -coupled resonators. . . . .  | 16 |
| 2.3.1.Metamaterial WPT system composed of $n$ -coupled resonators arranged in a line (a) and its equivalent circuit. . . . .   | 18 |
| 2.3.2.System shown in Figure 2.3.1with a receiver facing the metamaterial. . . . .   | 20 |
| 2.3.3.Equivalent circuit of a system composed of $n$ resonator cells with a receiver (a) and with the impedance $Z_d$ (b). . . . .   | 21 |
| 2.3.4.Equivalent circuit of the WPT in terms of an equivalent impedance $\hat{Z}_{eq}$ . . . . .   | 22 |
| 3.0.1.a) Experimental setup. b) Solenoid coils used as emitter (left) and receiver (right) in transmitted power tests. . . . .   | 26 |
| 3.0.2.Representation of the four arrangements tested: a) I-arrangement, b) II-arrangement, c) III-arrangement and d) IV-arrangement. The receiver coil is moved along the SR array. . . . .  | 28 |
| 3.1.1.Equivalent circuit associated to the experimental system. . . . .  | 29 |
| 3.1.2.Example of mutual inductance between two spiral structur with $N = 2$ . . . . .  | 31 |
| 3.2.1.Measured and calculated transmission coefficient $S_{21}$ as a function of frequency. These trends are for I-arrangement a) and II-arrangement when the receiver coil is facing the SR6. . . . .   | 35 |
| 3.2.2.Measured and calculated peaks of the transmission coefficient $S_{21}$ as a function of the position of the receiver coil for each arrangement of the array of SRs. a) I-arrangement, b) II-arrangement, c) III-arrangement and d) IV-arrangement. . . . . | 36 |
| 4.1.1.Experimental setup. . . . .  | 38 |
| 4.2.1.Transmission coefficient $S_{21}$ as a function of the height of the receiver. The receiver is located on the last cell. . . . .   | 39 |
| 4.2.2.Transmission coefficient $S_{21}$ as a function of the height of the receiver. The receiver is located on the last cell. . . . .   | 40 |
| 4.2.3.Measurements of $S_{21}$ as a function of frequency and receiver position for $Z_T = 0\Omega$ (a), $Z_T = 120\Omega$ (b) and $Z_T \gg 120\Omega$ (c). . . . .  | 41 |

List of Figures

|  |    |
|--|----|
| 4.2.4. Measurements of $S_{21}$ (a) and adjusted efficiency (b) as a function of the receiver position for the termination impedances used and at $f = f_0$ . . . . .  | 42 |
| 4.2.5. $S_{21}$ measured as a function of frequency for all receiver positions facing the I (a), II (b), III (c), IV (d) and V (e) cell. . . . .   | 43 |
| 4.2.6. Comparison of measured and simulated efficiency and efficiency peaks and optimum frequency for $Z_T = 0\Omega$ (a) and (c) and $Z_T = 120\Omega$ , (b) and (d), respectively. . . . .   | 44 |
| 4.3.1. Comparison between simulated envelopes of efficiency and efficiency peaks (a) and optimum frequencies (b). . . . .  | 46 |
| 5.1.1. Examples of single layer and multilayer flat spiral resonators (a) and their quasi-static equivalent circuit (b). . . . .   | 48 |
| 5.2.1. Particular of multilayer flat spiral coil: main geometrical dimensions (drawing not in scale). . . . .  | 50 |
| 5.2.2. Top view of the partition of a flat spiral resonator layer with $N = 3$ . The partition of the three parallel sides with $n_l = 9$ is shown. The facing elements have the same length (a). Current distribution in the partition elements with $l_1 = l_2 = l_3$ (b), $l_4 = l_5 = l_6 = l_7$ (c) and $l_8 = l_9$ (d) simulated with FEMM for a resonator with $N = 3$ , $n = 2$ , $w = 1$ mm, $s = 0.5$ mm, $h = 0.5$ mm and $t_c = 0.05$ mm . . . . . | 51 |
| 5.2.3. P.u.l. resistance as a function of the number of turns for different layer numbers ( $n$ ), distances between layers ( $h$ ) and turns ( $s$ ). In each simulation $w = 1$ mm and $f = 1MHz$ . Comparison between proposed procedure ('x') and Sonnet simulations ('o'). . . . .  | 52 |
| 5.2.4. P.u.l. resistance as a function of the number of turns, for different layer numbers ( $n$ ), distances between layers ( $h$ ) and turns ( $s$ ). In each simulation $w = 1$ mm and $f = 0.25MHz$ . Comparison between proposed procedure ('x') and Sonnet simulations ('o'). . . . .  | 53 |
| 5.2.5. Electrical energy associated to each couple of conductors considered. Cross-sectional view of the windings of a flat spiral resonator with $N = 3$ and $n = 4$ . . . . .  | 54 |
| 5.2.6. Comparison between the quality factors with ( $Q_{Rp}$ ) and without ( $Q_{th}$ ) dielectric losses performed with Sonnet. The simulated spiral resonator has the geometrical dimensions of the resonator $SR_r$ tabulated in Tab. 5.1, with $n = 6$ and $N = 8$ and FR4 insulating layers. The self-resonant frequency $f_0$ is about 3.8 MHz. . . . .   | 55 |
| 5.3.1. Self-inductance of the resonators $SR_s$ (a) and $SR_r$ (b) as a function of the number of turns for different layer numbers. Comparison between the proposed model ('x') and Sonnet simulations ('o'). . . . .   | 56 |
| 5.3.2. Stray capacitance of the resonator $SR_s$ (a) and $SR_r$ (b) as a function of the number of turns for different layer numbers. Comparison between the proposed model ('x') and Sonnet simulations ('o'). . . . .  | 58 |

|        |   |    |
|--------|---|----|
| 5.3.3. | Self-resonant frequency of the resonators $SR_s$ (a) and $SR_r$ (b) as a function of the number of turns for different layer numbers. Comparison between the proposed model ('x') and Sonnet simulations ('o'). . . . . | 59 |
| 5.3.4. | Quality factor of the resonators $SR_s$ (a) and $SR_r$ (b) for different number of layers and turns as a function of frequency. Comparison between the proposed model ('x') and Sonnet simulations ('o'). . . . .       | 60 |
| 5.4.1. | Quality factor as a function of the number of turns for different layer numbers. . . . .  | 62 |
| 5.4.2. | Coupling coefficient as a function of the number of turns for different layer numbers. $ k $ is performed considering two equal resonators spaced 0.1mm. . . . .  | 62 |
| 5.4.3. | $ kQ $ product as a function of the number of turns and layers. . . . .   | 63 |
| 5.4.4. | Lumped equivalent impedance with the first cell in series (a) and parallel (b) resonance. . . . .   | 64 |
| 5.4.5. | $L_{SR}$ and $L_{PR}$ designed with (5.4.4) as a function of source resistance and for different frequencies. . . . .   | 65 |
| 5.5.1. | Metamaterial composed of 5 cell implemented in Sonnet Software. . . . .   | 67 |
| 5.5.2. | Transmission coefficient as a function of frequency when the second port faces the I (a), II (b), III (c), IV (d) and V (e) cell. . . . .   | 68 |
| 5.5.3. | Efficiency at $f_0$ as a function of the second port position. . . . .  | 69 |
|        |   |    |
| A.0.1  | Resistance versus coil radius of single-layer solenoid coils calculated with (A.0.1) and with Flux 2D (frequency of 180 kHz). . . . .   | 75 |
| A.0.2  | Self-inductance versus coil radius of a single-layer solenoid coil calculated according to [1, 2, 3] and with Flux 2D. . . . .  | 77 |
| A.0.3  | Relative error of the analytical calculations of Figure A.0.2 with respect to the calculation with Flux 2D. . . . .   | 78 |
| A.0.4  | Self-inductance versus number of turns of a single-layer solenoid coil calculated according to [1, 2, 3] and with Flux 2D. . . . .  | 79 |
| A.0.5  | Relative error of the analytical calculations of Figure A.0.4 with respect to the calculation with Flux 2D. . . . .   | 80 |
| A.0.6  | Average error of the analytical calculations with respect to Flux 2D for the self-inductance of a single-layer solenoid coil. . . . .   | 81 |
|        |   |    |
| B.0.1  | Planar zig-zag spiral inductor subdivided in $N$ parts. . . . .   | 83 |
| B.0.2  | Particular of a single side with its geometrical dimensions. . . . .  | 84 |
| B.0.3  | Two parallel thin parallelograms b). . . . .  | 84 |
| B.0.4  | Planar zig-zag spiral inductor with its axis. . . . .   | 88 |
| B.0.5  | Configurations of any two filaments of a planar zig-zag spiral inductor. . . . .  | 88 |
| B.0.6  | Samples I to VI of planar zig-zag spiral inductors of Table B.1. . . . .  | 91 |
| B.0.7  | Self-inductance values of the inductors listed in Table B.4. (a) Samples I-IV, (b) Samples V-VIII. . . . .  | 93 |
| B.0.8  | Nonuniform planar zig-zag spiral inductor. (a) Layout (b) Self-inductance as a function of the turn number. . . . .   | 94 |
| B.0.9  | Layout for the mutual inductance calculation between samples VIII and VI. . . . .   | 94 |



# List of Tables

|      |  |    |
|------|--|----|
| 3.1. | Calculated $L_{e(r),cal}$ and measured $L_{e(r),m}$ self-inductance of the emitter and receiver coils with $d = 1$ mm, $s = 0.3$ mm, $N = 2$ and $D = 70$ mm. . . . .  | 26 |
| 3.2. | Self-resonant frequencies $f_{0m}$ measured for each sample of SR with $w = 0.4$ mm, $s = 0.9$ mm, $N = 28$ and $l = 80$ mm. . . . .   | 26 |
| 3.3. | Calculated $L_{SR,cal}$ , $C_{SR,cal}$ and measured $L_{SR,m}$ , $C_{SR,m}$ electrical parameters of the SRs. . . . .  | 27 |
| 3.4. | Comparison between processing time for three different numerical calculations of mutual inductance, $M$ . . . . .  | 32 |
| 3.5. | Values of the measured ( $f_m$ ) and calculated ( $f_{th}$ ) frequencies [MHz] of the $S_{21}$ peaks as a function of the arrangement of the SR array and position of the receiver. . . . .  | 33 |
| 4.1. | Equivalent impedance values, $Z_{eq}$ , and efficiency, $\eta$ , at $f = f_0$ for different receiver positions and conditions calculated with (2.3.16). . . . .  | 42 |
| 5.1. | Main geometrical dimensions of the two flat spiral resonators considered, $SR_s$ and $SR_r$ . . . . .  | 54 |
| 5.2. | Geometrical dimensions of the single cell of the simulated metamaterial. . . . .   | 66 |
| A.1. | Variability intervals of the frequency and geometrical parameters considered in the analysis. . . . .  | 73 |
| A.2. | Calculations and experimental measurements of the emitter and receiver coil resistance (frequency of 180 kHz). . . . .   | 75 |
| A.3. | Self-inductance of emitter and receiver coils calculated and measured. . . . .   | 76 |
| B.1. | Comparison between the total inductance values obtained with (B.0.12), $L_{ZSI}$ , and with experimental measurements, $L_{ZSI,m}$ . . . . .   | 91 |
| B.2. | Comparison between partial self-inductance values of each part of the planar zig-zag spiral inductor obtained with the exact expression (B.0.5), $L_{exact}$ , and approximated with the partial self-inductance of a rectangle, $L_{rectangle}$ . . . . . | 92 |
| B.3. | Partial self-inductance [nH] of parallelograms of different dimensions calculated with (B.0.5) as a function of the angle $\theta$ . . . . .   | 92 |
| B.4. | Comparison between the self-inductance values obtained with the proposed procedure, $L_{ZSI}$ , and with FastHenry, $L_{ZSI,FH}$ . . . . .   | 93 |
| B.5. | Mutual inductance and coupling coefficient values obtained with the proposed procedure for some sample configurations. . . . .   | 93 |



# 1. Introduction

Wireless power transfer (WPT), i.e., the transmission of electrical power without the last cable or wire, has been studied for a long period of time. An extended review of the history is presented in [4]. The origin can be considered Maxwell's "Treatise on Electricity and Magnetism", published in 1873 [5], where he predicted that power could be transmitted from one point to another in free space by means of electromagnetic waves, and Hertz subsequent experiments to validate Maxwell's equations. At the early beginning of the previous century other experiments to transmit electrical power from one point to another without wires were carried out by Tesla, who patented systems for transmitting electrical energy between two coils [6, 7] where resonance was considered. Originally, one purpose was to employ the "*invention on an industrial scale—as, for instance, for lighting distant cities or districts from places where cheap power is obtainable*".

The increasing request for portability in electric and/or electronic appliances, which follows the development of power electronics, has moved the efforts devoted to the original scheme of power transfer over long distances without any carrier medium to the need to supply electrical energy to electric and/or electronic devices wirelessly, i.e., without conductive paths or magnetic structures. Wireless electricity is potentially interesting for a large number and variety of applications: it can be used to recharge batteries in vehicular technology [8], to power and recharge implantable medical devices [9, 10] or Radio-Frequency IDentification (RFID) systems [11], or mobile appliances such as portable computers or mobile phones [12]. In general, the applications can be divided into two main areas: direct wireless powering of stationary or dynamic devices and automatic wireless charging of portable/movable devices. In the former applications power is supplied directly to the electrical devices, whereas in the latter a battery storing energy is necessary. Wireless transmission of electrical energy can be achieved with techniques that can be broadly classified as far field (radiative) and near field (nonradiative). The former class is particularly suitable for transmitting information at low power. High power radiative transfer is in fact undermined by the waste of energy in free space and thus by the low efficiency when omnidirectional antennas are used, and by safety issues and the need for sophisticated tracking systems when directional antennas are used to supply power to mobile objects. The technique which has been recognized so far as the most promising for transmitting power belongs to the class of nonradiative techniques and is based on the magnetic coupling in a resonant system (inductive power transfer). Several applications of this technique have been proposed, which show that a high efficiency in transmission can be achieved; however, the distance of transmission and amount of power are still limited thus restricting the practical applicability of this technique. It has been shown that a higher efficiency can be obtained at a distance of transmission a few times larger than the largest dimension of both objects involved and can be reached with two

## 1. Introduction

resonant coils of the same resonant frequency magnetically coupled [13, 14]. The resonance condition in the coils is essential as the magnetic coupling between two air-core coils is intrinsically weak [15]; it can be obtained by arranging capacitance in series or in parallel with the coil inductance. The exchange of energy (and thus the efficiency) between the coils can in this way be raised, while the dissipation of energy into extraneous off-resonant object is limited. Moreover, high power transmission efficiency can be achieved by introducing intermediate coils between the emitter and receiver coils [16, 17]. There are several advantages that make this technique particularly appealing: absence of conductors and connectors, lower risk of shock hazard, possibility of employment in difficult environmental conditions.

To date, different approaches are used by researchers for analyzing WPT systems: in particular the coupled mode theory (CMT) or the circuit theory (CT) are the most used in order to explain the main topics generally investigated, for example, frequency splitting, impedance matching and optimization design [18, 19, 20, 21, 22]. The first approach is in general suitable for the study of the transmission energy between two resonators (this approach was originally applied in the microwave field) [23]. The CT approach, on the contrary, is widely used by researchers and engineers as it is more straightforward being based on the mutual inductance model [24].

Anyway, in the last years, a novel type of wave propagation has been experimentally and analytically studied, known as magnetoinductive wave (MIW) and supported by magnetic metamaterials [25, 26, 27]. The magnetic metamaterials are, in general, periodic arrays of resonant elements (also called metamaterial cells, composed of L-C series resonant circuits) magnetically coupled each other in different arrangements (planar or axial) and tuned to a common resonant frequency. Usually, metamaterials are used for telecommunication technologies and data transfer systems [28, 29] but very recently prof. C.J. Stevens applied the MIW theory and metamaterials in WPT system, due to their low loss in a wide bandwidth propagation [30, 31].

The aim of this thesis is to develop a depth analysis of the inductive power transfer along a metamaterial composed of cells arranged in a planar configuration, in order to deliver power to a receiver sliding on them. In this way, the problem of the efficiency strongly affected by the weak coupling between emitter and receiver can be obviated, and the distance of transmission can significantly be increased. This study is made using a circuitual approach and the MIW theory, in order to simply explain the behavior of the transmission coefficient and efficiency from the circuitual and experimental point of view. Moreover, flat spiral resonators are used as metamaterial cells, particularly indicated in literature for WPT metamaterials operating at MHz frequencies (5-30 MHz [32, 30, 33]). Finally, this thesis presents a complete electrical characterization of multilayer and multiturn flat spiral resonators and, in particular, it proposes new approach for the resistance calculation through finite element simulations, in order to consider all the high frequency parasitic effects. Multilayer and multiturn flat spiral resonators are studied in order to decrease the operating frequency down to kHz, maintaining small external dimensions and allowing the metamaterials to be supplied by electronic power converters (resonant inverters).

## 2. Wireless Power Transfer and Magnetoinductive Waves (MIW)

The transmission of electrical power is obtained via inductive resonant coupling between two generic coils at least. One coil (emitter coil) is connected to a converter whose output can be ideally represented by a sinusoidal voltage source, whereas the other (receiver coil) is connected to a load. In order to create resonant conditions, the two coils (each represented by a self-inductance  $L$ ) are connected in series or in parallel to capacitors,  $C$ . This type of resonating LC circuit is also briefly called resonator. In both cases, the resonant frequency of the circuits can be calculated with very good accuracy through the following fundamental expression

$$f_o = \frac{1}{\sqrt{LC}} \quad (2.0.1)$$

### 2.1. Circuital analysis between two coupled resonators

In a system composed of two resonators, four topology combinations can be achieved: parallel-parallel, series-series, parallel-series and series-parallel. These topologies have widely been considered in literature [34, 35] to achieve maximum power transmission and efficiency. In [36], parallel-parallel and series-series topologies are accurately studied in order to reduce the system with an equivalent impedance seen from the source.

Assuming a time-harmonic operation with angular frequency  $\omega$ , the Kirchhoff's voltage law for the emitter and receiver coils and for the parallel-parallel topology shown in Figure 2.1.1(a) can be written

$$\hat{V}_1 = R_1 \hat{I}_1 + j\omega L_1 \hat{I}_1 + j\omega M \hat{I}_2, \quad (2.1.1)$$

$$-\hat{V}_2 = R_2 \hat{I}_2 + j\omega L_2 \hat{I}_2 + j\omega M \hat{I}_1 \quad (2.1.2)$$

where  $\hat{V}_1$  is the voltage source,  $\hat{V}_2$  the voltage across the load,  $\hat{I}_1$  and  $\hat{I}_2$  are the currents flowing in the emitter and receiver coils, respectively. The emitter coil is characterized in terms of lumped-circuit parameters by the elements  $R_1$  and  $L_1$  (resistance and self-inductance, respectively), whereas the receiver coil, characterized by the lumped-circuit elements  $R_2$  and  $L_2$ , is terminated into the load  $\hat{Z}_{load}$ . The emitter and receiver coils are parallel compensated with the capacitances  $C_1$  and  $C_2$ , respectively. The magnetic coupling between the two coils is taken into account by the mutual inductance  $M$ . From the equivalent impedance of the capacitive and load branches in parallel we obtain

$$\hat{V}_2 = \hat{Z}_{C,load} \hat{I}_2 \quad (2.1.3)$$

## 2. Wireless Power Transfer and Magnetoinductive Waves (MIW)

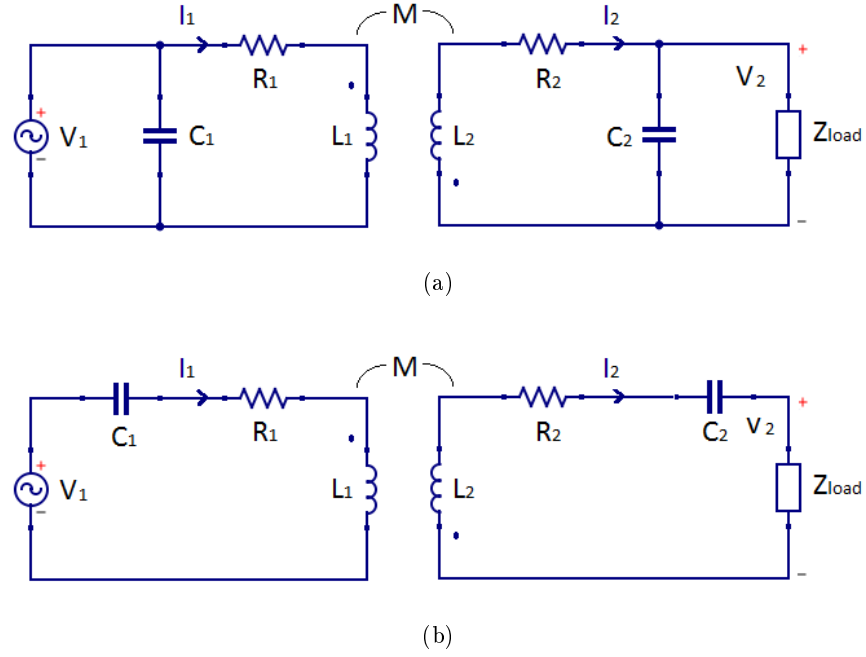


Figure 2.1.1.: Circuit topologies for two mutually coupled coils. (a) Parallel-parallel topology. (b) Series-series topology.

where

$$\hat{Z}_{C,load} = \frac{\hat{Z}_{load}}{1 + j\omega C_2 \hat{Z}_{load}}. \quad (2.1.4)$$

Substituting (2.1.3) into (2.1.2) yields

$$\hat{m} = \frac{-j\omega M}{R_2 + j\omega L_2 + \hat{Z}_{C,load}} = \frac{\hat{I}_2}{\hat{I}_1}. \quad (2.1.5)$$

By using (2.1.5) it is possible to represent the magnetic coupling between the two coils: in fact, substituting (2.1.5) into (2.1.1) gives

$$\hat{V}_1 = R_1 \hat{I}_1 + j\omega L_1 \hat{I}_1 + j\omega M \hat{m} \hat{I}_1 \quad (2.1.6)$$

where  $j\omega M \hat{m}$  represents the contribution to the parallel compensated receiver coil given by the magnetic coupling:

$$j\omega M \hat{m} = j\omega M \frac{-j\omega M}{R_2 + j\omega L_2 + \hat{Z}_{C,load}} = \frac{\omega^2 M^2}{R_2 + j\omega L_2 + \hat{Z}_{C,load}}. \quad (2.1.7)$$

The equivalent circuit for two mutually coupled coils with the compensation source  $j\omega M \hat{m}$  used to represent the effect of mutual inductance is represented in Figure 2.1.2, similarly as in [16].

## 2.1. Circuitual analysis between two coupled resonators

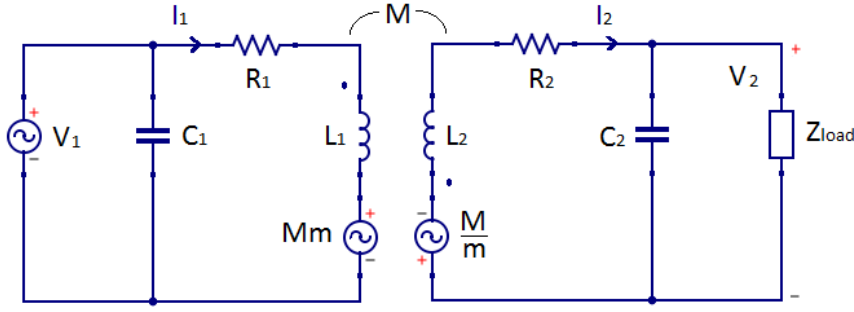


Figure 2.1.2.: Equivalent circuit of the parallel-parallel topology of Figure 2.1.1(a) with compensation sources.

Equation (2.1.5) can be written as

$$\hat{m} \left( R_2 + j\omega L_2 + \hat{Z}_{C,load} \right) = -j\omega M \quad (2.1.8)$$

which substituted in (2.1.6) yields

$$\hat{V}_1 = R_1 \hat{I}_1 + j\omega L_1 \hat{I}_1 - \hat{m}^2 R_2 \hat{I}_1 - j\omega \hat{m}^2 L_2 \hat{I}_1 - \hat{m}^2 \hat{Z}_{C,load} \hat{I}_1 \quad (2.1.9)$$

Equation (2.1.9) can be written as

$$\hat{V}_1 = R_1 \hat{I}_1 + j\omega L_1 \hat{I}_1 + \hat{R}'_2 \hat{I}_1 + j\omega \hat{L}'_2 \hat{I}_1 + \hat{Z}'_{C,load} \hat{I}_1 \quad (2.1.10)$$

where  $\hat{R}'_2 = (-\hat{m}^2)R_2$ ,  $\hat{L}'_2 = (-\hat{m}^2)L_2$ ,  $\hat{Z}'_{C,load} = (-\hat{m}^2)\hat{Z}_{C,load}$ ,  $\hat{C}'_2 = C_2/(-\hat{m}^2)$  and  $\hat{Z}'_{load} = (-\hat{m}^2)Z_{load}$  are the complex parameters of the receiver coil referred to the emitter coil through  $\hat{m}^2$ . Furthermore, from (2.1.3) and (2.1.5), it follows  $\hat{Z}'_{C,load} \hat{I}_1 = (-\hat{m})\hat{V}'_2 = \hat{V}'_2$  where  $\hat{V}'_2$  represents the voltage across the load referred to the emitter coil. The equivalent circuit of the parallel-parallel topology of Figure 2.1.1(a) seen at the input terminals of the emitter coil is depicted in Figure 2.1.3.

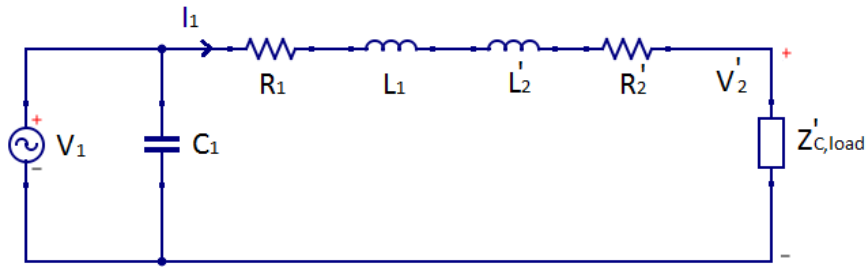


Figure 2.1.3.: Equivalent circuit of the parallel-parallel topology of Figure 2.1.1(a) seen at the input terminals of the emitter coil.

## 2. Wireless Power Transfer and Magnetoinductive Waves (MIW)

In the same way, for the series-series circuit topology of Figure 2.1.1(b), we can write

$$\hat{V}_1 = \frac{\hat{I}_1}{j\omega C_1} + R_1 \hat{I}_1 + j\omega L_1 \hat{I}_1 + j\omega M \hat{I}_2, \quad (2.1.11)$$

$$-\hat{V}_2 = R_2 \hat{I}_2 + j\omega L_2 \hat{I}_2 + j\omega M \hat{I}_1 + \frac{\hat{I}_2}{j\omega C_2} \quad (2.1.12)$$

where the symbols have the same meaning as in the parallel-parallel topology with the exception of the capacitances  $C_1$  and  $C_2$  which represent the series compensation of the two coils. To represent the mutual coupling between the two coils we can use the parameter

$$\hat{m} = \frac{-j\omega M}{R_2 + j\omega L_2 + \hat{Z}_{C,load}} \quad (2.1.13)$$

which is formally equal to (2.1.5); however, in the series-series circuit topology

$$\hat{Z}_{C,load} = \frac{1 + j\omega C_2 \hat{Z}_{load}}{j\omega C_2}. \quad (2.1.14)$$

It is also possible to consider the equivalent circuit at the input terminals of the emitter coil, as previously done for the parallel-parallel circuit topology.

## 2.2. Multiple resonator system

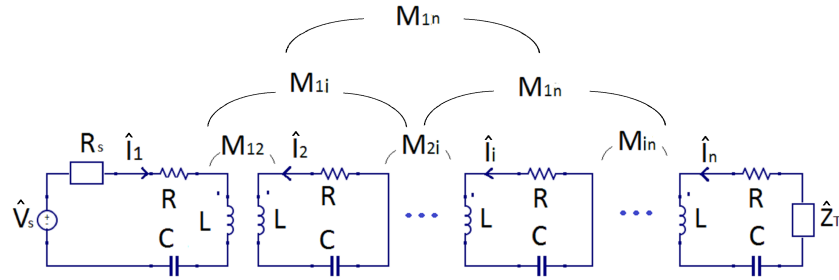


Figure 2.2.1.: Equivalent circuit of a system composed of  $n$ -coupled resonators.

Considering a generic system composed of  $n$ -resonators, as shown in Figure 2.2.1, the circuitual representation is expressed by  $n$ -equation system as follows

$$\begin{aligned} \hat{V} + \hat{Z}_1 \hat{I}_1 + j\omega M_{1,2} \hat{I}_2 + \dots + j\omega M_{1,i} \hat{I}_i + \dots + j\omega M_{1,n} \hat{I}_n &= 0 \\ \hat{Z}_2 \hat{I}_2 + j\omega M_{2,1} \hat{I}_1 + j\omega M_{2,3} \hat{I}_3 + j\omega M_{2,i} \hat{I}_i + \dots + j\omega M_{2,n} \hat{I}_n &= 0 \\ &\vdots \\ \hat{Z}_i \hat{I}_i + j\omega M_{i,1} \hat{I}_1 + j\omega M_{i,2} \hat{I}_2 + \dots + j\omega M_{i,n} \hat{I}_n &= 0 \\ &\vdots \\ (\hat{Z}_n + \hat{Z}_{load}) \hat{I}_n + j\omega M_{n,1} \hat{I}_1 + j\omega M_{n,2} \hat{I}_2 + \dots + j\omega M_{n,i} \hat{I}_i + \dots + j\omega M_{n,n-1} \hat{I}_{n-1} &= 0 \end{aligned} \quad (2.2.1)$$

### 2.3. MIW: Theoretical background and basic assumptions

where  $\hat{V}$  is the voltage source,  $\hat{I}_i$  is the current flowing in the  $i$ th-circuit. The impedance  $\hat{Z}_i = R_i + j\omega L_i + \frac{1}{j\omega C_i}$ , with  $2 < i < n$ , is the impedance of the  $i$ th-resonator, in particular  $R_i, L_i, C_i$  (with  $1 < i < n$ ) represent the resistance, self-inductance and capacitance of the same resonator. The impedance of the first resonator could be different depending on the resonance topology. If the capacitance is connected in parallel to the self-inductance of the first resonator,  $\hat{Z}_1 = (j\omega C_1 + \frac{1}{(R_1 + j\omega L_1)})^{-1}$ . Otherwise,  $\hat{Z}_1 = \hat{Z}_i$  if the capacitance is in series to the resonator. The  $M_{i,j} = M_{j,i}$  (with  $1 < i < n, 1 < j < n$  and  $i \neq j$ ) is the mutual inductance between two generic  $i$  and  $j$  inductors.

The multiple resonator equivalent circuit may be more complex to solve because the mutual inductance between each couple of cells must be taken into account. Hence, the whole system could be easily represented in a matrix form through the following equation:

$$\hat{V} = \hat{Z}\hat{I} \quad (2.2.2)$$

where  $\hat{V} = [\hat{V}_s \ 0 \ \dots \ 0]^T$  with  $\hat{V}_s$  the phasor supply voltage of the emitter coil,  $\hat{I}$  is the complex vector of the current flowing in the cells, and  $\hat{Z}$  is the symmetric matrix of the impedances defined for a  $n$ -cell system as follows

$$\hat{Z} = \begin{bmatrix} R_s + \hat{Z}_1 & j\omega M_{12} & \dots & j\omega M_{1n} & j\omega M_{1r} \\ j\omega M_{21} & \hat{Z}_2 & \dots & j\omega M_{2n} & j\omega M_{2r} \\ \vdots & \vdots & \ddots & \vdots & \vdots \\ j\omega M_{n1} & j\omega M_{n2} & \dots & \hat{Z}_n & j\omega M_{nr} \\ j\omega M_{r1} & j\omega M_{r2} & \dots & j\omega M_{rn} & \hat{Z}_r \end{bmatrix} \quad (2.2.3)$$

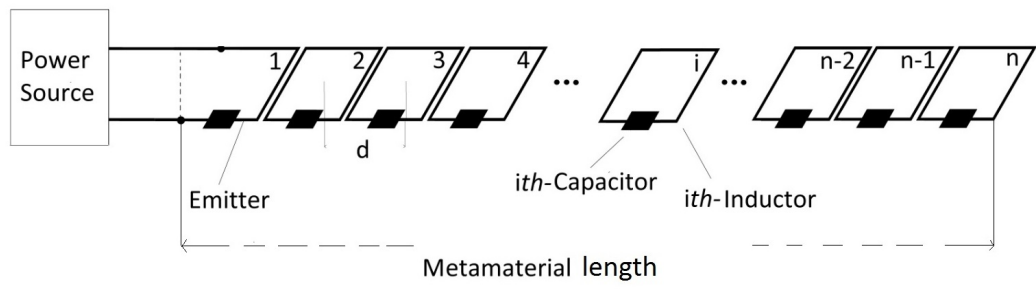
where  $\hat{Z}_i = R_i + j\omega L_i + 1/j\omega C_i$  ( $i = 1, 2, \dots, n$ ) represents the impedance of each inductor and  $\hat{Z}_r = \hat{Z}_n + \hat{Z}_{load}$ .  $M_{ij}$  is the mutual inductance between the cells  $i$  and  $j$ .

### 2.3. MIW: Theoretical background and basic assumptions

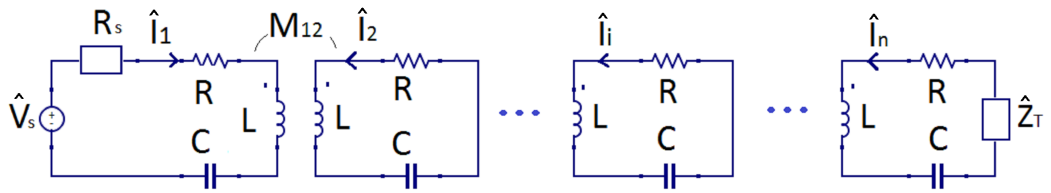
The theory behind the magnetoinductive waves (MIW) has been widely discussed in the literature [25, 37, 26]. In this work, the main considerations for wireless power transfer applications and equivalent circuits are reviewed. Generally, a metamaterial is a periodic array formed by resonator cells (L-C series resonant circuits) coupled to each other magnetically. Considering a system composed of a finite number  $n$  of equal cells as shown in Figure 2.3.1, the associated equivalent circuit is analytically described by the following system of  $n$  equations

$$\begin{aligned} \hat{V}_s + R_s \hat{I}_1 + \hat{Z} \hat{I}_1 + j\omega M_{1,2} \hat{I}_2 &= 0 \\ j\omega M_{2,1} \hat{I}_1 + \hat{Z} \hat{I}_2 + j\omega M_{2,3} \hat{I}_3 &= 0 \\ &\vdots \\ j\omega M_{i,i-1} \hat{I}_{i-1} + \hat{Z} \hat{I}_i + j\omega M_{i,i+1} \hat{I}_{i+1} &= 0 \\ &\vdots \\ j\omega M_{n,n-1} \hat{I}_{n-1} + \hat{Z} \hat{I}_n &= 0 \end{aligned} \quad (2.3.1)$$

2. Wireless Power Transfer and Magnetoinductive Waves (MIW)



(a)



(b)

Figure 2.3.1.: Metamaterial WPT system composed of  $n$ -coupled resonators arranged in a line (a) and its equivalent circuit.

### 2.3. MIW: Theoretical background and basic assumptions

where  $\hat{V}_s$  and  $R_s$  are the voltage source applied to the first inductor and its internal resistance, respectively,  $\hat{I}_i$  the current flowing in the  $i$ th-cell and  $\hat{Z} = R + j\omega L + 1/j\omega C$  is the impedance considered the same for each cells,  $R$  is the AC resistance,  $L$  the self-inductance,  $C$  the capacitance and  $\hat{Z}_T$  is an optional termination impedance connected to the last cell of the line. Hence, each cell is a resonant series L-C circuit tuned to a single resonant frequency

$$f_0 = \frac{1}{2\pi\sqrt{LC}}. \quad (2.3.2)$$

$M_{i,i+1} = M_{i+1,i} = M$  is the mutual inductance between two adjacent resonators. In the equivalent circuit, the mutual inductance between two nonadjacent resonators is neglected. According to the MIW theory, the wave travelling along the metamaterial is expressed in terms of current as

$$\hat{I}_i = I_1 e^{-\hat{\gamma}(i-1)d} \quad (2.3.3)$$

where  $I_1$  is the value of the current flowing in the first cell,  $d$  is the periodic distance between two adjacent cells and  $\hat{\gamma}$  is the propagation constant defined as  $\hat{\gamma} = \alpha + j\beta$ .  $\alpha$  and  $\beta$  are the attenuation and phase constants, respectively, and they could also be expressed in terms of electrical parameters; in particular, it is important to express the attenuation per cell because it represents the wave reduction along the metamaterial

$$\alpha = \frac{1}{d} \sinh^{-1}\left(\frac{1}{kQ}\right) \quad (2.3.4)$$

where  $k = 2M/L$  is the coupling coefficient and  $Q = \omega_0 L/R$  is the quality factor of each inductor. The propagation waves is governed by the following dispersion equation

$$\cos(\beta d) = \left(\frac{\omega_0^2 - \omega^2}{k\omega_0^2}\right) \quad (2.3.5)$$

from which it is possible to find the bandwidth in which the wave propagation is achieved with very low losses [27, 29]

$$\frac{f_0}{\sqrt{1 + \eta k}} \leq f \leq \frac{f_0}{\sqrt{1 - \eta k}} \quad (2.3.6)$$

where  $\eta = 1$  in 1-D structure.

The sign of the mutual inductance  $M$  determines the type of magneto-inductive wave propagation in the array: axial configuration involves forward waves with phase and group velocities in the same direction (given by  $M > 0$ ). On the contrary, planar configuration involves a backward waves with opposite directions of the phase and group velocities (given by  $M < 0$ ).

It is known in literature that the matching condition is achieved introducing a termination impedance in the last cell equal to  $\hat{Z}_T = j\omega M e^{-\hat{\gamma}d}$  (shown in Figure 2.3.1), becoming purely real for  $f = f_0$  and equal to  $Z_T = \omega_0 M$ , as demonstrated in [27, 38]. Under this condition, the no standing wave occurs along the metamaterial and the maximum power can be delivered to the last cell at the resonant frequency. With the termination impedance, the last equation of the system (2.3.1) is modified as follows

$$j\omega M_{n,n-1} \hat{I}_{n-1} + \hat{Z} \hat{I}_n + \hat{Z}_T \hat{I}_n = 0 \quad (2.3.7)$$

## 2. Wireless Power Transfer and Magnetoinductive Waves (MIW)

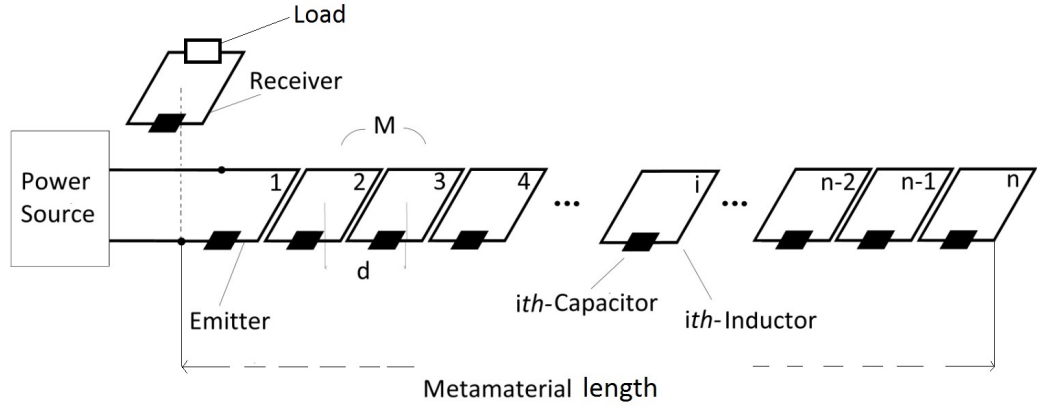


Figure 2.3.2.: System shown in Figure 2.3.1 with a receiver facing the metamaterial.

### 2.3.1. Metamaterial with a receiver

In the following discussion, some assumptions are made in order to simplify the system in (2.3.1):

- All the resonators are equal.  $R_i = R$ ,  $L_i = L$  and  $C_i = C$  for  $1 < i < n$ .
- Only the mutual inductances between adjacent resonators are taken into account and considered equal for any coupled resonators  $M$ .

Consequently, considering a receiver inductor with a load  $R_{load}$  in series and facing the  $i$ th-cell of the metamaterial as shown in Figure 2.3.2, it is enough to add a further equation in (2.3.1) in order to represent the whole system shown in Figure 2.3.3(a)

$$\begin{aligned}
 \hat{V}_s + R_s \hat{I}_1 + \hat{Z} \hat{I}_1 + j\omega M \hat{I}_2 &= 0 \\
 j\omega M \hat{I}_1 + \hat{Z} \hat{I}_2 + j\omega M \hat{I}_3 &= 0 \\
 &\vdots \\
 j\omega M \hat{I}_{i-1} + \hat{Z} \hat{I}_i + j\omega M \hat{I}_{i+1} + j\omega M_{i,r} \hat{I}_r &= 0 \\
 &\vdots \\
 j\omega M \hat{I}_{n-1} + \hat{Z} \hat{I}_n + \hat{Z}_T \hat{I}_n &= 0 \\
 j\omega M_{r,i} \hat{I}_i + \hat{Z}_r \hat{I}_r &= 0
 \end{aligned} \tag{2.3.8}$$

where  $\hat{Z}_r = \hat{Z} + R_{load}$  with the subscript  $r$  identifying the receiver inductor.

The current flowing in the receiver can be expressed as

$$\hat{I}_r = \hat{I}_{n-1} \left( -\frac{j\omega M_{r,i}}{\hat{Z}} \right) \tag{2.3.9}$$

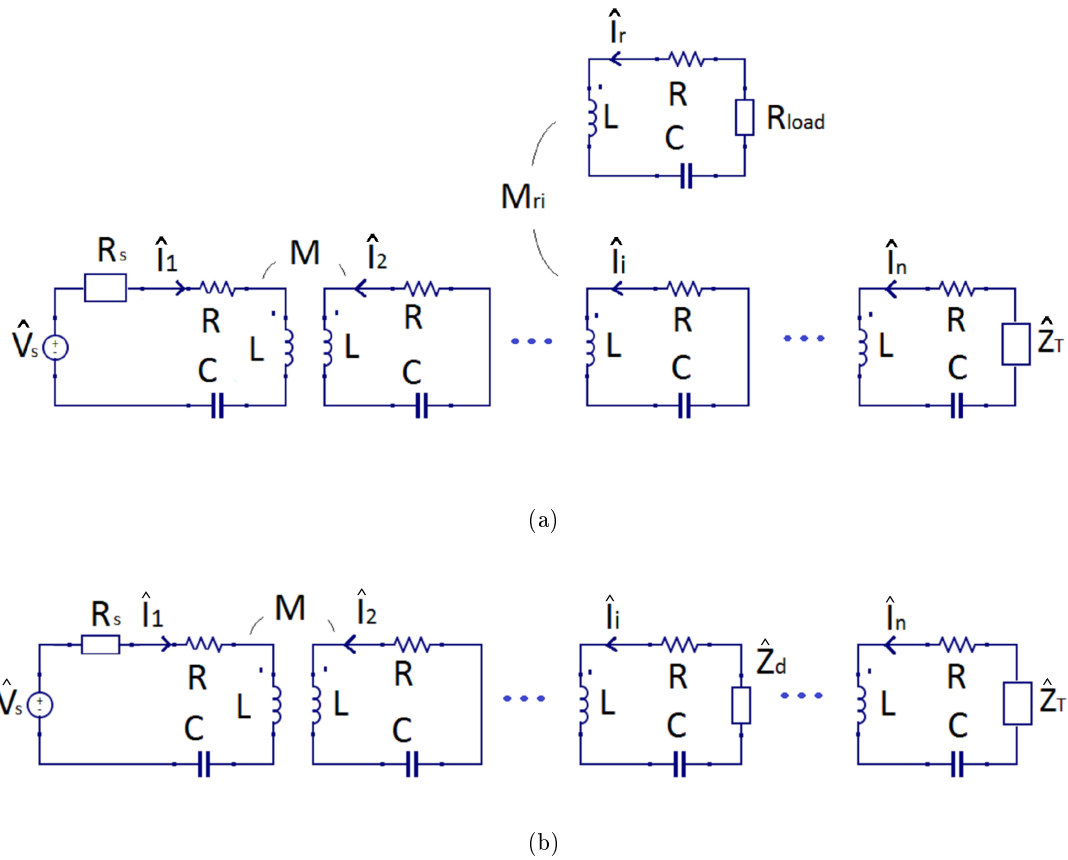


Figure 2.3.3.: Equivalent circuit of a system composed of  $n$  resonator cells with a receiver (a) and with the impedance  $Z_d$  (b).

## 2. Wireless Power Transfer and Magnetoinductive Waves (MIW)

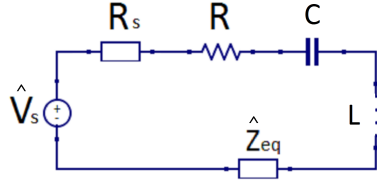


Figure 2.3.4.: Equivalent circuit of the WPT in terms of an equivalent impedance  $\hat{Z}_{eq}$ .

and substituting the (2.3.9) into the  $i$ th-equation of (2.3.8), it is possible to obtain

$$\left(\hat{Z} + \frac{(\omega M_{r,i})^2}{\hat{Z}}\right)\hat{I}_i + j\omega M\hat{I}_{i-1} + j\omega M\hat{I}_{i+1} = 0. \quad (2.3.10)$$

Hence, the receiver impedance seen from the nearest cell can be expressed as an impedance connected in series to the resonator to which facing on, of value

$$\hat{Z}_d = \frac{\omega^2 M_{r,i}^2}{\hat{Z}_r} \quad (2.3.11)$$

and for  $f = f_0$  this impedance is purely real

$$Z_d = \frac{\omega^2 M_{r,i}^2}{R + R_{load}} \quad (2.3.12)$$

The receiver impedance seen from the nearest cell can be expressed as an impedance of value  $\hat{Z}_d = \omega^2 M_{r,i}^2 / \hat{Z}_r$  connected in series to the cell (see Figure 2.3.3(b)). Consequently, the equation of the  $i$ th-cell in (2.3.8) can be written as

$$j\omega M\hat{I}_{i-1} + (\hat{Z} + \hat{Z}_d)\hat{I}_i + j\omega M\hat{I}_{i+1} = 0. \quad (2.3.13)$$

In this sense, it is enough to set

$$\hat{Z}_d = \omega_0 M \quad (2.3.14)$$

in order to obtain the matching condition when the receiver couples to the last cell and avoid a standing wave: this condition can be achieved, for example, by an accurate adjustment of the inductances of the receiver, being  $M_{r,i} = k_{r,i}L$  [38]. However, this does not hold if the receiver inductor moves along the metamaterial as a reflected wave is generated and standing waves result in an extra frequency dependence to the input impedance.

### 2.3.2. Input and equivalent impedances

The multiple resonator system can be simplified with an equivalent impedance  $\hat{Z}_{eq}$ , representing the whole metamaterial and connected in series to the impedance of the first cell, as depicted in Figure 5.4.4.

### 2.3. MIW: Theoretical background and basic assumptions

If the matching condition is satisfied, then  $\hat{Z}_{eq} = \omega_0 M$  [30]. In all the other cases, the equivalent impedance can be also calculated analytically through a continued fraction (as used in [39] for four resonators) whose value depends mainly on the position of the receiver and a possible terminal impedance. For example, considering the receiver located on the third cell of a metamaterial composed of 5 cells and a termination impedance  $\hat{Z}_T$ , the equivalent impedance can be calculated as follows

$$\hat{Z}_{eq} = \frac{(\omega M)^2}{\hat{Z} + \frac{(\omega M)^2}{\hat{Z} + \hat{Z}_d + \frac{(\omega M)^2}{\hat{Z} + \frac{(\omega M)^2}{\hat{Z} + \hat{Z}_T}}} \quad (2.3.15)$$

and for  $f = f_0$

$$\hat{Z}_{eq} = \frac{(\omega_0 M)^2}{R + \frac{(\omega_0 M)^2}{R + Z_d + \frac{(\omega_0 M)^2}{R + \frac{(\omega_0 M)^2}{R + \hat{Z}_T}}} \quad (2.3.16)$$

The input impedance depends on the circuit topology of the cell supplied by source. If the series resonance is achieved in the first cell (as in Figure 5.4.4), the input impedance can be simply calculated as  $\hat{Z}_{in} = R + \hat{Z}_{eq}$  at the resonant frequency. If the parallel topology is used, the input impedance is calculated as  $\hat{Z}_{in}^{-1} = (j\omega C + 1/(j\omega L + R + \hat{Z}_{eq}))^{-1}$



### 3. Transmission Coefficient: experimental analysis of wireless power transfer system

For the analysis of the transmitted power, six identical samples of SR designed to resonate at about 20 MHz were used. Furthermore, two equal solenoid coils were made as emitter and receiver coils. The experimental setup and the coils used as emitter and receiver are shown in Figs. 3.0.1(a) and 3.0.1(b), respectively. The geometrical dimensions of the coils and SRs are indicated in the captions of the Tables 3.1 and 3.2, respectively. As regard the SR dimensions,  $l$  is the external dimension,  $w$  the track width. With respects to the emitter and receiver,  $d$  and  $D$  are the diameters of the turns of the solenoid coil and of the coil, respectively. For both SR and coils,  $s$  and  $N$  are the distance between two adjacent turns and the number of turns of both type of inductor, respectively. The period and the total length of the resonator system were 85 mm and 505 mm, respectively. The emitter and receiver coils were connected to the output and input ports of a Rohde&Schwarz ESRP test receiver 10 Hz - 7 GHz with tracking generator, respectively.

Emitter and receiver coils are designed with the formulas reported in Appendix A, and their calculated electrical parameters  $L_{e(r)}$  are shown and compared with measurements in Table 3.1.

Regarding the single layer flat spiral resonator, the self-inductance and stray capacitance are well discussed in literature both analytically and experimentally [40, 41, 42]. In particular, the formulas used in [43, 44] defining all the electrical parameters as a function of the geometrical dimensions are thoroughly validated and supported by comparisons with measurements in order to optimize the main electrical parameters predicting the self-resonant frequency and quality factor with very good accuracy.

Table 3.2 shows the self-resonant frequencies  $f_{0m}$  measured for each sample of SR and in Table 3.3 the calculated electrical parameters  $L_{cal}$ ,  $C_{cal}$  are compared with measurements,  $L_m$ ,  $C_m$ . The measures of the self-resonant frequencies were performed with the ESRP test receiver. The self-inductances of the SRs and coils were measured with a HP 4192 A impedance analyzer. The value of  $C_m$  is obtained introducing the values of  $L_m$  and  $f_{0m}$  into (2.0.1).

### 3. Transmission Coefficient: experimental analysis of wireless power transfer system



Figure 3.0.1.: a) Experimental setup. b) Solenoid coils used as emitter (left) and receiver (right) in transmitted power tests.

Table 3.1.: Calculated  $L_{e(r),cal}$  and measured  $L_{e(r),m}$  self-inductance of the emitter and receiver coils with  $d = 1$  mm,  $s = 0.3$  mm,  $N = 2$  and  $D = 70$  mm.

| $L_{e(r),cal}$ | $L_{e(r),m}$ |
|----------------|--------------|
| $0.735\mu H$   | $0.76\mu H$  |

Table 3.2.: Self-resonant frequencies  $f_{0m}$  measured for each sample of SR with  $w = 0.4$  mm,  $s = 0.9$  mm,  $N = 28$  and  $l = 80$  mm.

| Sample | $f_{0m}$ [MHz] |
|--------|----------------|
| SR1    | 19.55          |
| SR2    | 19.56          |
| SR3    | 19.52          |
| SR4    | 19.52          |
| SR5    | 19.52          |
| SR6    | 19.3           |

The theoretical self-resonant frequency of the resonators  $f_{0th}$ , calculated introducing  $L_{cal}$  and  $C_{cal}$  in (2.0.1), is 19.4 MHz; the error between the values of the self-resonant frequency calculated and measured is less than 5%. The Q factor of each resonator was estimated about 230 at the resonant frequency.

The experiments were performed in order to analyse the transmission coefficient in an array of resonators and its variation for different arrangements of the array. Hence, four different coplanar combinations were tested maintaining the same number of SRs. The different arrangements considered are shown in Figure 3.0.2. In each test, the distance between two adjacent SRs was 5mm so the coupling coefficient is calculated as  $k = 2M_{cal}/L_{cal} \approx 0.16$ . Furthermore, as the receiver coil is connected to a spectrum analyzer having an input impedance  $R_L = 50\Omega$ , the receiver coil was matched to the structure

### 3.1. Numerical modeling and transmission coefficient $S_{21}$

at its end when it was positioned above the last resonator. This situation was achieved by choosing the distance between the receiver coil and the SR equal to 23 mm so as to satisfy the condition [38]

$$M_{nr} = \sqrt{\frac{M_{cal}}{2\pi f_{0th}} R_L} \quad (3.0.1)$$

The emitter coil was placed at the same distance from the array of resonators. The relevant coupling coefficient is almost  $k_{e(r)1} = M_{r1}/\sqrt{L_r L_{cal}} \approx 0.17$ .

Table 3.3.: Calculated  $L_{SR,cal}$ ,  $C_{SR,cal}$  and measured  $L_{SR,m}$ ,  $C_{SR,m}$  electrical parameters of the SRs.

| $L_{SR,cal}$ | $L_{SR,m}$   | $C_{SR,cal}$ | $C_{SR,m}$     |
|--------------|--------------|--------------|----------------|
| 30 $\mu H$   | 28.9 $\mu H$ | 2.24 $pF$    | 2.28-2.35 $pF$ |

### 3.1. Numerical modeling and transmission coefficient $S_{21}$

If both the period and the total length of the structure are much smaller than the free-space wavelength at the operating frequency, the retarding effects can be neglected and consequently the mutual impedances between two resonators and each resonator and a coil are purely imaginary, i.e., only the mutual inductances, due to magnetic coupling, are effective [45]. Then, if only the emitter coil is supplied, the multiple resonator system can be shown in terms of equivalent electrical circuit as in Figure 3.1.1, numerically represented in matrix form through the following equation:

$$\hat{\mathbf{V}} = \hat{\mathbf{Z}}\hat{\mathbf{I}} \quad (3.1.1)$$

where  $\hat{\mathbf{V}} = [\hat{V}_e \ 0 \ \dots \ 0]^T$  with  $\hat{V}_e$  the phasor supply voltage of the emitter coil,  $\hat{\mathbf{I}}$  is the complex vector of the current flowing in the cells, and  $\hat{\mathbf{Z}}$  is the symmetric matrix of the impedances defined for a  $n$ -cell system as follows

$$\begin{bmatrix} \hat{Z}_e + R_s & j\omega M_{eSR1} & \dots & j\omega M_{eSRn} & j\omega M_{er} \\ j\omega M_{SR1e} & \hat{Z}_{SR1} & \dots & j\omega M_{1SRn} & j\omega M_{SR1r} \\ \vdots & \vdots & \ddots & \vdots & \vdots \\ j\omega M_{SRne} & j\omega M_{nSR1} & \dots & \hat{Z}_{SRn} & j\omega M_{SRnr} \\ j\omega M_{re} & j\omega M_{rSR1} & \dots & j\omega M_{rSRn} & \hat{Z}_r + R_l \end{bmatrix} \quad (3.1.2)$$

where  $\hat{Z}_{e(r)} = R_{e(r)} + j\omega L_{e(r)}$  and  $\hat{Z}_i = R_i + j\omega L_i + 1/j\omega C_i$  represent the impedance of  $i$ th-inductor. In particular, the subscript  $e$  ( $r$ ) identifies the electrical parameter of the emitter (receiver) coil. The emitter and receiver coils are designed with the procedure presented in [46] which allows their electrical parameters to be calculated analytically. The mutual inductances between each couple of inductors in the system are

3. *Transmission Coefficient: experimental analysis of wireless power transfer system*

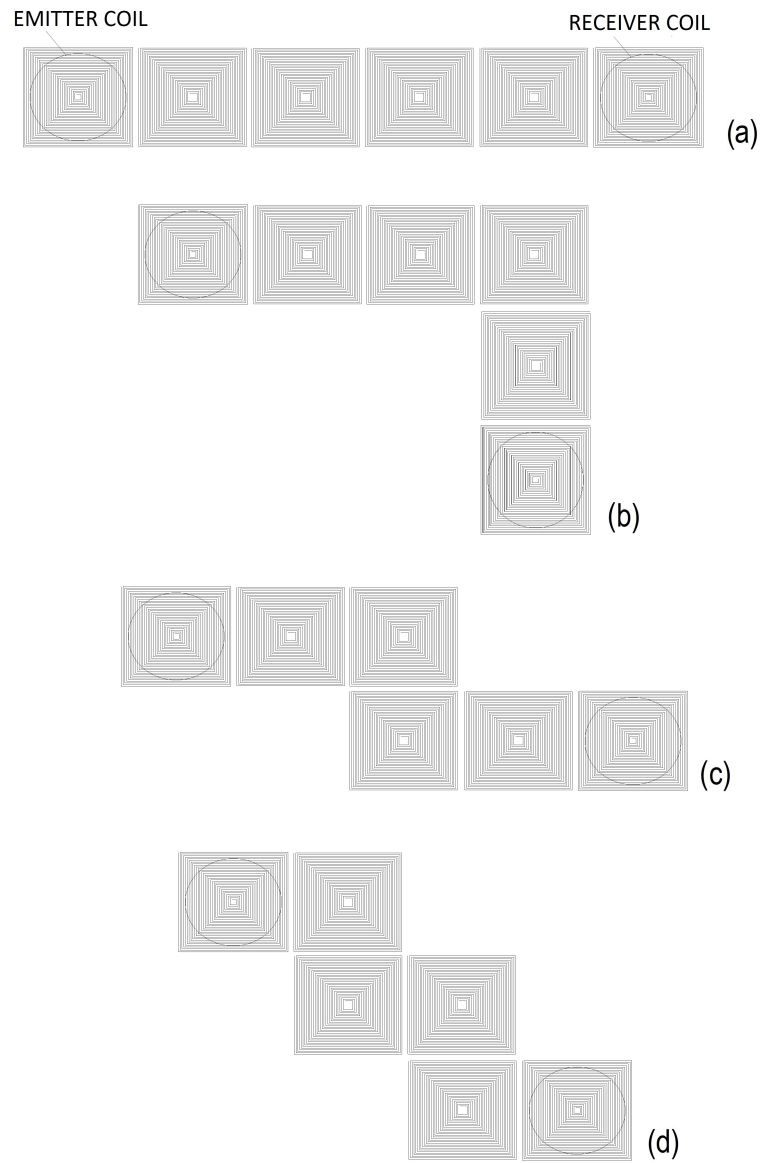


Figure 3.0.2.: Representation of the four arrangements tested: a) I-arrangement, b) II-arrangement, c) III-arrangement and d) IV-arrangement. The receiver coil is moved along the SR array.

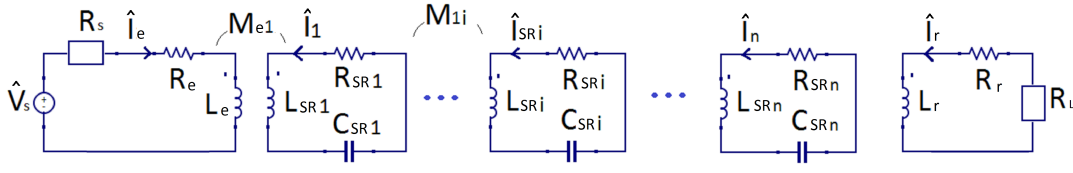


Figure 3.1.1.: Equivalent circuit associated to the experimental system.

calculated with good approximation following the numerical calculation reported in subsection 3.1.1. In this form, the currents circulating in each resonator are calculated inverting the impedance matrix

$$\hat{\mathbf{I}} = \hat{\mathbf{Z}}^{-1} \hat{\mathbf{V}} \quad (3.1.3)$$

In this way, all the electrical dimensions are easily found and the transmission coefficient  $S_{21}$  could be calculated through the following expression [47]

$$S_{21} = 2 \frac{V_l}{V_s} \left( \frac{R_s}{R_l} \right)^{1/2} \quad (3.1.4)$$

### 3.1.1. Mutual Inductance Calculation

This subsection presents the numerical code implemented in Matlab™ programme [48] in order to predict the mutual inductance between two different and general structure (simply filaments or more complex polygons). The method is based on Sonntag et al. work [49] but in this work is improved in terms of computation time.

The mutual inductance is calculated integrating numerically the following flux linkage formula between two filaments:

$$\lambda(i, j) = \frac{\mu_0 I_1}{4\pi} \oint_i \oint_j \frac{di \cdot dj}{|r - r'|} \quad (3.1.5)$$

where  $\mu_0$  is the free space permeability,  $I_1$  the current circulating in the filament considered as primary,  $i$ , and  $j$  the contour of the second filaments.  $|r - r'|$  is the difference between the vector pointing from the axis origin to the respective contour.

Hence, the (3.1.5) becomes numerically

$$\lambda'(i, j) = \frac{\mu_0 I_1}{4\pi} \sum_{\alpha=1}^{a^i} \sum_{\beta=1}^{a^j} \sum_{\chi=0}^X \sum_{\varepsilon=0}^E \frac{n_{\alpha}^i \cdot n_{\beta}^j}{|K_{\chi} - K_{\varepsilon}|} \quad (3.1.6)$$

where

$$K_{\chi} = q_{\alpha}^i + (\chi)(\Delta_i) n_{\alpha}^i \quad (3.1.7)$$

$$K_{\varepsilon} = q_{\beta}^j + (\chi)(\Delta_j) n_{\beta}^j \quad (3.1.8)$$

### 3. Transmission Coefficient: experimental analysis of wireless power transfer system

$$X = \frac{c_\alpha^i}{\Delta_i}, \quad E = \frac{c_\beta^j}{\Delta_j}$$

In particular,  $\Delta_i$  and  $\Delta_j$  are the small integration elements,  $n_m^i$  and  $n_m^j$  are the normalized position vectors for the respective structure filaments identified by the peaks  $i$  and  $j$ , respectively and defined as

$$n_m^{i,j} = \frac{q_{m+1}^{i,j} - q_{l,k}^{i,j}}{c_m^{i,j}}, \quad m \in [1 \dots a^{i,j}]$$

$c^{i,j}$  is the Euclidean length,  $q^{i,j}$  is the vector containing all the coordinate vertices.  $a^{i,j}$  is the amount of the sides of the structure (hence the number of vertices is  $b^{i,j} = a^{i,j} + 1$ ).

Once calculated the flux (3.1.6), the partial mutual inductance is obtained simply dividing for the current  $I_1$ .

$$M_{p,i,j} = \frac{\mathcal{X}(i,j)}{I_1} \quad (3.1.9)$$

## Modifications added

The numerical calculation (3.1.6) can be affected by the processing time for accurate integration, choosing  $\Delta_i$  and  $\Delta_j$  very small. Four summations are needed for the flux linkage between the two structures calculation:  $X$  and  $E$  depend only on the length of each side and integration element,  $a^i$  and  $a^j$  on the number of structure sides.

- Elimination of the calculation of perpendicular sides. As the mutual inductance between two perpendicular filaments is equal to  $M_{ij\perp} = 0$ , a further matrix,  $\beta_{test}$ , containing the number of non-perpendicular elements respect to  $\alpha$  value is added in the code. In this way, only the  $M_{ij} \neq 0$  are taken into account.

For example, considering two spiral structures with  $N = 2$  and with a generic distance  $g$  and length  $l$ , as in Figure 3.1.2  $\beta_t$  is equal to

$$\beta_t = \begin{bmatrix} 1 & 2 & 1 & 2 & 1 & 2 & 1 & 2 \\ 3 & 4 & 3 & 4 & 3 & 4 & 3 & 4 \\ 5 & 6 & 5 & 6 & 5 & 6 & 5 & 6 \\ 7 & 8 & 7 & 8 & 7 & 8 & 7 & 8 \end{bmatrix} \quad (3.1.10)$$

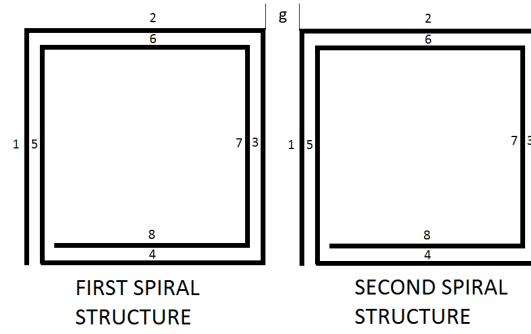


Figure 3.1.2.: Example of mutual inductance between two spiral structures with  $N = 2$ .

hence if  $\alpha = 1$ ,  $\beta = 1, 3, 5, 7$ : it means that only the mutual between the first side of the first structure and 1, 3, 5, 7 sides of the second structure are calculated. Then,  $\alpha = 2$  so  $\beta = 2, 4, 6, 8$  because only the mutual inductances between the second side of the first structure and 2, 4, 6, 8 sides of the second structure exist. When  $\alpha = 3$ ,  $\beta = 1, 3, 5, 7$  and so on.

- parallel processing. A parallel for-loops is implemented for running task-parallel algorithms on multiple processors.

## Results

The following table shows the processing time needed to calculate the mutual inductance between generic structures performed with 3 different numerical code:

- Numerical calculation proposed by Sonntag et al. ( $Mutual_{Sonntag}$ );
- Mutual with only  $\beta_t$  modification ( $Mutual_{\beta_{test}}$ );
- Mutual with  $\beta_t$  modification and parallel processing ( $Mutual_{\beta_t-par}$ ).

In each simulation the track width is equal to the spacing ( $w = s = 1mm$ ), track thickness and distance between layers,  $t_c$  and  $h$ , are 0.1mm, and the distance between structures is  $g = 0.5mm$ .  $\Delta_l = \Delta_k = 0.85w$ .

## 3.2. Measurements and comparison with simulations

The analysis of the transmission coefficient  $S_{21}$  was developed comparing experimental measurements with analytically predicted results obtained with a Scilab computer code [50]. The matrix of impedances (3.1.2) becomes as follows

### 3. Transmission Coefficient: experimental analysis of wireless power transfer system

Table 3.4.: Comparison between processing time for three different numerical calculations of mutual inductance,  $M$ .

| $l$ [mm] | $N$ | $n$ | $Mutual_{Sonntag}$ [s] | $Mutual_{\beta_t}$ [s] | $Mutual_{\beta_t-par}$ [s] | $M$ [ $\mu$ H] |
|----------|-----|-----|------------------------|------------------------|----------------------------|----------------|
| 40       | 4   | 1   | 9.3                    | 4.3                    | 2.1                        | -0.073         |
| 80       | 4   | 1   | 43.2                   | 20                     | 6.3                        | -0.28          |
| 40       | 4   | 2   | 43.2                   | 20                     | 7.7                        | -0.34          |
| 80       | 2   | 4   | 291.6                  | 135.15                 | 39.7                       | -2.45          |

$$\begin{bmatrix}
 \hat{Z}_e & j\omega M_{eSR1} & \dots & j\omega M_{eSR3} & \dots & j\omega M_{eSR5} & \dots & j\omega M_{er} \\
 j\omega M_{SR1e} & \hat{Z}_{SR1} & \dots & j\omega M_{SR13} & \dots & j\omega M_{SR15} & \dots & j\omega M_{SR1r} \\
 \vdots & \vdots & \ddots & \dots & \ddots & \vdots & \ddots & \vdots \\
 j\omega M_{SR3e} & j\omega M_{SR31} & \dots & \hat{Z}_{SR3} & \dots & j\omega M_{SR35} & \dots & j\omega M_{SR3r} \\
 \vdots & \vdots & \ddots & \vdots & \ddots & \vdots & \ddots & \vdots \\
 j\omega M_{SR5e} & j\omega M_{SR51} & \dots & j\omega M_{SR53} & \dots & \hat{Z}_{SR5} & \dots & j\omega M_{SR5r} \\
 \vdots & \vdots & \ddots & \vdots & \ddots & \vdots & \ddots & \vdots \\
 j\omega M_{re} & j\omega M_{rSR1} & \dots & j\omega M_{rSR3} & \dots & j\omega M_{rSR5} & \dots & \hat{Z}_r
 \end{bmatrix} \quad (3.2.1)$$

Clearly, the values of the mutual inductances depend on the type of the system under test. Solving (3.1.3) with the impedance matrix given by (3.2.1), it is possible to obtain the current  $I_r$  in the receiver coil and so the transmitted power  $50I_r^2$ , being  $50\Omega$  the input impedance of the spectrum analyzer to which the receiver coil was connected.

In Figs. 3.2.1, the transmission coefficient  $S_{21}$  as a function of frequency for the arrangements I and II is shown. As in each test the emitter coil is fixed in front of SR1, the results depend on the position of the receiver coil and the arrangement of the resonators under consideration. If the measured patterns are compared with the analytically predicted ones, the trends are in agreement in particular under resonance condition. These results are performed for the distance of 23 mm between the receiver coil and the array that realizes the matching condition.

Figure 3.2.2 shows the peaks of the transmission coefficient  $S_{21}$  for each arrangement of the resonators and position of the receiver coil for the distance of 23 mm. In particular, with reference to the calculated values, the  $S_{21}$  peak is higher when there is a direct coupling between the emitter and the receiver coil located above SR2. A general decay of the  $S_{21}$  peaks occur moving the receiver coil along the SR array as the mismatching of the system generates standing waves. After a minimum value is reached, the  $S_{21}$  peak increases and a new maximum value is obtained on top of SR6. Moreover, the system has a low efficiency (between about 20% and 35%) due to the weak magnetic coupling between the resonators. However, considering each arrangement of the array, it can be noticed that the calculated values of the peaks vary in a narrow range. The results obtained are corroborated by the results of the simulations presented in [30]. The

### 3.2. Measurements and comparison with simulations

Table 3.5.: Values of the measured ( $f_m$ ) and calculated ( $f_{th}$ ) frequencies [MHz] of the  $S_{21}$  peaks as a function of the arrangement of the SR array and position of the receiver.

| Receiver | I     |          | II    |          | III   |          | IV    |          |
|----------|-------|----------|-------|----------|-------|----------|-------|----------|
|          | $f_m$ | $f_{th}$ | $f_m$ | $f_{th}$ | $f_m$ | $f_{th}$ | $f_m$ | $f_{th}$ |
| SR2      | 19.4  | 20.7     | 19.3  | 20       | 19.3  | 20       | 19.3  | 20       |
| SR3      | 19.9  | 19.7     | 19.8  | 19.7     | 19.8  | 19.7     | 19.7  | 19.6     |
| SR4      | 19.7  | 20.5     | 19.4  | 20.6     | 19.6  | 19.2     | 19.3  | 19       |
| SR5      | 19.3  | 20.2     | 19.3  | 20.2     | 20.2  | 20.1     | 20.2  | 19       |
| SR6      | 20    | 19.6     | 19.8  | 19.6     | 19.9  | 19.6     | 19.8  | 19.5     |

measurements of the  $S_{21}$  peaks show a similar trend to the calculations with a minimum along the array although the difference between measured and calculated values increases approaching the end of the array. This difference in the trends may be related to the different resistance values of the SRs due to imperfections determined by the fabrication process. Further investigations are needed on this point.

In Table 3.5, all the values of the measured ( $f_m$ ) and calculated ( $f_{th}$ ) frequencies of the  $S_{21}$  peaks are reported. It is important to observe that both the measured and calculated values of the frequencies at which the peaks occur are slightly different due to standing waves which arise when the receiver coil is not above SR6 in matching condition. Anyway, the values of the peak frequencies are similar for each receiver position, regardless of the type of arrangement. It can be noted that the theoretical frequencies when the receiver coil is on the top of the SR6 are nearly coincident regardless of the arrangement; the same result is obtained in the experiments, thus showing that an adequate matching condition was achieved that can be obtained with the same formula used for the partial mutual inductance calculation.  $C_i$  is the total capacitance in series to the self-inductance of each cell considering both the stray,  $C_p$ , and the lumped capacitances added,  $C_{add}$ , to tune the resonance condition ( $\omega_0 = 1/\sqrt{L(C_p + C_{add})}$ )

#### 3.2.1. Discussion of the results

A theoretical and experimental analysis of wireless power transfer through an array of coplanar resonators is presented in this work. In particular, six identical SRs were used to form an array and transfer power between an emitter and a receiver. The spiral resonators are designed to resonate at about 20 MHz. Hence, the transmission coefficient is measured for four different arrangements having the same number of resonators and the experimental results are compared with the theoretical predictions, obtaining an analogous behaviour with differences that may be related to the resistance values of the SRs, which depend on the fabrication process. The values of the transmission coefficient peaks vary slightly for the considered SR arrangements. About the system efficiency,

### *3. Transmission Coefficient: experimental analysis of wireless power transfer system*

some considerations are made. First of all, the transmitted power of the system is affected by the weak coupling strength between SRs and between SR and coils. This lack can be reduced by using other configurations (for example axial) or other type of resonators, as shown in [27]. On the other hand, the efficiency along the SR structure is also reduced by the matching condition which is obtained in the last position of the array only. It is possible to improve the efficiency mainly increasing the coupling strength between the receiver coil and SR array so that most power is transmitted. Optimizing the system presented can allow the wireless charging of consumer electronic devices regardless of the receiver position and the arrangement of the SR array.

### 3.2. Measurements and comparison with simulations

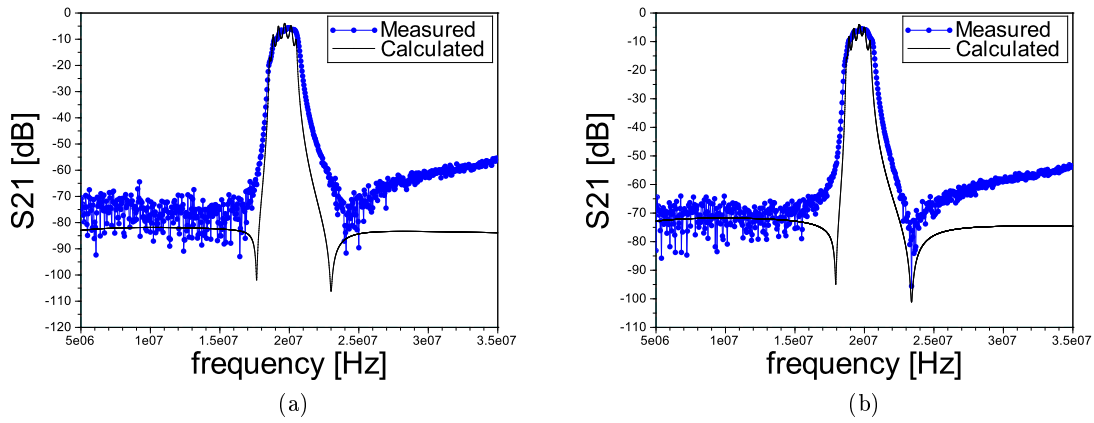


Figure 3.2.1.: Measured and calculated transmission coefficient  $S_{21}$  as a function of frequency. These trends are for I-arrangement a) and II-arrangement when the receiver coil is facing the SR6.

### 3. Transmission Coefficient: experimental analysis of wireless power transfer system

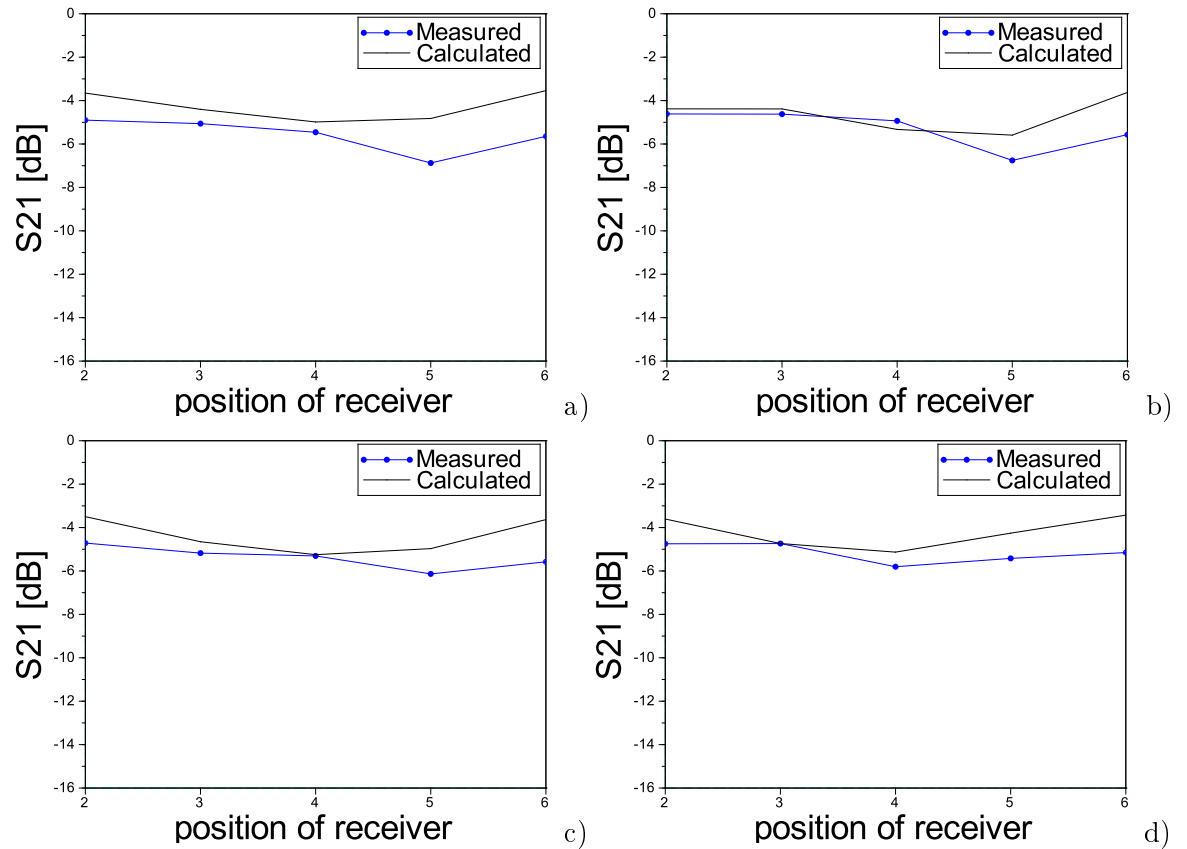


Figure 3.2.2.: Measured and calculated peaks of the transmission coefficient  $S_{21}$  as a function of the position of the receiver coil for each arrangement of the array of SRs. a) I-arrangement, b) II-arrangement, c) III-arrangement and d) IV-arrangement.

## 4. Investigation of Termination Impedance Effects: Experiments and Simulations

In a previous work, C.J. Stevens showed that the efficiency can be improved along a metamaterial line, as depicted in Figure 2.3.2, with the introduction of a termination impedance connected to the last cell whose value depends on the receiver position [31]. This work extends the considerations in [31] with an accurate investigation of the effects of the termination impedance on the transmitted power and efficiency as a function of frequency and receiver position. Moreover, efficiency peaks are discussed in this Chapter. Finally, a numerical characterization is also shown in order to predict with good accuracy the performance of the system analyzed.

### 4.1. Experimental setup

The metamaterial used in this work consists of five equal resonators of square shape mutually coupled and arranged in a planar line separated by gaps equal to  $g = 0.2\text{mm}$ . The experimental system is shown in Figure 4.1.1.

The single metamaterial cell is fabricated with a printed circuit board (PCB) with  $N = 1$ ,  $l = 40\text{mm}$ ,  $w = 1\text{mm}$  and  $s = 1\text{mm}$ . The value of the measured self-inductance is  $0.135\mu\text{H}$ , equal to the numerically calculated one. The mutual inductance between two cells is calculated from measurement by resonance splitting and it is found equal to  $-16.3\text{nH}$  (very close to the predicted one  $-18.7\text{nH}$ ). As the stray capacitance is small, a lumped capacitance equal to  $1\text{nF}$  is added to each cell in order to tune the resonant frequency to  $f_0 = 13.56\text{MHz}$  (as it is a license free ISM band). All the capacitances are parallel to the inductors. The source is connected in series as in Figure 2.3.1. Finally, the measured and calculated AC resistances are equal to  $0.303\Omega$  and  $0.152\Omega$ , respectively. The measured AC resistance includes also the solder connections and series resistance of the lumped capacitances plus any radiation losses. The layout of the receiver resonator used in these tests is identical to the cells of the metamaterial: a load resistance ( $R_{load} = 3.3\Omega$ ) is soldered in series to the lumped capacitance of  $1\text{nF}$ . In case the emitter and receiver coils are single-layer solenoid or single-layer spiral coils, they can be designed with the procedure presented in [46].

An HP 8753 vector network analyzer (VNA) was used in order to supply the source and measure the transmission coefficient  $S_{21}$ : the instrument output is connected to the first cell and the received signal is measured across the load resistance. This type of circuitual connection involves an adjustment of the transmitted power measured as the

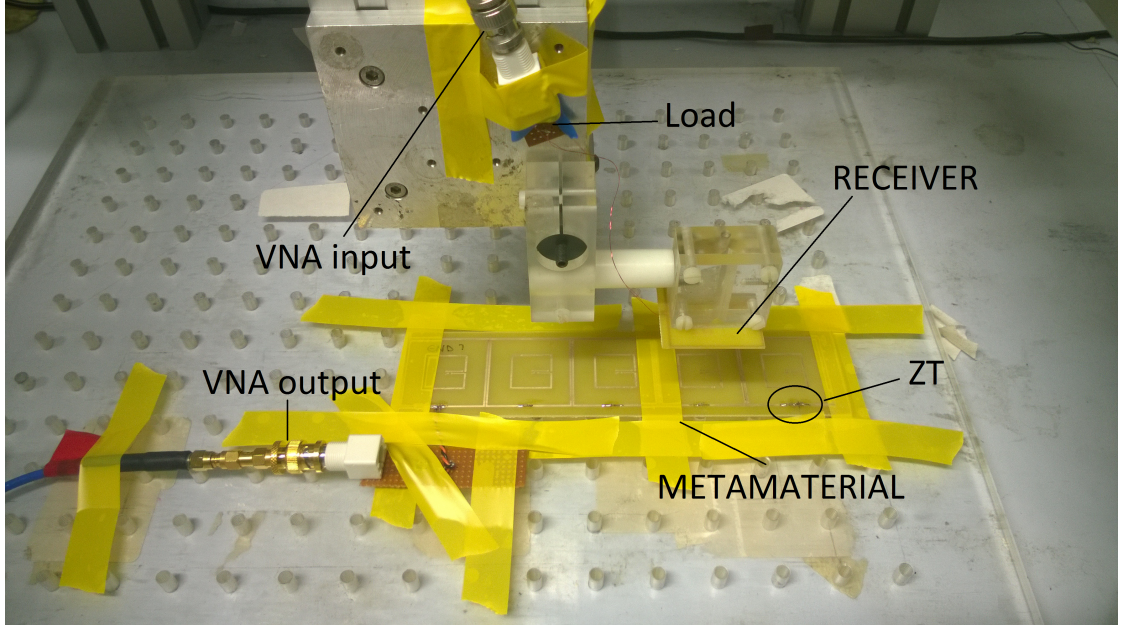


Figure 4.1.1.: Experimental setup.

internal impedance of the VNA is equal to  $Z_0 = 50\Omega$ , quite different from  $R_{load}$ . Hence, the measured value is smaller than the real one, consequently it is possible to adjust the measure and find the effective efficiency across the load through

$$\eta = \frac{S_{21}^2(1 + Z_0/R_{load})}{1 - S_{11}^2}. \quad (4.1.1)$$

In the efficiency calculation, the error considered is  $\pm 2.5$  dB for both  $S_{21}$  and  $S_{11}$  measurements given by the sum of the accuracy of the network analyzer output and input characteristics assumed equal to  $\pm 1$  dB, respectively, and Transmission/Reflection Test Set (Agilent HP 85044A 300kHz to 3GHz) equal to  $\pm 1.5$  dB. The error bars are calculated by the combined uncertainty  $u_c(y)$ , as suggested by the GUM guide (Guide to the expression of Uncertainty Measurement) [51], using the following formula

$$u_c(y) = \sqrt{\sum_{i=1}^n \left(\frac{\partial f}{\partial x_i}\right)^2 u^2(x_i) + 2 \sum_{i=1}^{n-1} \sum_{j=i+1}^n \left(\frac{\partial f}{\partial x_i}\right) \left(\frac{\partial f}{\partial x_j}\right) u(x_i) u(x_j) r(x_i, x_j)} \quad (4.1.2)$$

where  $y = f(x_1, x_2, \dots, x_n)$  is the value of the measure given by the  $n$  measured quantities  $(x_1, x_2, \dots, x_n)$ ,  $u(x_i, x_j) = u(x_j, x_i)$  is the covariance between  $x_i$  and  $x_j$ .  $r(x_i, x_j)$  is a correlation coefficient whose value varies between 0 (if the measurements are independent on each other) and 1 (if the measurements are dependent on each other).

Finally, according to the instrument specifications, the frequency measurement uncertainty is 10 ppm and therefore we chose not to take it into account

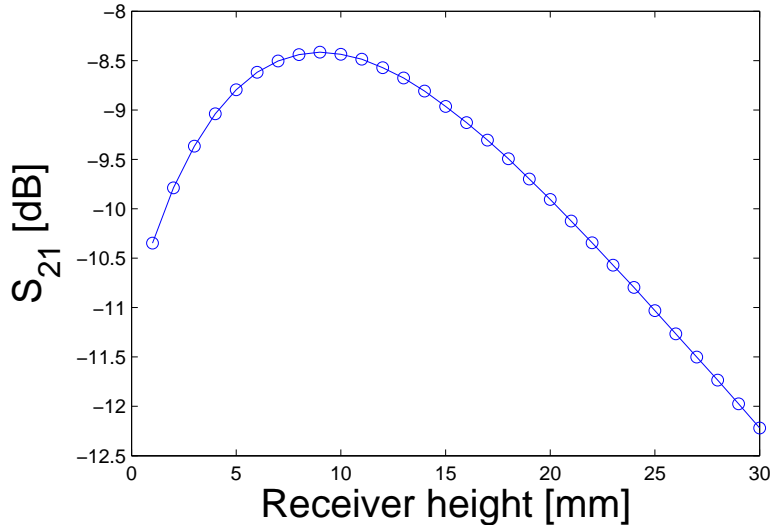


Figure 4.2.1.: Transmission coefficient  $S_{21}$  as a function of the height of the receiver. The receiver is located on the last cell.

## 4.2. Measurement results

The measurements are made for receiver heights from the metamaterial included between 1mm (“ground height”) and 31mm (“top height”). All the measurements are made without termination impedance. Considering the receiver perfectly faced to the last cell, the matching condition can be experimentally found by the transmission coefficient measurements at the resonant frequency and varying the receiver height from ground to top ones (shown in Figure 4.2.1). As it can be noticed, the maximum power is delivered when the receiver is located at about 9mm meaning that the matching condition is verified for this height (“matching height”). In Figure 4.2.2, the transmission coefficient as a function of receiver position is plotted for ground, matching and top heights at the resonant frequency. It is evident by the Figure that all the curves present similar trends: in fact, all the behaviour of  $S_{21}$  alternates highs and lows and the peaks are located every two cells where the maximum of the transmission coefficient is achieved when the receiver faces the I, III and V resonator (cell centres at 20, 100 and 180mm). Furthermore, for the matching height, the values transmission coefficient are almost similar to the ground height ones. However, it is important to noticed that for 9mm  $S_{21}$  is larger than that for 1mm when the receiver is perfectly located on the I, III and V suggesting that the system is well matched. Otherwise, the transmission coefficient related to the top height is clearly lower than the ground and the matching ones.

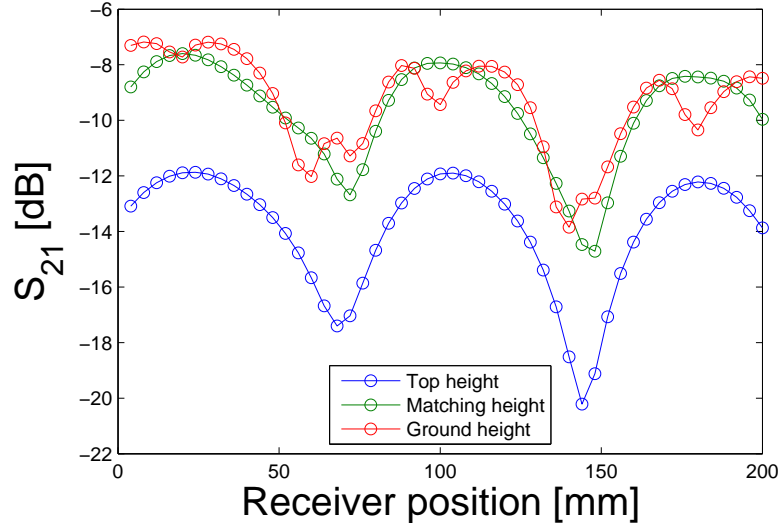


Figure 4.2.2.: Transmission coefficient  $S_{21}$  as a function of the height of the receiver. The receiver is located on the last cell.

#### 4.2.1. Measurement at 9mm of distance between metamaterial and receiver (Matching Height)

The transmission coefficient and efficiency are studied for three different conditions, corresponding to different termination impedance values. In particular:

- Condition A:  $Z_T = 0\Omega$  (corresponding to a short-circuited last cell);
- Condition B:  $Z_T = 120\Omega$  (much larger than  $\omega_0 M$ );
- Condition C:  $Z_T \gg 120\Omega$  (corresponding to an open circuit last cell).

The measured values of the transmission coefficient,  $S_{21}$ , in dB for each termination impedance considered as a function of frequency and receiver position are shown in Figure 4.2.3. As it can be noticed, the plot of  $S_{21}$  regarding condition A is quite different from those relevant to the other two conditions, that are very similar. The maximum values of the transmission coefficient are distributed for different frequencies and positions depending on the considered condition. Particularly, in the frequency range between about 12.4 and 15.5 MHz and when the receiver is positioned at 180mm, i.e., perfectly faced to the last resonator,  $S_{21}$  is over -10dB for the condition A but much smaller for the conditions B and C (-20dB). Moreover, for the condition A, the concentration of high transmission coefficient values around the resonant frequency means that the matching condition is achieved. For the conditions B and C high transmission coefficient values occur for different positions of the receiver along the metamaterial as it is confirmed by the measures of  $S_{21}$  and the adjusted efficiency presented in Figure 4.2.4.

If the last cell is short-circuited ( $Z_T = 0\Omega$ ) the maximum of the efficiency is achieved when the receiver faces the I, III and V resonator (confirming the trends presented in

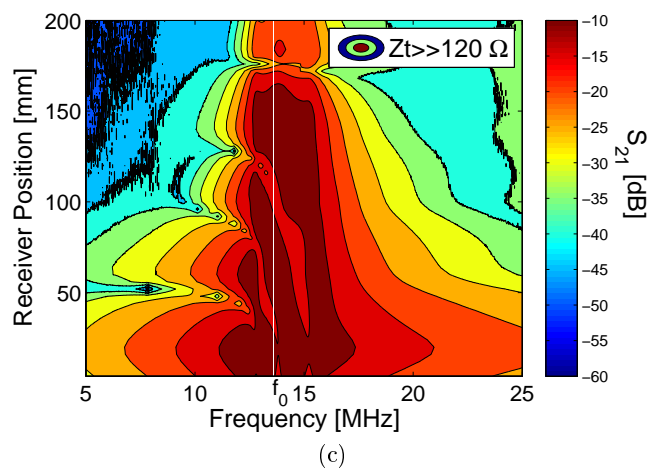
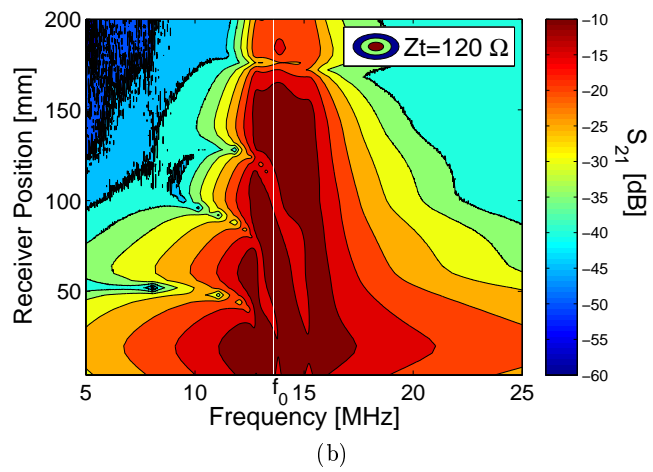
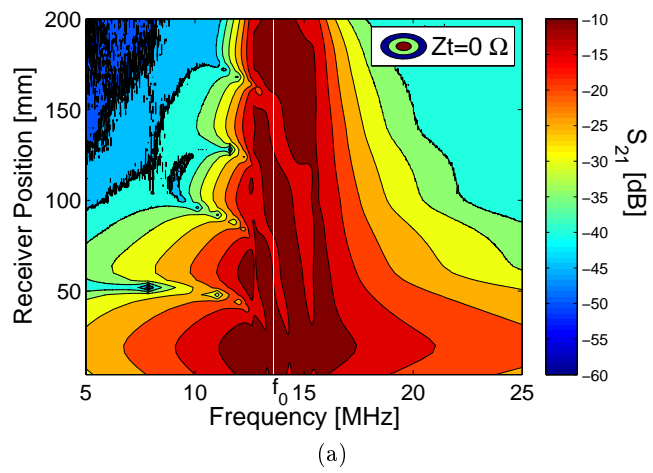


Figure 4.2.3.: Measurements of  $S_{21}$  as a function of frequency and receiver position for  $Z_T = 0\Omega$  (a),  $Z_T = 120\Omega$  (b) and  $Z_T \gg 120\Omega$  (c).

#### 4. Investigation of Termination Impedance Effects: Experiments and Simulations

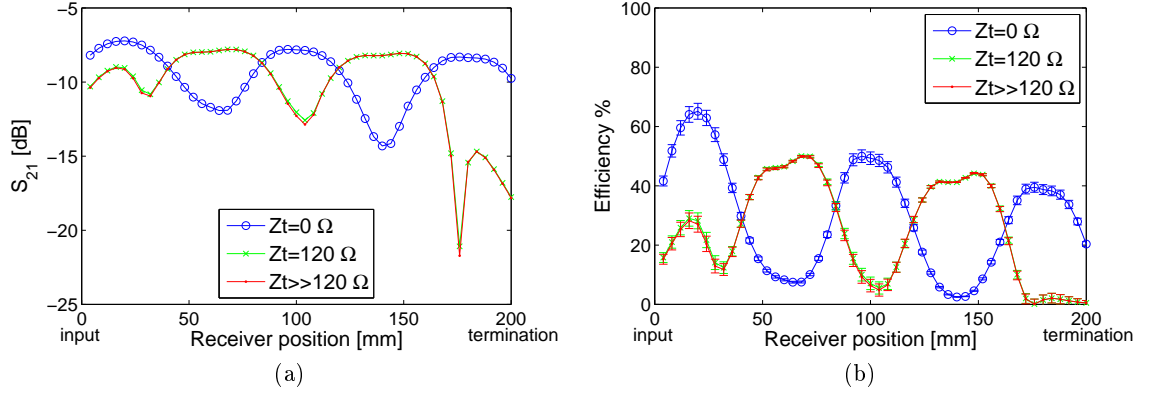


Figure 4.2.4.: Measurements of  $S_{21}$  (a) and adjusted efficiency (b) as a function of the receiver position for the termination impedances used and at  $f = f_0$ .

Table 4.1.: Equivalent impedance values,  $Z_{eq}$ , and efficiency,  $\eta$ , at  $f = f_0$  for different receiver positions and conditions calculated with (2.3.16).

| Receiver position | $Z_T = 0\Omega$  |          | $Z_T = 120\Omega$ |          |
|-------------------|------------------|----------|-------------------|----------|
|                   | $Z_{eq}[\Omega]$ | $\eta\%$ | $Z_{eq}[\Omega]$  | $\eta\%$ |
| I cell            | 1.6              | 67%      | 7.2               | 30%      |
| II cell           | 0.2              | 10%      | 1.1               | 58%      |
| III cell          | 1.4              | 53%      | 6.2               | 5%       |
| IV cell           | 0.3              | 5%       | 1.2               | 49%      |
| V cell            | 1.3              | 43%      | 5.8               | 0%       |

Figure 4.2.2). The introduction of a high impedance ( $Z_T = 120\Omega$  or  $Z_T \gg 120\Omega$ ) involves a displacement of peaks by one cell: in fact, the efficiency peaks occur when the receiver is on the II and IV cell (cell centres at 60 and 140mm). Also, observing the equivalent impedance values reported in Table 4.1, the value of  $Z_{eq}$  is very close to  $\omega_0 M = 1.39\Omega$  in positions where the efficiency is maximum. Finally, the correspondence of the peaks at the resonant frequency is further validated by showing the behaviour of  $S_{21}$  as a function of frequency when the receiver is perfectly located on each cell, as depicted in Figure 4.2.5. The behaviour of the transmission coefficient is strongly affected by the introduction of a termination impedance  $Z_T$  which changes the distribution of the transmission coefficient peaks in the resonant frequency bandwidth. In particular, with the connection or disconnection of the termination impedance, the maximum values of  $S_{21}$  can be obtained at the resonant frequency in all the receiver positions.

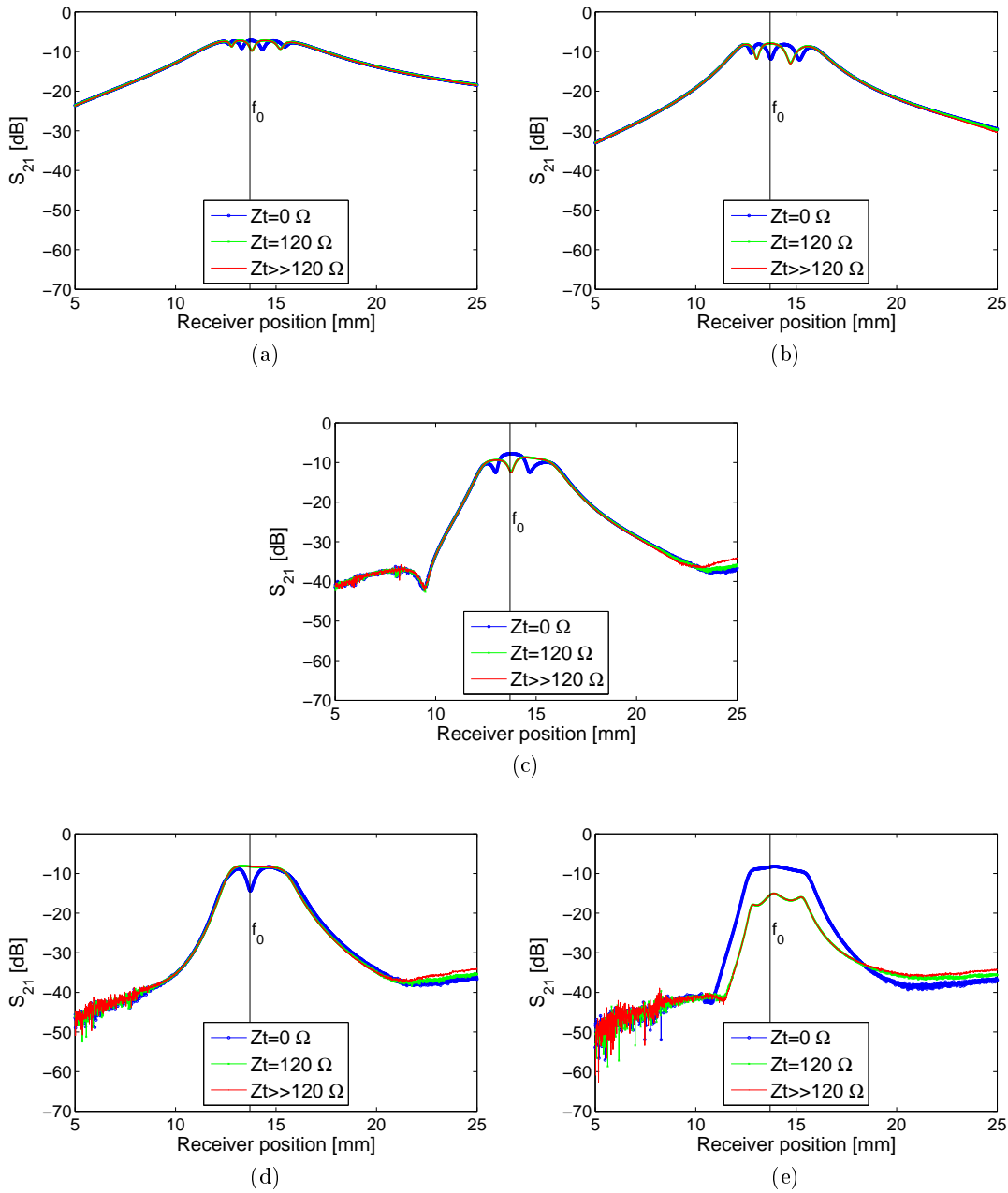


Figure 4.2.5.:  $S_{21}$  measured as a function of frequency for all receiver positions facing the I (a), II (b), III (c), IV (d) and V (e) cell.

#### 4. Investigation of Termination Impedance Effects: Experiments and Simulations

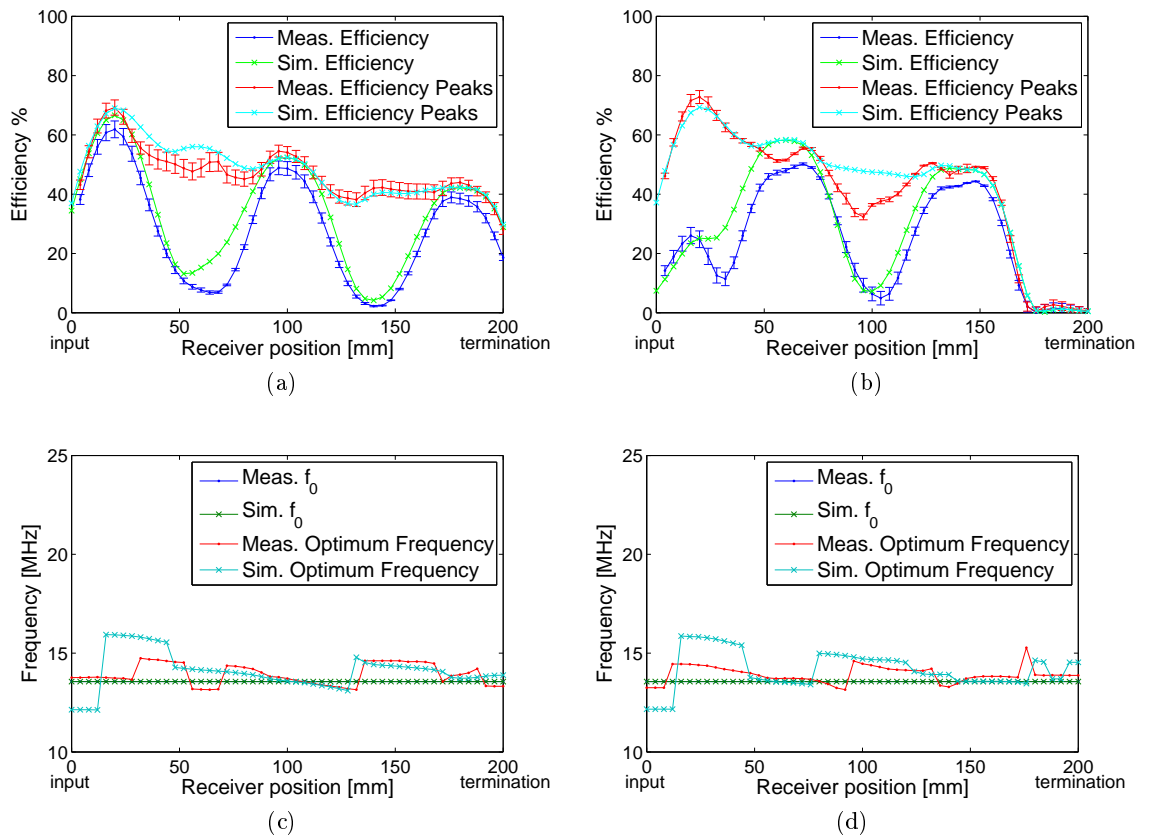


Figure 4.2.6.: Comparison of measured and simulated efficiency and efficiency peaks and optimum frequency for  $Z_T = 0\Omega$  (a) and (c) and  $Z_T = 120\Omega$ , (b) and (d), respectively.

### 4.2.2. Comparison with simulations

The measurements are now compared with numerical simulations, made implementing the formulas presented in Chapter XX in a Matlab programme [48]. In particular the efficiency, peaks of efficiency and optimum frequencies are studied and taking into account only two different conditions, A ( $Z_T = 0\Omega$ , shown in Figure 4.2.6 (a) and (c)) and B ( $Z_T = 120\Omega$ , shown in Figure 4.2.6 (b) and (d)), as conditions B and C ( $Z_T \gg 120\Omega$ ) are found to be equivalent. Peaks of efficiency are defined as the maximum values of efficiency occurring at the resonant frequency and optimum frequencies as those frequencies at which the peaks of efficiency are achieved. As shown, all the simulations match with very good agreement the experimental data. Considering the efficiency, the largest difference is obtained for the receiver centre between 0 and 60mm in the condition B (as it can be noticed in Figure 4.2.6(b)). Moreover, a small difference (10%) is obtained for the receiver centre between 80mm and 120mm, as regarding the peaks of efficiency. Consequently, the prediction of the optimum frequencies show a little disagreement with the measurement for the same receiver positions (as shown in Figure 4.2.6(d)) even if the general behaviour is similar to the measurement.

Finally, it is worth noticing that the efficiency and efficiency peaks are very close when the receiver is perfectly aligned with the resonators I, III and V for the condition A (see Figure 4.2.6 (a)) or to the resonators II and IV for the condition B (see Figure 4.2.6 (b)). Correspondingly, in the same positions the optimum frequencies of both conditions A and B are close to the resonant frequency, as shown in Figure 4.2.6 (b) and (d), respectively. This behaviour enhances the assumption that the matching condition occurs every two cells (as previously demonstrated by the equivalent impedance values, Table 4.1) .

## 4.3. Discussion of the results

The experimental analysis presented in this work shows the behaviour of the power delivered to a receiver sliding along a metamaterial for three different values of a termination impedance,  $Z_T$  (the conditions A, B and C presented in Section 4.1). In the experiments, it was found that the termination impedance affects the received power behaviour modifying the equivalent impedance  $Z_{eq}$  and, hence, the position of the receiver where the maximum value of efficiency is achieved. In this way, it is possible to obtain the best behaviour for any position of the receiver by varying the  $Z_T$  value between 0 and a high value (in this work  $120\Omega$ , almost a hundred times larger than  $\omega_0 M$ ) in order to maintain the equivalent impedance always about  $\omega_0 M$  (as reported in Table 4.1). In Figure 4.3.1, the envelopes of the efficiency and peaks of efficiency obtained for the termination impedances of 0 and  $120\Omega$  with the respective optimum frequencies are shown as a function of the receiver position. It can be seen that the envelope of the efficiency has globally higher values than the cases with constant termination impedances. Moreover, the envelope of the efficiency overlaps the envelope of the efficiency peaks for a number of receiver positions. Also, the optimum frequencies, with the exception for the first cells, are closer to the resonant frequency: this is due to the equivalent impedance closer to the matching condition.

#### 4. Investigation of Termination Impedance Effects: Experiments and Simulations

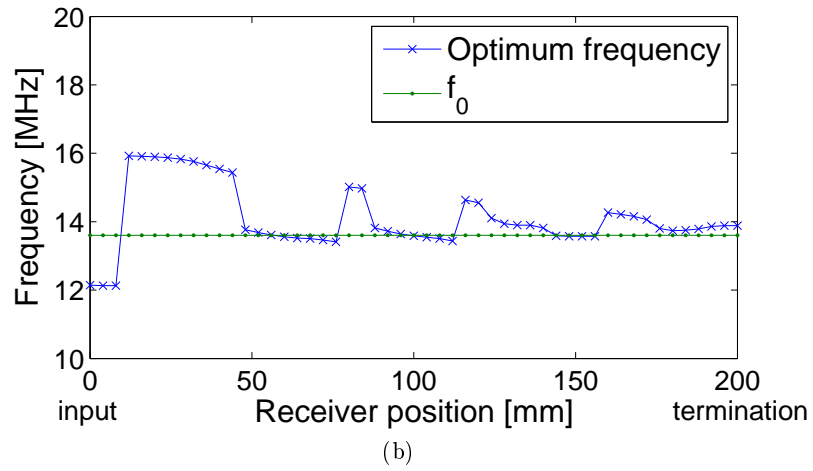
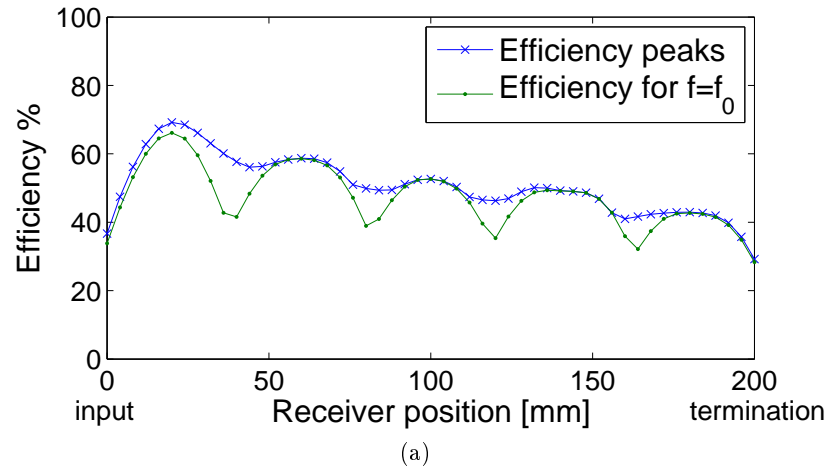


Figure 4.3.1.: Comparison between simulated envelopes of efficiency and efficiency peaks (a) and optimum frequencies (b).

Transmitted power and efficiency are investigated under different termination impedance conditions that improve significantly the efficiency at the resonant frequency. All the considerations presented in this work are supported by circuitual, numerical and experimental results.

## 5. Design of Metamaterial with Multilayer Flat Spiral Resonators for WPT

This Chapter presents a procedure to characterize a multilayer and multiturn flat spiral resonator through 2D finite element simulations and numerical calculations. The procedure is general and valid for both rectangular and square shapes. It considers all the parasitic effects occurring for low frequencies (from kHz to few MHz) and for complex structures (i.e., skin effect, crowding current density, proximity effect, stray capacitance and dielectric losses). In particular, the work takes into account validated procedures both proposed by literature and also new and more complete simulation methods (particularly regarding AC resistance). Two resonator samples with different shapes and dimensions are investigated, and with large number of turns and layers in order to validate the proposed procedure. The characterization is supported by comparisons with Sonnet software and allows the self-resonant frequency and quality factor, fundamentals for the design of wireless power transfer via metamaterials, to be predicted with good accuracy.

The Chapter is organized as follows: after a brief explanation of the design of the single layer flat spiral resonator, an accurate modelling method of the multilayer flat spiral resonator is reported. The numerical method used in this work to define the AC resistance, self-inductance and stray capacitance is detailed in Section 5.2. Also, after the explanation of the electromagnetic model simulated with Sonnet, the main results of the proposed method are shown in Section 5.3: they consist in analyzing the main electrical parameters as a function of frequency and geometrical dimensions in order to predict the self-resonant frequency and quality factor of the resonators. All the results are compared with an electromagnetic programme (Sonnet [52]). Finally, in Section 5.3.2, the conclusions and main considerations about the validation are discussed.

### 5.1. Modelling of multilayer flat spiral resonator

Flat spiral resonators are widely used in radio frequency (RF) applications, such as amplifiers, oscillators, filters and sensors [53]. Recently, they are also considered by researchers as intermediate resonators (spiral resonator, SR) or metamaterial cells in wireless power transfer applications, thanks to their capability to tune the self-resonant frequency to a few MHz with good performance [54, 32, 55]. Furthermore, the possibility to design flat spiral resonators with different shapes and frames (such as printed circuit board, PCB, fabricated on a flexible substrate as polyimide or on the more rigid FR-4

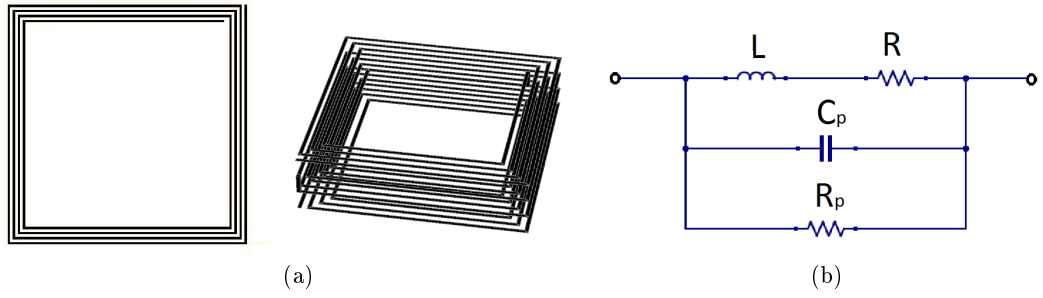


Figure 5.1.1.: Examples of single layer and multilayer flat spiral resonators (a) and their quasi-static equivalent circuit (b).

one) makes these resonators suitable for industrial and biomedical applications operating below a few tens of MHz (such as the 13.56 MHz (license free Industrial, Scientific and Medical, ISM, band)).

In Figure 5.1.1(a), examples of single layer and multilayer flat spiral resonators are depicted. As it is known, the high frequency behaviour of an inductor is very different from that at low frequency because the stray capacitances cannot be neglected [56, 57, 46]. Also, the increase of the frequency involves an increment of the resonator resistance particularly due to the skin and proximity effects. For these reasons, referring to 5.1.1(b), the resonator has to be electrically modeled with a lumped stray capacitance,  $C_p$ , connected in parallel between the terminals of the winding which presents an AC resistance,  $R$ , in series to the self-inductance,  $L$ . Finally, a parallel resistance  $R_p$  is taken into account to represent the substrate losses that worsen the quality factor and efficiency also at low frequencies [44, 58]. Consequently, the self-self-resonant frequency  $f_0$  and quality factor  $Q$  are calculated as

$$f_0 = \frac{1}{2\pi\sqrt{LC_p}} \quad (5.1.1)$$

$$Q = \frac{\text{Im}(\hat{Z})}{\text{Re}(\hat{Z})} \quad (5.1.2)$$

with the resonator impedance defined as

$$\hat{Z} = \frac{(R + j\omega L)}{(R + j\omega L)(1/R_p + j\omega C_p) + 1} \quad (5.1.3)$$

## 5.2. Numerical characterization

The theoretical predictions of the self-inductance and stray capacitance are quite different and more complicated if a number of layers are considered: in fact, mutual coupling between layers exists and stray capacitances between layers and turns must be taken into account as they strongly affect the self self-resonant frequency calculation. Furthermore, the AC resistance is affected from strong proximity effect. Nevertheless, as for the single

layer, at high frequency a multilayer flat spiral resonator can be electrically modeled as shown in Figure 5.1.1(b) and the self-resonant frequency is consequently calculated with (5.1.1). The accurate design of a single metamaterial cell is of fundamental importance for the system design and performance in terms of quality factor and losses (given by magnetic effects and AC resistance), particularly for wireless power transfer systems.

Hence, this work proposes a numerical characterization of a multilayer flat spiral resonator that can be used as a metamaterial. The characterization presented is numerical and use the finite element programme FEMM for calculating the resistance, self-inductance and stray capacitance [59] in order to validate and predict the parasitic parameters with very good agreement. In particular, a novel and accurate procedure for the AC resistance calculation is proposed.

A detailed electrical model of the multilayer flat spiral resonator is now presented. The numerical characterization proposed is totally generic and applicable for both square and rectangular flat spiral resonators.

The main geometrical dimensions of a multilayer flat spiral resonator are shown in Figure 5.2.1, namely:

- $N$ , number of turns per layer;
- $n$ , number of layers;
- $l$  and  $l_m$  larger and shorter external sides, respectively (for a square shape,  $l = l_m$ );
- $w$ , metal track width;
- $s$ , spacing between turns;
- $t_c$ , metal track thickness;
- $h$ , distance between layers.

### 5.2.1. AC Resistance: skin and proximity effects

The resistance  $R$  of a multilayer flat spiral resonator must take into account all the parasitic effects dominating in AC frequency especially in complicated structures. In fact, skin and proximity effects increase significantly the resistance value with the frequency and, particularly, number of layers, turns and closeness of the sides. This effect is enhanced at a high degree decreasing  $h$  and  $s$  [46]. This subsection describes a novel approach for calculating the AC resistance through the Finite Element Method Magnetics (FEMM) [59] by carrying out a 2D analysis on a transversal cross section of the resonator. The parallel sides of the resonator are divided in elements such that facing elements have the same length. The total number of layer elements is  $n_l$ . An example of partition of three parallel sides of a resonator with three turns is depicted in Figure 5.2.2(a). There are three groups of elements with the same length:  $l_1 = l_2 = l_3$ ,  $l_4 = l_5 = l_6 = l_7$  and  $l_8 = l_9$ . The partition has to be carried out also for the other remaining parallel sides.

## 5. Design of Metamaterial with Multilayer Flat Spiral Resonators for WPT

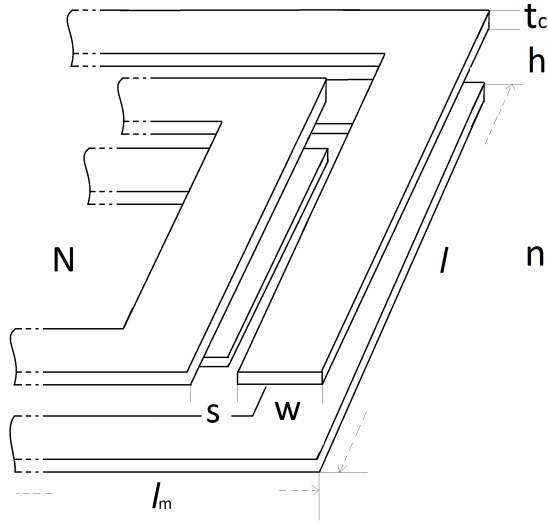


Figure 5.2.1.: Particular of multilayer flat spiral coil: main geometrical dimensions (drawing not in scale).

Following, the elements with the same length are simulated with FEMM and the per unit length (p.u.l.) resistance of each  $i$ th-element  $R_i$  is found by applying a sinusoidal current to it. In this way, all the different current distributions are considered and resonators can be quickly and accurately analysed through 2D finite element simulations. Figures 5.2.2(b)-(d) show the current distribution in the elements in which the resonators has been partitioned calculated with FEMM.

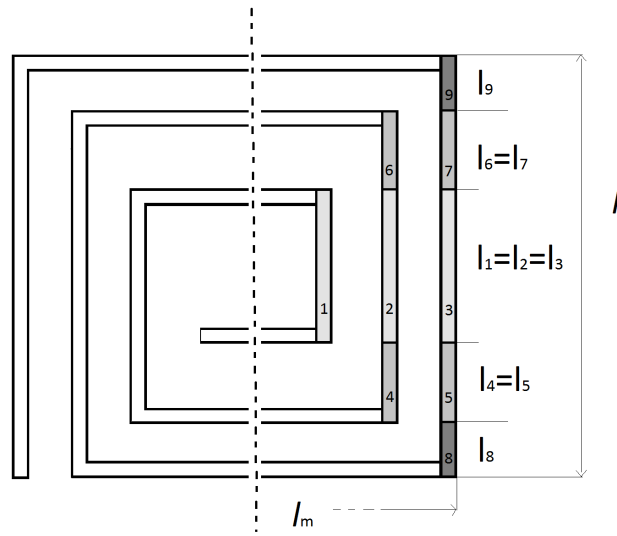
Consequently, the resistance of the whole rectangular resonator is obtained by summing all the calculated resistances

$$R = 2 \sum_{i=1}^{n_l \cdot n} R_i l_i + 2 \sum_{i=1}^{n_l \cdot n} R_i l_{mi} \quad (5.2.1)$$

where  $l_i$  and  $l_{mi}$  are the lengths of the  $i$ th-element of the considered external sides  $l$  and  $l_m$ , respectively. If a square shape resonator is considered  $l = l_m$  and the total resistance is obtained directly as  $R = 4 \sum_{i=1}^{n_l \cdot n} R_i l_i$ .

In Figure 5.2.3, the p.u.l. resistance  $R$  predicted with the proposed procedure and compared with Sonnet simulations is shown.  $R$  is calculated as a function of the number of turns  $N$  and for different  $s$ ,  $n$  and  $h$ . In each simulation  $w = 1$  mm and  $f = 1$  MHz. As shown, the proximity effect is evident:  $R$  increases particularly with the number of conductors and their closeness. In fact, considering the curves for  $n = 2$ , the augment of  $N$  does not affect significantly the p.u.l. resistance. On the contrary, if more layers are considered, as for the resonator with  $n = 6$ ,  $h = 1$  mm and  $s = 1$  mm, the number of turns has a great impact on  $R$ , even more evident for smaller distances between sides ( $n = 6$ ,  $h = 0.5$  mm and  $s = 0.5$  mm).

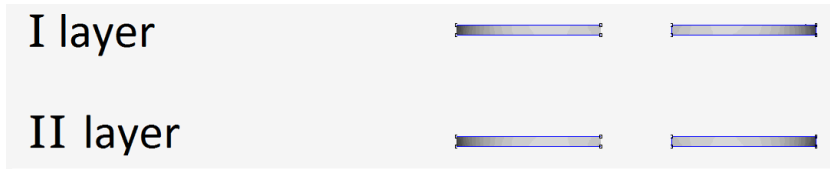
Vice versa, reducing the number of turns, the proximity effect is much lower also for



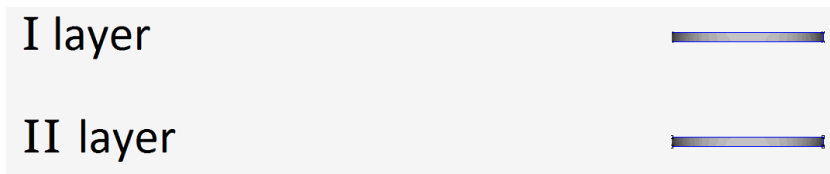
(a)



(b)



(c)



(d)

Figure 5.2.2.: Top view of the partition of a flat spiral resonator layer with  $N = 3$ . The partition of the three parallel sides with  $n_l = 9$  is shown. The facing elements have the same length (a). Current distribution in the partition elements with  $l_1 = l_2 = l_3$  (b),  $l_4 = l_5 = l_6 = l_7$  (c) and  $l_8 = l_9$  (d) simulated with FEMM for a resonator with  $N = 3$ ,  $n = 2$ ,  $w = 1$  mm,  $s = 0.5$  mm,  $h = 0.5$  mm and  $t_c = 0.05$  mm .

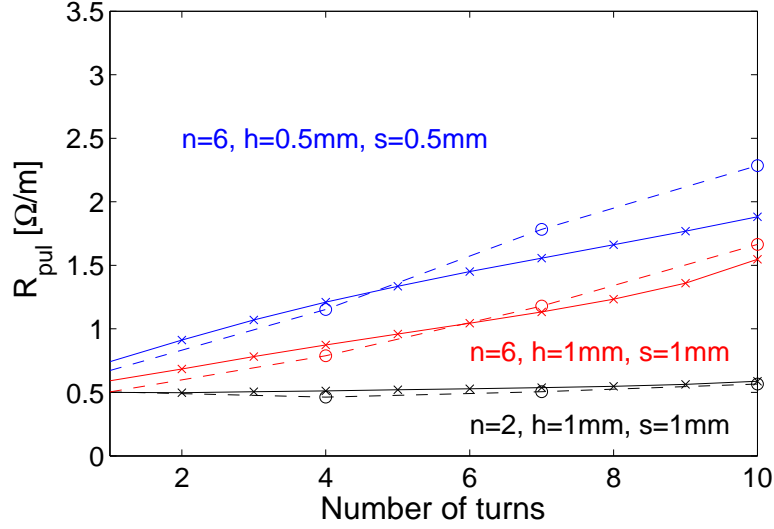


Figure 5.2.3.: P.u.l. resistance as a function of the number of turns for different layer numbers ( $n$ ), distances between layers ( $h$ ) and turns ( $s$ ). In each simulation  $w = 1\text{mm}$  and  $f = 1\text{MHz}$ . Comparison between proposed procedure ('x') and Sonnet simulations ('o').

the largest number of layers. The same effects are evident also for lower frequencies, even if the p.u.l. resistance has smaller values particularly for large number of turns, as shown in Figure 5.2.4 for  $f = 0.25\text{ MHz}$ .

### 5.2.2. Self-Inductance

As regards the self-inductance of a multilayer flat spiral resonator,  $L$  can be calculated by means of the partial inductance concept, outlined by Ruehli in [60]. Briefly, the method consists in the calculation of the partial self- and mutual inductances of  $N \cdot n$  simpler and straight sub-elements into which the whole resonator can be divided, as it is demonstrated that an inductance contribution can be uniquely associated to each element of a closed loop. The method holds also for incomplete loops. In this way, the self-inductance of complicated shape resonators can be simply calculated (for example zig-zag spiral resonators with uniform and nonuniform arms[36, 61], as reported in Appendix B). The total inductance of a loop,  $L$ , is then equal to the sum of the partial self-inductance of each straight element plus all the partial mutual inductances between the sub-elements:

$$L = \sum_{i=1}^{N \cdot n} \sum_{j=1}^{N \cdot n} M_{pij} \quad (5.2.2)$$

where  $M_{pij}$  ( $j \neq i$ ) is the partial mutual inductance between any two sub-elements  $i$  and  $j$  of the spiral resonator and  $M_{pij} = L_p$  when ( $j = i$ ) representing the partial self-inductance of the  $i$ -th rectangular track. As regards  $M_{pij}$ , the numerical calculation

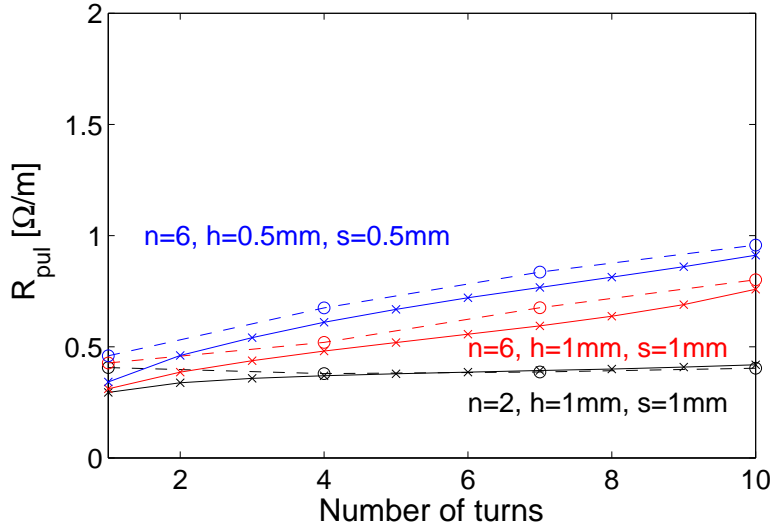


Figure 5.2.4.: P.u.l. resistance as a function of the number of turns, for different layer numbers ( $n$ ), distances between layers ( $h$ ) and turns ( $s$ ). In each simulation  $w = 1\text{mm}$  and  $f = 0.25\text{MHz}$ . Comparison between proposed procedure ('x') and Sonnet simulations ('o').

validated and proposed in [49] is used and briefly reported in Chapter 3.  $L_p$  is calculated with FEMM. The partial self- and mutual inductances of straight conductors of rectangular cross-sections can also be analytically calculated in approximate and exact forms as shown in [62] and [63], respectively.

### 5.2.3. Stray capacitance and parallel resistance

The stray capacitance  $C_p$  is found as the sum of all the parasitic capacitances distributed in every adjacent couple of conductors composing the multilayer flat spiral resonator. Both the capacitances between turns  $C_{p,tt}$  and layers  $C_{p,ll}$  are considered.  $C_{p,tt}$  per layer is easily found through the formula proposed in [44]. Regarding the  $C_{p,ll}$  calculation, the method proposed in [64] is used, where the stray capacitance between layers is found for multilayer spiral resonators with circular shapes and traditional or alternating windings. Briefly, the method consists in the calculation of the stray capacitance through the following expression

$$C_{p,ll} = \frac{2E_{ct}}{V_t^2} = \frac{\sum_{i=1}^{N(n-1)} \sum_{j=1}^{N(n-1)} E_{cij}}{V_t^2} \quad (5.2.3)$$

where  $V_t$  is the voltage source applied to the resonator and  $E_{ct}$  is the total electrical energy stored among layers in the resonator, obtained by the sum of the energy  $E_{cij}$  between two metallic tracks  $i$  and  $j$ , given by  $E_{cij} = (1/6) C_{ij} [V_{Aij}^2 + V_{Bij}^2 + V_{Aij} V_{Bij}]$ ,

5. Design of Metamaterial with Multilayer Flat Spiral Resonators for WPT

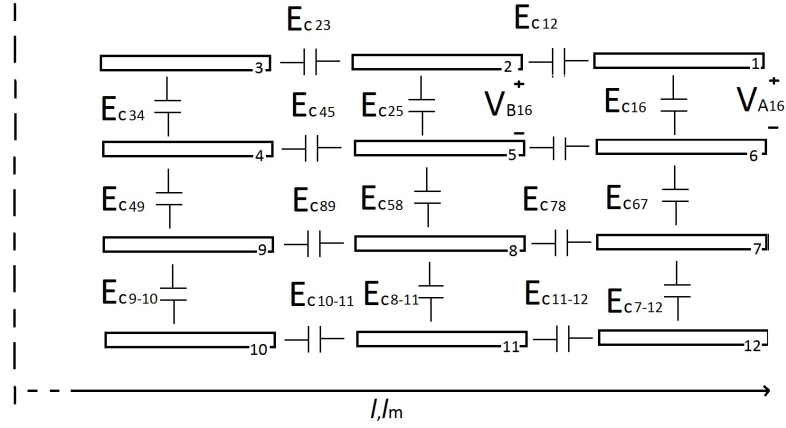


Figure 5.2.5.: Electrical energy associated to each couple of conductors considered. Cross-sectional view of the windings of a flat spiral resonator with  $N = 3$  and  $n = 4$ .

Table 5.1.: Main geometrical dimensions of the two flat spiral resonators considered,  $SR_s$  and  $SR_r$ .

|        | $l$<br>[mm] | $l_m$<br>[mm] | $w$<br>[mm] | $s$<br>[mm] | $t_c$<br>[mm] | $h$<br>[mm] |
|--------|-------------|---------------|-------------|-------------|---------------|-------------|
| $SR_s$ | 40          | 40            | 1           | 0.5         | 0.05          | 0.25        |
| $SR_r$ | 35          | 20            | 0.5         | 0.5         | 0.1           | 0.1         |

where  $V_{Aij}$  and  $V_{Bij}$  are the difference of potential between the start and end terminal points, respectively, of tracks belonging to turns of facing layers. As an example, Figure 5.2.5 shows the electrical energy associated to the first turn of the first layer and the first turn of the second layer.  $C_{ij}$  is the capacitance between the tracks  $i$  and  $j$ . Finally, the total stray capacitance  $C_p$  is found by the following expression

$$C_p = C_{p,ll} + nC_{p,tt}. \quad (5.2.4)$$

The parallel resistance  $R_p$  is commonly neglected in many applications because its value normally corresponds to a reactance much larger than the reactance  $X_p = 1/\omega C_p$ . In addition, if lumped capacitances are connected to the resonator to tune the self-resonant frequency to a value much lower than the intrinsic one (5.1.1),  $R_p$  can be furtherly neglected for frequencies smaller than the one yielding the maximum of the quality factor [58]. However, multilayer resonators can have a low self-resonant frequency (5.1.1) and, when operate at even lower frequencies,  $R_p$  may not be negligible any longer and it may affect significantly the Q value, as it is shown in Figure 5.2.6. In this case, once the equivalent stray capacitance of the system is found (5.2.4), the equivalent parallel

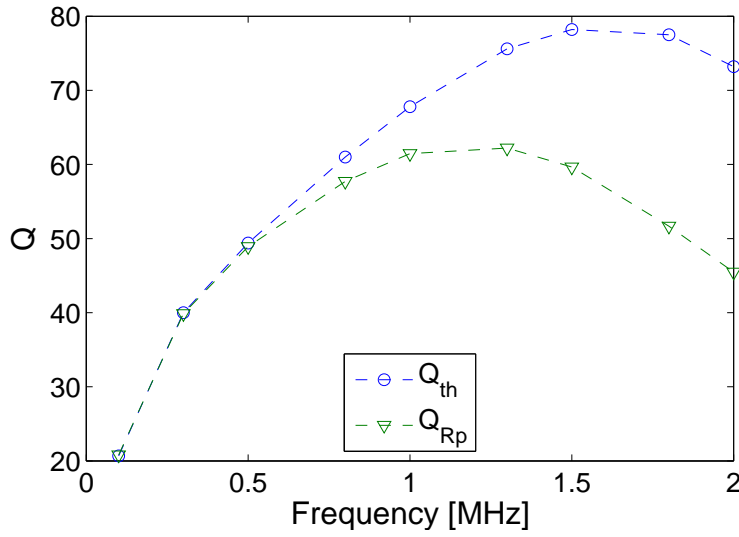


Figure 5.2.6.: Comparison between the quality factors with ( $Q_{Rp}$ ) and without ( $Q_{th}$ ) dielectric losses performed with Sonnet. The simulated spiral resonator has the geometrical dimensions of the resonator  $SR_r$  tabulated in Tab. 5.1, with  $n = 6$  and  $N = 8$  and FR4 insulating layers. The self-resonant frequency  $f_0$  is about 3.8 MHz.

resistance is simply approximated by means of the loss tangent,  $\tan \delta$  [65]

$$R_p = \frac{1}{\omega C_p \tan \delta}. \quad (5.2.5)$$

### 5.3. Sonnet validation

All the numerical results presented in this Section are compared with those obtained with Sonnet software [52], based on the Method of Moment (MoM) technique which takes into account all coupling and radiation effects from DC to THz. It is usually used for filters, antennas and generally for printed circuit board (PCB) but, recently, it is also used for Radio Frequency Identification (RFID) tag and reader design [66].

All the electrical parameters are calculated through the admittance parameter  $\hat{Y}_{21}$  as a function of frequency. The resistance  $R_{Sonnet}$  is thus predicted using

$$R_{Sonnet} = -\text{Re} \left( \frac{1}{\hat{Y}_{21}} \right) \quad (5.3.1)$$

and the self-inductance  $L_{Sonnet}$  with

$$L_{Sonnet} = \frac{\text{Im}(1/\hat{Y}_{21})}{2\pi f}. \quad (5.3.2)$$

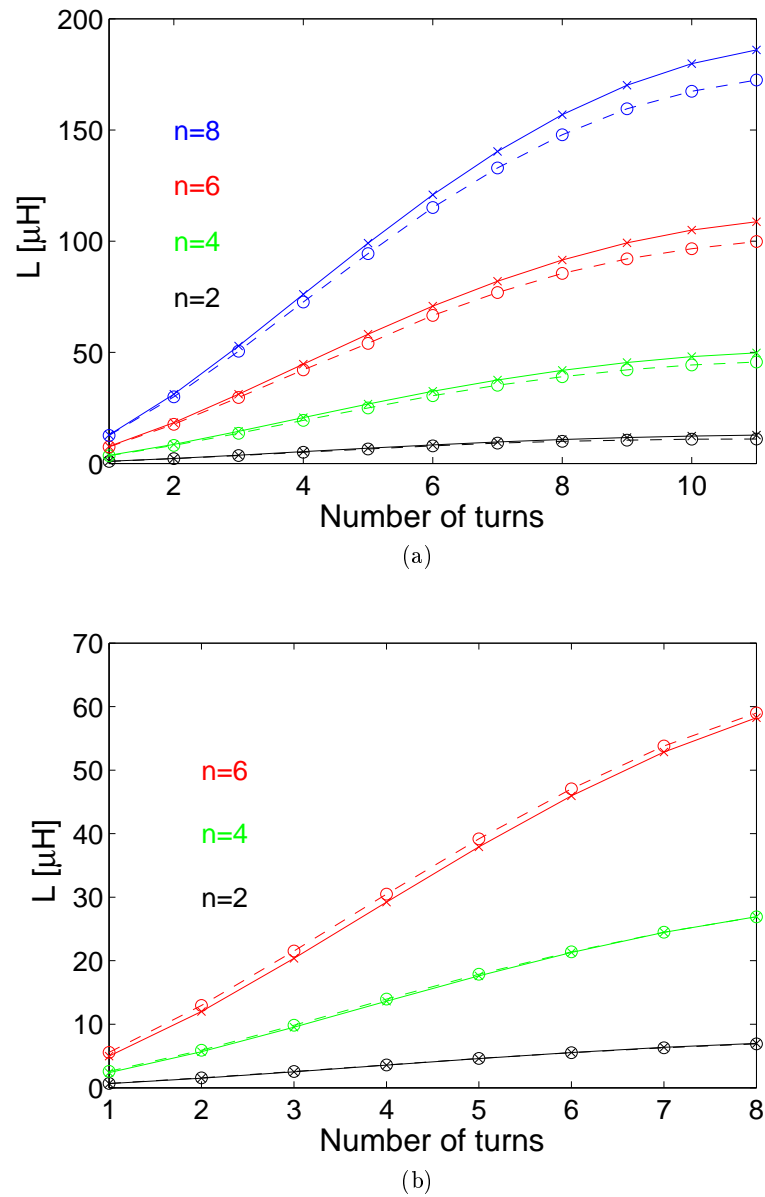


Figure 5.3.1.: Self-inductance of the resonators  $SR_s$  (a) and  $SR_r$  (b) as a function of the number of turns for different layer numbers. Comparison between the proposed model ('x') and Sonnet simulations ('o').

The self-resonant frequency  $f_{0,Sonnet}$  is calculated analyzing the behaviour of the self-inductance as a function of frequency (swept from 0.1 MHz to the self-resonant frequency). As regards the stray capacitance, it can be calculated using (5.1.1) once the self-inductance and self-resonant frequency are found. In each simulation, FR4 insulating layers ( $\epsilon_r = 4.4$  and  $\tan \delta = 0.02$ ) are interposed between the inner resonator layers.

### 5.3.1. Results and comparisons

Two different resonators,  $SR_s$  and  $SR_r$ , are considered; their geometrical dimensions are tabulated in Table 5.1.  $SR_s$  has a square shape and  $SR_r$  a rectangular one. The electrical parameters  $L$  and  $C_p$  of both samples are studied as a function of turns for different layers numbers and are shown in Figs. 5.3.1 and 5.3.2, respectively. In Figure 5.3.3 the self-resonant frequency of the resonators is plotted.

As widely confirmed in the literature, an increase of the number of turns and layers involves a significant augment of the self-inductance, as both resonators show in Figs. 5.3.1(a) and (b). However, different considerations must be done as regards the stray capacitance shown in Figure 5.3.2. In fact, although the stray capacitance  $C_p$  increases with the increase of the number of turns, it radically drops with the number of layers. For example, with reference to Figure 5.3.2(a), the simulated  $C_p$  for the resonator  $SR_s$  with  $N = 11$  falls down from beyond 70 pF for  $n = 2$  to about 35 pF for  $n = 8$ . The same considerations hold for the resonator  $SR_r$  in Figure 5.3.2(b). Anyway, for an increasing layer number, the increment of the self-inductance is larger than the stray capacitance decrease, resulting in a reduction of the self-resonant frequency, as shown in Figs. 5.3.3(a) and (b), with a significant variation particularly when the number of turns is small.

Thus, once all the parasitic effects affecting the resonator have been considered, the quality factor as a function of the geometrical dimensions and frequency can be predicted through (5.1.2). The  $Q$  of  $SR_s$  and  $SR_r$  is shown in Figure 5.3.4 and investigated versus the number of turns and layers and for frequencies up to the relevant quality factor peak. As it can be noticed, the peak of the quality factor collapses drastically with the increase of  $N$  and  $n$  and occurs at frequencies lower than those corresponding to maximum value ( $N = 2, n = 2$ ). However, at the lowest frequencies the increment of  $N$  and  $n$  involves a slight increment of  $Q$ . In fact, with reference to Figure 5.3.4(a), for  $f = 0.1$  MHz the quality factor increases from 5 with  $N = 2, n = 2$  to 21 with  $N = 11, n = 8$ . The same behaviour is also found for the resonator  $SR_r$ , whose quality factor is depicted versus the number of layers and turns as a function of frequency in Figure 5.3.4(b).

### 5.3.2. Discussion of the results

Multilayer and multiturn flat spiral resonators are components that present a difficult electrical characterization. In particular, a large number of conductors and their proximity may enhance parasitic effects like crowding current density, proximity effects and stray capacitances. This Chapter presents a complete modelling of this type of resonators analyzing the main electrical parameters as a function of the geometrical dimensions and frequency. The proposed design is supported by numerical simulations and can be im-

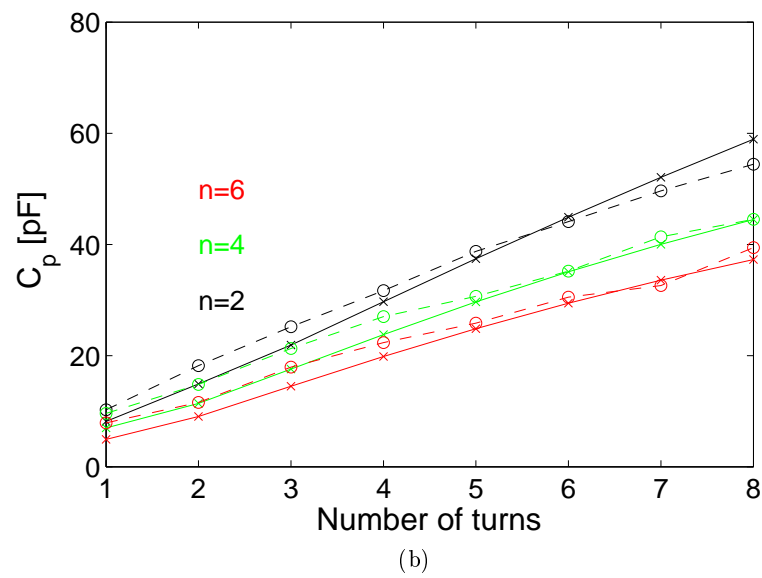
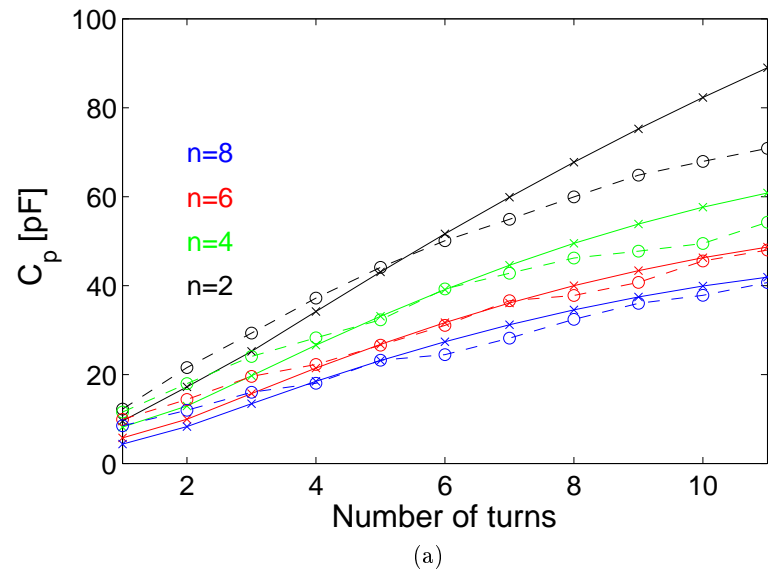


Figure 5.3.2.: Stray capacitance of the resonator  $SR_s$  (a) and  $SR_r$  (b) as a function of the number of turns for different layer numbers. Comparison between the proposed model ('x') and Sonnet simulations ('o').

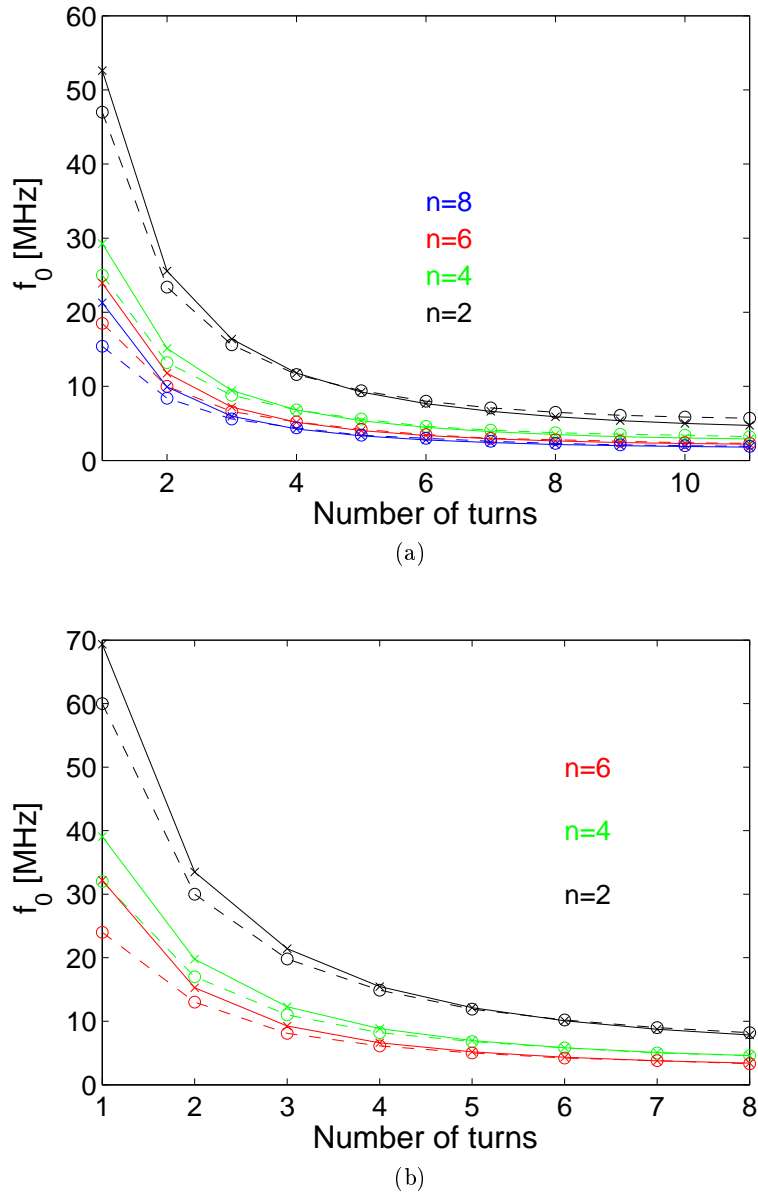


Figure 5.3.3.: Self-resonant frequency of the resonators  $SR_s$  (a) and  $SR_r$  (b) as a function of the number of turns for different layer numbers. Comparison between the proposed model ('x') and Sonnet simulations ('o').

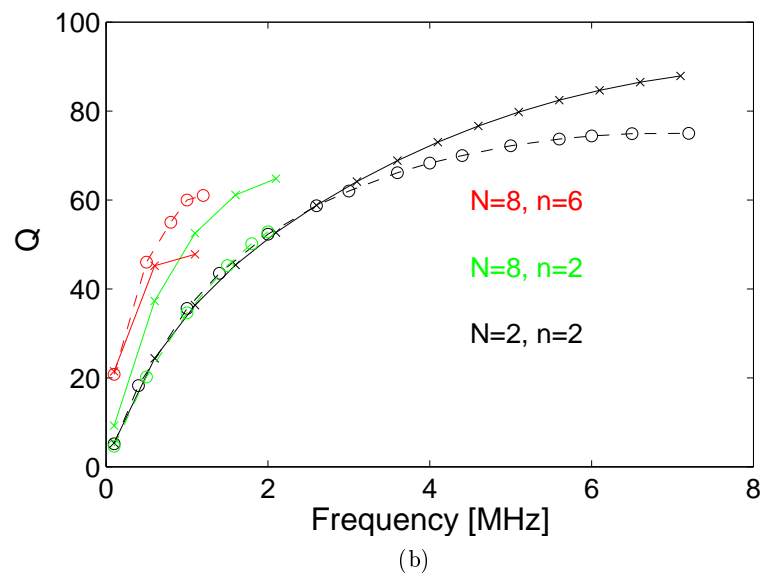
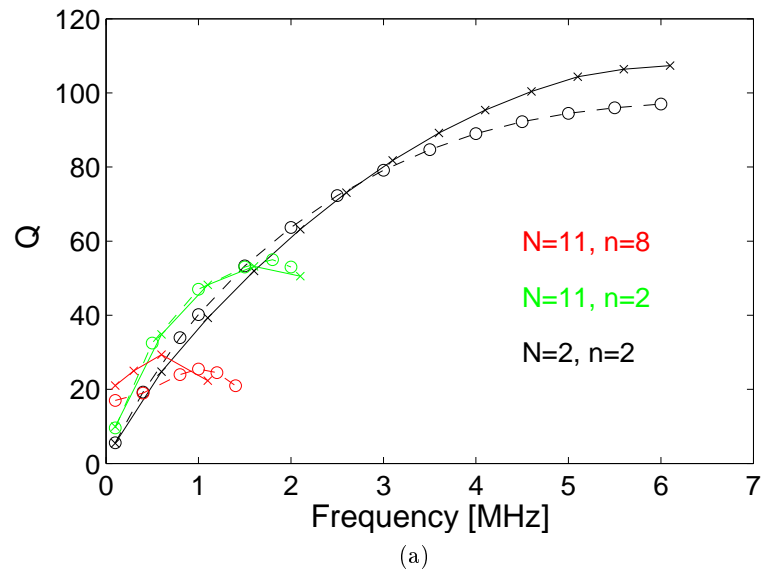


Figure 5.3.4.: Quality factor of the resonators  $SR_s$  (a) and  $SR_r$  (b) for different number of layers and turns as a function of frequency. Comparison between the proposed model ('x') and Sonnet simulations ('o').

plemented and interfaced with finite element programme in a computing environment in order to obtain accurate results. The validation of the procedure is made comparing the results with those obtained with the Sonnet software. In particular, regarding the self-inductance, the largest difference in the comparison is found for the maximum number of turns and layers, as shown in Figure 5.3.1(a). Differently, the stray capacitances agree with those found in the electromagnetic simulations for different dimensions and shapes. Referring to Figure 5.3.2, a difference is found for both resonators  $SR_s$  and  $SR_r$  for the maximum number of turns and minimum number of layers (e.g., 15 pF for  $SR_s$  with  $n = 2$  and  $N = 11$ ) but the general behaviour is well predicted. Consequently, the self-resonant frequency is predicted with good accuracy, as Figure 5.3.3 shows.

As regards the quality factor, the biggest difference is found near the peaks (as shown in Figure 5.3.4). The biggest difference in the  $Q$  prediction is about 15 and is obtained for the  $SR_r$  for the maximum number of turns and layers, due to the difficulty in the resistance estimation (as demonstrated by the p.u.l. resistance shown in Figure 5.2.3).

## 5.4. Metamaterial modelling

According to the magnetoinductive waves theory (MIW), the current flowing in the resonator  $i$ th can be expressed as  $\hat{I}_i = I_1 e^{-\hat{\gamma}(i-1)d}$ , where  $I_1$  is the phasor of the current flowing in the first cell,  $d$  is the periodic distance between two adjacent cells and  $\hat{\gamma}$  is the propagation constant defined as  $\hat{\gamma} = \alpha + j\beta$ .  $\alpha$  and  $\beta$  are the attenuation and phase constants, respectively, and they could also be expressed in terms of electrical parameters [27]. The attenuation constant is particularly interesting because meaning of the wave losses per cell and it can be defined as follows[29]:

$$\alpha = \frac{1}{d} \ln \left[ \frac{1}{kQ} + \sqrt{1 + \frac{1}{kQ}} \right] \quad (5.4.1)$$

where  $k = M/L$  is the coupling coefficient between two adjacent resonators and the quality factor of the each resonator can be approximated at low frequency as  $Q = \omega_0 L/R$ . From the coupling coefficient it is possible to obtain the bandwidth in which the wave propagation is achieved with very low losses,  $f_0/\sqrt{1+k} \leq f \leq f_0/\sqrt{1-k}$  [27, 29].

### 5.4.1. Investigation on $|kQ|$ product

In Figs. 5.4.1 and 5.4.2 the quality factor  $Q$  and coupling coefficient  $k$  are shown as a function of the number of turns and for different layer numbers, at  $f_0 = 300\text{kHz}$ . In respect of Figure 5.4.1, the quality factor strongly depends on the geometrical dimensions:  $Q$  tends to increase with the number of turns achieving a peak for any number of layers. Furthermore, the peak augments its value increasing the number of layers (in this case from 23 with  $n=2$  to 35 with  $n=8$ ) and it occurs for a decreasing number of turns. Differently, the magnitude of the coupling coefficient significantly decreases with the number of turns but its value can be considered quite similar increasing the layer numbers.

5. Design of Metamaterial with Multilayer Flat Spiral Resonators for WPT

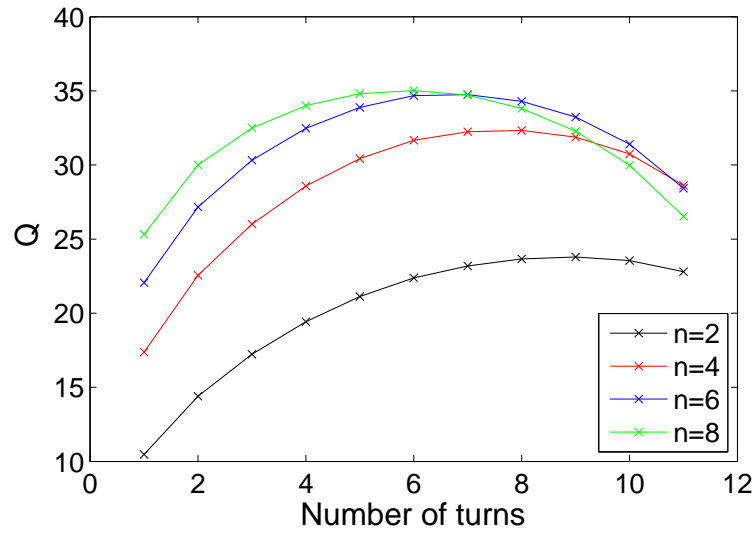


Figure 5.4.1.: Quality factor as a function of the number of turns for different layer numbers.

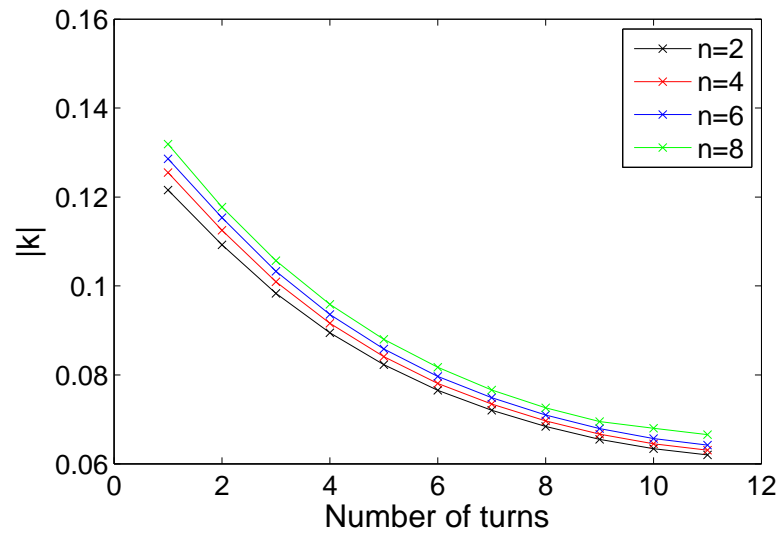


Figure 5.4.2.: Coupling coefficient as a function of the number of turns for different layer numbers.  $|k|$  is performed considering two equal resonators spaced 0.1mm.

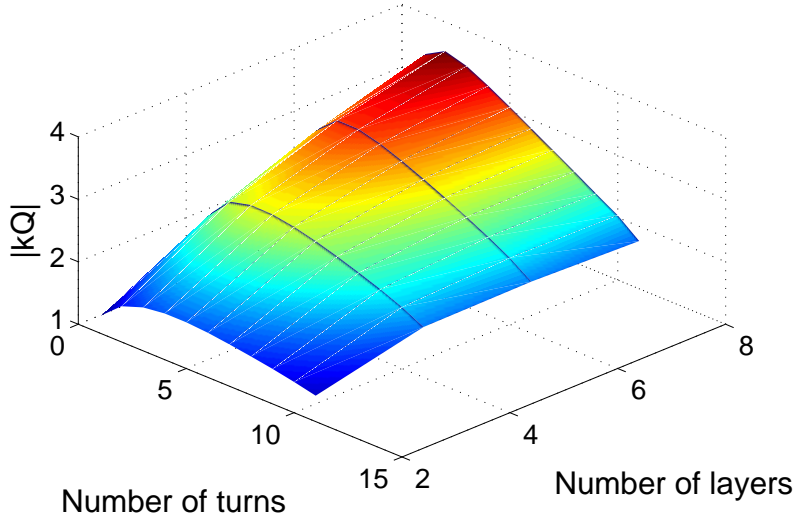


Figure 5.4.3.:  $|kQ|$  product as a function of the number of turns and layers.

However, with respect to (5.4.1), it could be also important to monitor the  $|kQ|$  product as a function of the number of turns and layers. Figure 5.4.3 shows that the  $|kQ|$  product collapses for an high number of turns and its peaks are located for a very low number of turns: in fact, the highest value of the  $|kQ|$  product is achieved for the maximum value of layers ( $n=8$ ) and  $N=2$ .

### 5.4.2. Matching condition

A second important aspect for the metamaterial design is about the matching condition: it is demonstrated that if the receiver is located on the last cell it is possible to set  $Z_d = \frac{(\omega M_{r,i})^2}{R_r + R_{load}} = \omega_0 M$  and match the system at the resonant frequency [38] by adjusting its self-inductance or the mutual inductance between the receiver and the last resonator. Under this condition, a system composed of a number of resonators can be represented with a single impedance in series to the resistance of the first cell whose value is close to  $Z_{eq} = \omega_0 M$  [30]. Furthermore, as noted in literature, the maximum power transmitted is achieved if the input impedance is equal to the complex conjugate of the source impedance. If the source impedance is a resistance  $R_s$ :

$$\text{Re}\{\hat{Z}_{in}\} = R_s. \quad (5.4.2)$$

The input impedance depends on the resonance topology (i.e., series resonance SR or parallel resonance PR, as depicted in Figure 5.4.4) of the first cell by the following expressions

$$\begin{cases} \hat{Z}_{in,SR} = \omega_0 M + R \\ \hat{Z}_{in,PR} = \left( j\omega_0 C + \frac{1}{\omega_0 M + R + j\omega_0 L} \right)^{-1} \end{cases} \quad (5.4.3)$$

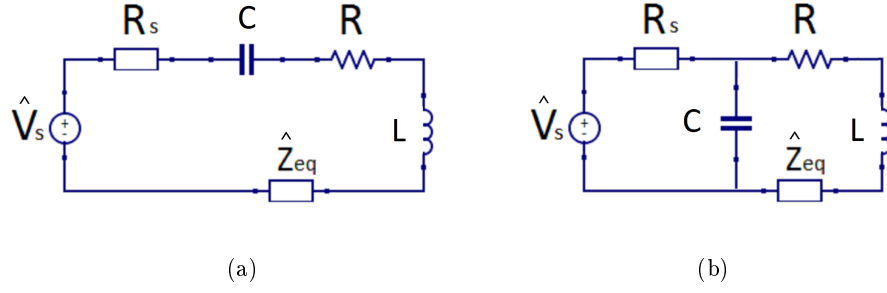


Figure 5.4.4.: Lumped equivalent impedance with the first cell in series (a) and parallel (b) resonance.

at the resonant frequency  $f_0$ .

Consequently, from the equations reported in (5.4.3), it is possible to design the self-inductance of the cell expressing all the parameters as a function of the self-inductance and neglecting the resistance to a first approximation

$$\begin{cases} L_{SR} = \frac{R_s}{\omega_0 k} \\ L_{PR} = \frac{k R_s}{\omega_0 (1+k^2)} \end{cases} \quad (5.4.4)$$

Considering the series resonance SR, the self-inductance  $L_{SR}$  satisfying the condition (5.4.2) is easily calculated from

$$R_s = \text{Re} \left\{ \omega_0 M + R + j \left( \omega L_{SR} - \frac{1}{\omega C} \right) \right\}. \quad (5.4.5)$$

Thus, expressing  $M = kL$  and assuming  $\omega_0 M \gg R$  at  $\omega = \omega_0$ , the input impedance is real and it is possible to obtain

$$L_{SR} = \frac{R_s}{\omega_0 k}. \quad (5.4.6)$$

Considering the parallel resonance PR,  $L_{PR}$  can be calculated from:

$$R_s = \text{Re} \left\{ \left( j\omega C + \frac{1}{(R + \omega_0 M + j\omega L_{PR})} \right)^{-1} \right\}. \quad (5.4.7)$$

Taking the previous considerations into account, at the resonant frequency it is possible to consider that  $\omega_0 C = \frac{1}{\omega_0 L_{PR}}$

$$R_s = \text{Re} \left\{ \left( \frac{j}{\omega_0 L} + \frac{1}{(\omega_0 k L + j\omega_0 L_{PR})} \right)^{-1} \right\} \quad (5.4.8)$$

$$R_s = \text{Re} \left\{ \left( \frac{k}{\omega_0 L_{PR}(k^2 + 1)} + \frac{jk^2}{\omega_0 L_{PR}(k^2 + 1)} \right)^{-1} \right\} \quad (5.4.9)$$

## 5.5. Electromagnetic simulations ( $f_0 = 300\text{kHz}$ )

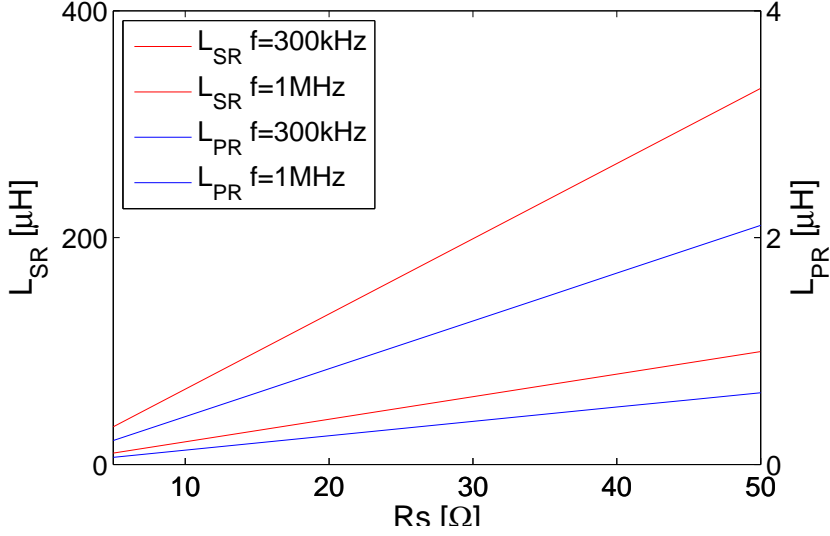


Figure 5.4.5.:  $L_{SR}$  and  $L_{PR}$  designed with (5.4.4) as a function of source resistance and for different frequencies.

hence

$$L_{PR} = \frac{kR_s}{\omega_0(1+k^2)}. \quad (5.4.10)$$

In Figure 5.4.5, the values of the self-inductance for the two different topologies are shown as a function of the source resistance  $R_s$  up to  $50\Omega$ , for different resonant frequencies and coupling coefficient equal to  $k = -0.15$ . It is important to notice that in the parallel topology, the self-inductance is considerably lower, suggesting that the parallel topology can be more effectively used for high value of  $R_s$  or at very low resonant frequency. However, this consideration about  $L$  must take into account the resistance associated to the resonator that should allow good values of  $|kQ|$  to be achieved.

## 5.5. Electromagnetic simulations ( $f_0 = 300\text{kHz}$ )

In this study the metamaterial is tuned to  $300\text{kHz}$  and composed of multilayer flat spiral resonators with one turn ( $N = 1$ ) and four layers ( $n = 4$ ) and whose dimensions are tabulated in Table 5.2. With respect to the Figure 5.4.5, if the source resistance is chosen equal to  $50\Omega$  (like the input source of a network analyzer), the self-inductance of the cell with the lumped capacitance in parallel should be about  $4\mu\text{H}$  and the coupling coefficient at least  $k = -0.15$ . Furthermore, the single cell is designed with large conductor width,  $w$ , and thickness,  $t_c$ , in order to satisfy large quality factor value. Also, the resonator shape is rectangular being  $l$  is the larger external dimension and  $l_m$  the smaller one. The number of turn,  $N$ , and the layers,  $n$ , are chosen to satisfy the considerations made in the previous Section 5.4.1, regarding the maximization of  $|kQ|$  product. Consequently, the single cell presents theoretical values of self-inductance,  $L$ , equal to  $3.87\mu\text{H}$  and AC

## 5. Design of Metamaterial with Multilayer Flat Spiral Resonators for WPT

Table 5.2.: Geometrical dimensions of the single cell of the simulated metamaterial.

| $l$ [mm] | $l_m$ [mm] | $w$ [mm] | $s$ [mm] | $h$ [mm] | $t_c$ [mm] |
|----------|------------|----------|----------|----------|------------|
| 80       | 60         | 4.5      | 2.5      | 0.5      | 0.6        |

resistance equal to  $0.084\Omega$ . In this way the theoretical quality factor  $Q$  at the resonant frequency is 86. Finally, considering the distance between two cell equal to 0.25mm, the predicted coupling coefficient is  $k = -0.12$ , which involves  $\omega_0 M = 0.9\Omega$ .

### 5.5.1. Transmission coefficient and efficiency

The performances of a metamaterial for WPT can be described in terms of transmission coefficient and efficiency [67]. In this Section, a metamaterial is simulated with Sonnet Software, for the first time used for this kind of simulation. Hence, a short metamaterial composed of 5 cells is implemented; its total length is 301mm. Each cell has a lumped capacitance equal to  $C = 75\text{nF}$  connected in parallel with each self-inductance. The first cell is supplied by a port whose internal resistance is  $50\Omega$ . The signal is received by a port with internal resistance setted equal to  $\omega_0 M$  in order to represent the receiver coil ( $Z_d$ ) matched to the metamaterial line. The whole system is represented in Figure 5.5.1.

It is important to underline that the simulations are performed following the consideration introduced in the Chapter 2. Briefly, it consists in the introduction of a termination impedance which is inserted in series with the last cell. By varying its value depending on the position of the second port (i.e., the receiver location) between 0 (when the second port faces the I, III and V cells) and  $Z_T \gg \omega_0 M$  (or non-resonating cell, when the second port is aligned to the II and IV cells), the peaks of transmission coefficient can be obtained along the whole metamaterial at  $f_0$ , as depicted in Figure 5.5.2. Consequently, the maximum efficiency can be obtained for any position of the receiver along the metamaterial and its value is plotted in Figure 5.5.3 as a function of the second port position. As it can be noticed, the simulated efficiency ranges between 60% and 80% and it is calculated through the simulated transmission and reflection coefficients  $S_{21}$  and  $S_{11}$ , respectively

$$\eta = \frac{S_{21}^2}{1 - S_{11}^2}. \quad (5.5.1)$$

5.5. Electromagnetic simulations ( $f_0 = 300\text{kHz}$ )

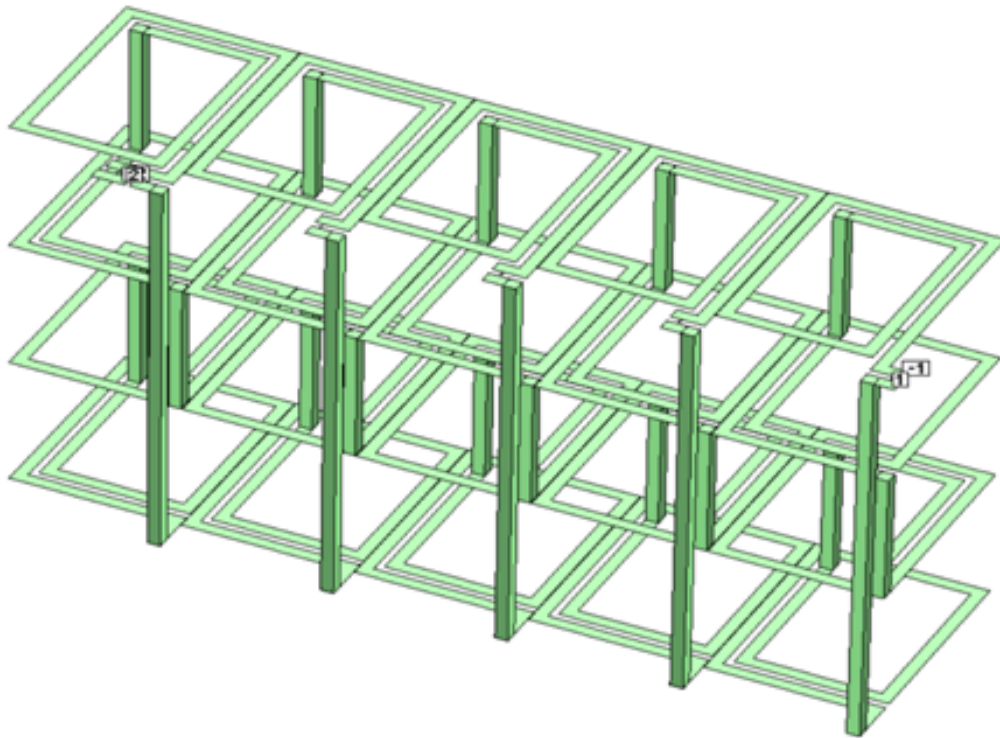


Figure 5.5.1.: Metamaterial composed of 5 cell implemented in Sonnet Software.

5. Design of Metamaterial with Multilayer Flat Spiral Resonators for WPT

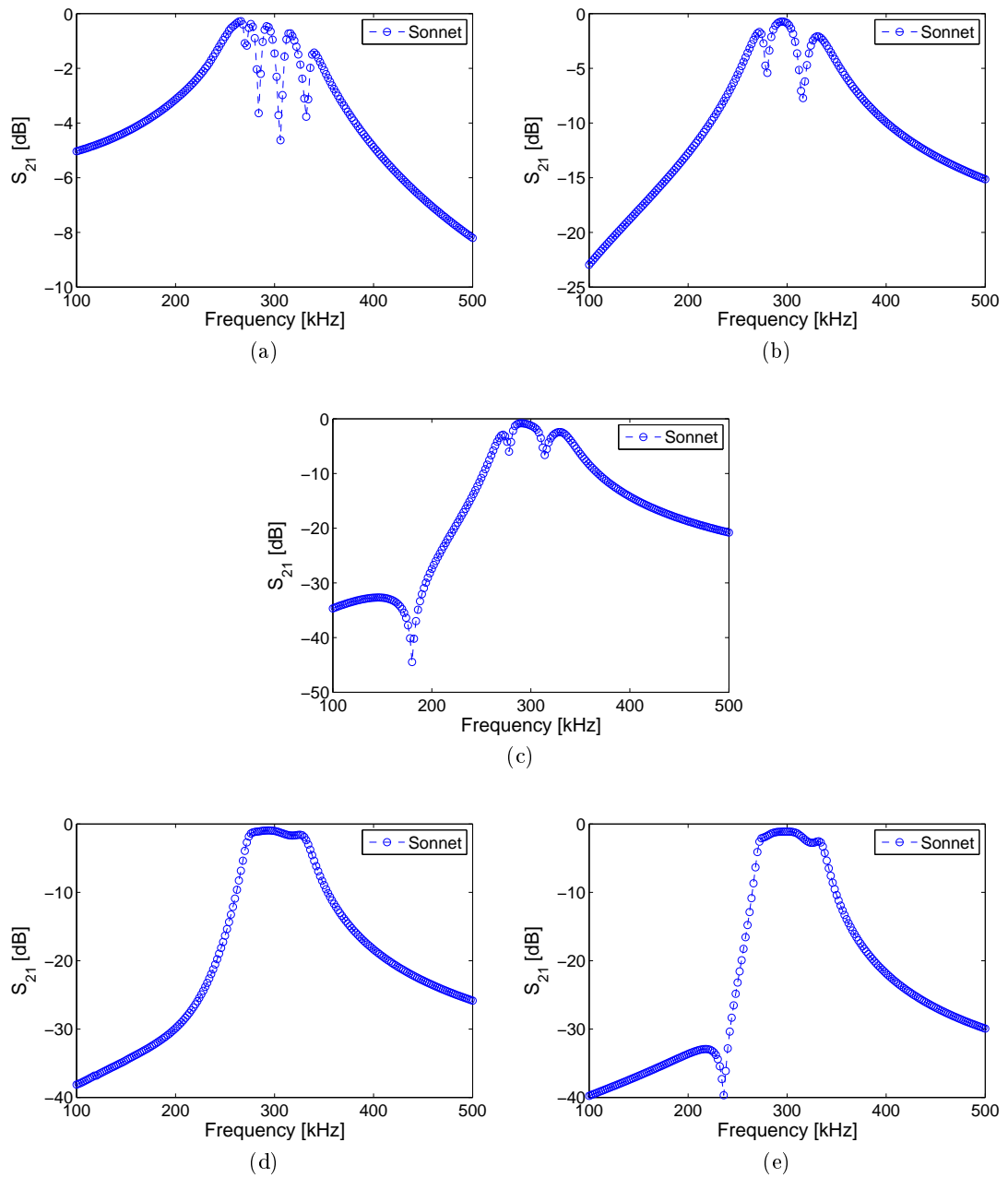


Figure 5.5.2.: Transmission coefficient as a function of frequency when the second port faces the I (a), II (b), III (c), IV (d) and V (e) cell.

5.5. Electromagnetic simulations ( $f_0 = 300\text{kHz}$ )

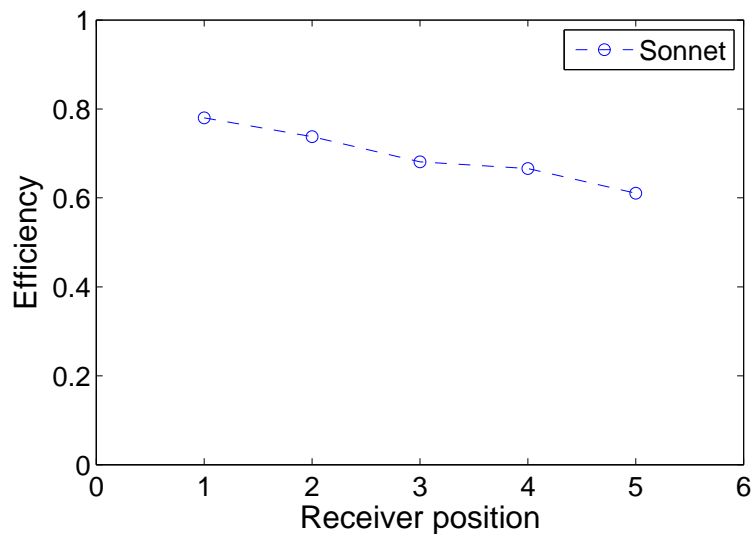


Figure 5.5.3.: Efficiency at  $f_0$  as a function of the second port position.



## 6. Original Contribution and Conclusions

- This thesis presents a deep study regarding Wireless Power Transfer (WPT) systems composed of a number of resonators arranged in a planar configuration (i.e., metamaterial line) and transmitting power to a receiver sliding on them.
- The thesis starts from a circuitual analysis which allows the equivalent and input impedances of the system to be calculated. This study is carried out from an analytical and numerical point of view.
- Two experiments are developed and described in order to analyse the behaviour of the transmitted power along short metamaterial lines. The first verification concerns a system composed of six planar resonators designed to resonate at 20MHz. Two non-resonating coils are used as emitter and receiver and matched using the novel approach based on magnetoinductive waves theory (MIW). In this case, the maximum transmitted power occurs only when the receiver coil is located on the last resonator and this laboratory experience is confirmed for four different arrangements. The second experimental verification is made with five resonators tuned to 13.56MHz whose purpose is to analyse the real effects of the termination impedance on the WPT metamaterial efficiency. Based on previous works of prof. C.J. Stevens, this thesis shows that, by appropriately varying the value of an impedance connected with the last cell of the metamaterial, it is possible to achieve the matching condition and enhance the power transmitted to the receiver along the metamaterial for the same resonant frequency. This study analyses the effects of the termination impedance on the transmission coefficient and efficiency in terms of the receiver position and frequency. All the experimental tests are made with flat spiral resonators and supported by numerical simulations based on formulas proposed by literature.
- A numerical electrical characterization of multilayer and multiturn flat spiral resonators is presented: a novel approach to calculate the alternating current (AC) resistance is proposed (considering skin, proximity and crowding current effects) and self-inductance, stray capacitance and dielectric losses are taken into account. The characterization is made interfacing a numerical code with a finite element one and validated through comparisons with electromagnetic simulations. The numerical characterization is proposed for multilayer and multiturn flat spiral resonators with both square and rectangular shapes. Multilayer flat spiral resonators can achieve large values of self-inductance and a low self-resonant frequency showing the possibility to be applied at low operating frequencies (kHz - a few MHz) in order to be supplied by electronic power converters. Finally, important considerations for

## 6. *Original Contribution and Conclusions*

the design of metamaterial composed of multilayer spiral resonators are detailed in this thesis, particularly with regards to the product between the coupling coefficient magnitude  $|k|$  and Q factor and the self-inductance of the metamaterial cell in order to reduce the losses per cell and match the system. All these considerations are used to design a WPT metamaterial operating at 300kHz: the electromagnetic simulations show an efficiency between 60% and 80% along the metamaterial length.

- Finally, simultaneously to the multilayer flat spiral resonator, the inductance characterization is made and validated with experiments regarding single layer solenoid coils and, especially, planar zig-zag spiral inductors. In particular, it is shown that zig-zag spiral inductors with uniform and nonuniform arms can increase their self-inductance up to 40%, dependently on the spiral angle, mantaining the same external dimensions.

# A. Resistance and Self-inductance of Single Layer Solenoid Coil

*This appendix presents a validation of formulas for calculating the resistance and self-inductance of solenoid coils, used to design the emitter and receiver in Chapter 3. This validation is based on the electrical characterization of a WPT system proposed in [46]. The analytical formulas that calculate the lumped-circuit parameters of the solenoid coils were assessed by comparison to the numerical simulations with Flux 2D. The resistance was calculated per unit length (p.u.l.) for both circular and rectangular cross sections, taking both skin and proximity effect into account. Several calculations of the self-inductance of the coils were carried out varying the coil radius, distance between turns and number of turns. The frequency and geometrical parameters considered in the analysis have the variability intervals shown in Table A.1.*

## Resistance

The resistance of a multiturn coil depends on the distribution of the current over the conductor cross section, which is determined by two factors: the skin effect, which causes for high frequencies a concentration of the current near the outer surfaces of the conductor, and the proximity effect, due to currents in adjacent conductors, which forces the current to the outside edges [68, 69, 70]. The latter is particularly important for systems with several closely spaced conductors, as the variation in the current distribution can increase the resistance of the conductors with a contribution even larger than that produced by the skin effect. The skin effect and proximity effect can be reduced using litz-wire windings [71, 72]. The analytical expression for the resistance which takes both skin effect and proximity effect into account used in the calculations can be written as

$$R = R_s(n + k_p), \tag{A.0.1}$$

Table A.1.: Variability intervals of the frequency and geometrical parameters considered in the analysis.

| Parameter                   | Minimum value | Maximum value |
|-----------------------------|---------------|---------------|
| Frequency                   | 100 kHz       | 300 kHz       |
| Coil radius                 | 10 mm         | 400 mm        |
| Distance between wire turns | 1 mm          | 15 mm         |
| Number of turns             | 2             | 10            |

### A. Resistance and Self-inductance of Single Layer Solenoid Coil

where  $R_s$  is the p.u.l. resistance of a conductor that takes the skin effect into account and  $n$  is the number of adjacent conductors;  $k_p$  is a conventional normalized coefficient which represents the contribution to the resistance value due to the proximity effect. For conductors of circular cross section [73]

$$R_s = \frac{1}{2\pi a} \sqrt{\frac{\mu\omega}{2\sigma}} \quad (\text{A.0.2})$$

where  $\mu$  and  $\sigma$  are the magnetic permeability and electrical conductivity of the conductor, respectively, and  $a$  is the cross-sectional radius of the conductor coil, whereas the coefficient  $k_p$  is a function of the geometry of the coil (number of turns, distance between conductors, coil diameter, etc.)

$$k_p = \frac{1}{2} \sum_{m=1}^n \sum_{s=1}^t |\hat{a}_{ms}|^2. \quad (\text{A.0.3})$$

In (A.0.3)  $t$  is the number of Fourier series terms used to represent the current density. The complex coefficients  $\hat{a}_{ms}$  can be found solving a system of coupled integral equations following the procedure detailed in [74] (method of least squares).

The results of the comparison between the predictions given by (A.0.1) and the numerical calculations with Flux 2D are shown in Figure A.0.1 for the resistance (at the frequency of 180 kHz) versus the coil radius of single-layer solenoid coils with four and ten turns of circular cross section of 5 mm radius. It can be noticed that the resistance calculated with (A.0.1) is constant regardless of the coil radius, whereas that calculated with Flux 2D increases significantly for small values of the radius. An explanation may be that (A.0.3) fails to represent the proximity effect for coils with small radius. The errors decrease increasing the coil radius and are within 10% for radii of practical dimension (radius greater than 10 cm), such as those used in the experiments. For coils with four and ten turns (A.0.1) and Flux 2D are in good agreement for a radius greater than 20 cm and 30 cm, respectively. This results shows that the less the number of turns, the less is the import of the proximity effect in calculating the coil resistance. The calculation is more complex for rectangular cross-section coils, probably because the current is less uniformly distributed than in circular cross-section coils. The error between predictions and Flux 2D ranges between 13 and 15% for radii of practical dimension. In particular, referring to the experimental setup described in [46], the error between the calculations with (A.0.1) and Flux 2D of the resistance of the emitter coil is about 6%, whereas it is larger for the receiver coil (about 13%). The validation of the resistance calculation was completed experimentally for the receiver coil; the measurement resulted in good agreement with (A.0.1). Instead, it was not possible to measure the emitter coil resistance with a good accuracy as the coil terminals were too large with respect to the impedance analyzer clip fixtures to consider the measurement reliable. The validation results are summarized in Table A.2.

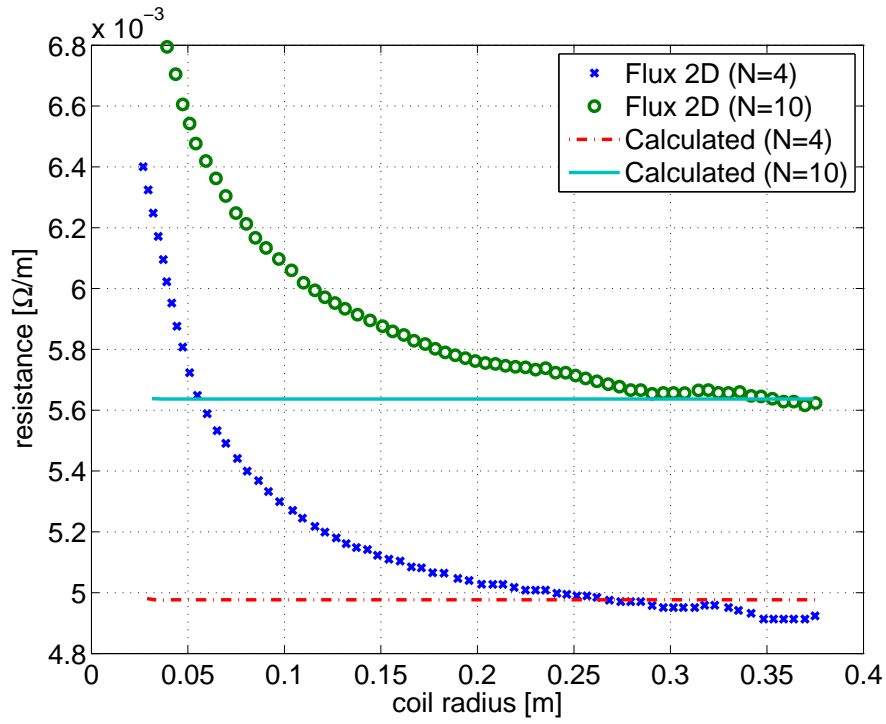


Figure A.0.1.: Resistance versus coil radius of single-layer solenoid coils calculated with (A.0.1) and with Flux 2D (frequency of 180 kHz).

Table A.2.: Calculations and experimental measurements of the emitter and receiver coil resistance (frequency of 180 kHz).

| Coil     | Analytical formula (A.0.1)<br>[mΩ] | Flux 2D<br>[mΩ] | Measurement<br>[mΩ] |
|----------|------------------------------------|-----------------|---------------------|
| Emitter  | 4.97                               | 5.3             | –                   |
| Receiver | 6.53                               | 7.5             | 7.35                |

## A. Resistance and Self-inductance of Single Layer Solenoid Coil

Table A.3.: Self-inductance of emitter and receiver coils calculated and measured.

| Coil     | Analytical formula (A.0.4)<br>[ $\mu\text{H}$ ] | Flux 2D<br>[ $\mu\text{H}$ ] | Measurement<br>[ $\mu\text{H}$ ] |
|----------|---|------------------------------|----------------------------------|
| Emitter  | 0.815   | 0.773                        | 0.860                            |
| Receiver | 1.280   | 1.147                        | 1.262                            |

### Self-inductance

Among the numerous formulas which have been proposed for calculating the self-inductance of single-layer solenoid coils, the predictions closest to the numerical calculations of Flux 2D were obtained with the expressions given by [1, 2, 3]. The comparison was carried out varying the radius, the number of turns and the distance between turns of single-layer solenoid coils. In Figure A.0.2 the self-inductance versus the coil radius of a single-layer solenoid coil (four turns, conductor radius 5 mm and distance between turns 10 mm) calculated according to [1, 2, 3] and with Flux 2D is plotted; the relative error of the analytical calculations with respect to Flux 2D is plotted in Figure A.0.3. The self-inductance versus the number of turns of a single-layer solenoid coil (coil radius of 87.5 mm, conductor radius 5 mm and distance between turns 10 mm) is plotted in Figure A.0.4; the relative error of the analytical calculations with respect to Flux 2D is plotted in Figure A.0.5. The average error for the three analytical formulas with respect to Flux 2D is plotted in Figure A.0.6.

Although it did not always yield the best agreement with Flux 2D calculations, Almeida's formula [3]

$$L = 4\pi 10^{-4} N^2 b \left\{ \ln(1 + \pi F) + \frac{1}{2.3 + 1.6/F + 0.44/F^2} \right\} \quad (\text{A.0.4})$$

was chosen due to its easiness of implementation into the Scilab computer code. In (A.0.4)  $N$  is the number of turns,  $b$  is the coil radius and  $F = b/l$ , with  $l$  the coil axial length. The self-inductance values of the emitter and receiver coils calculated with (A.0.4) were compared to those obtained with both Flux 2D and experimental measurements; the results are reported in Table A.3 and show that the the predictions obtained with (A.0.4) are in very good agreement with the measurement.

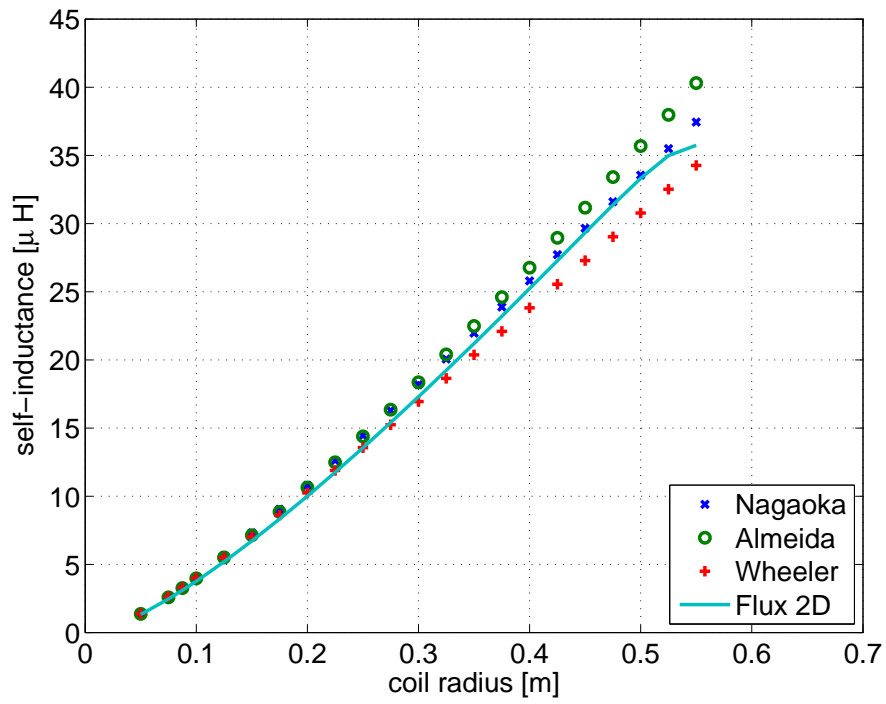


Figure A.0.2.: Self-inductance versus coil radius of a single-layer solenoid coil calculated according to [1, 2, 3] and with Flux 2D.

A. Resistance and Self-inductance of Single Layer Solenoid Coil

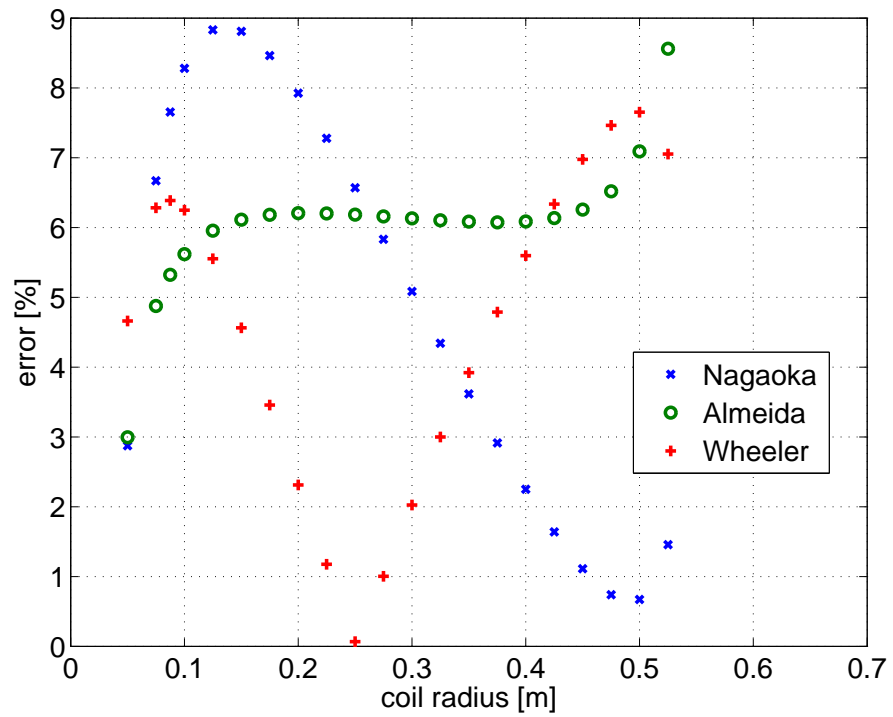


Figure A.0.3.: Relative error of the analytical calculations of Figure A.0.2 with respect to the calculation with Flux 2D.

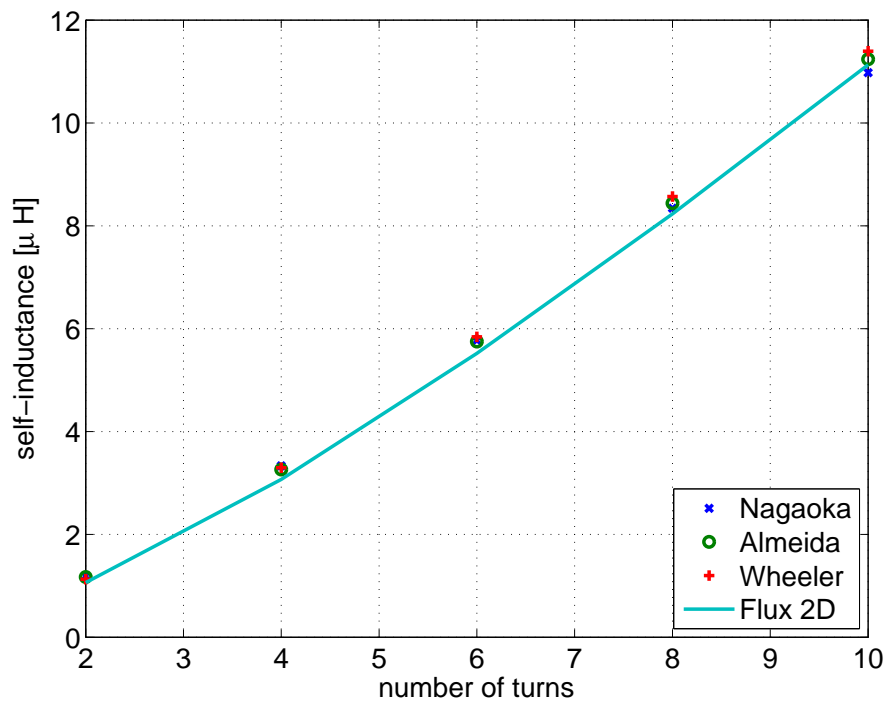


Figure A.0.4.: Self-inductance versus number of turns of a single-layer solenoid coil calculated according to [1, 2, 3] and with Flux 2D.

A. Resistance and Self-inductance of Single Layer Solenoid Coil

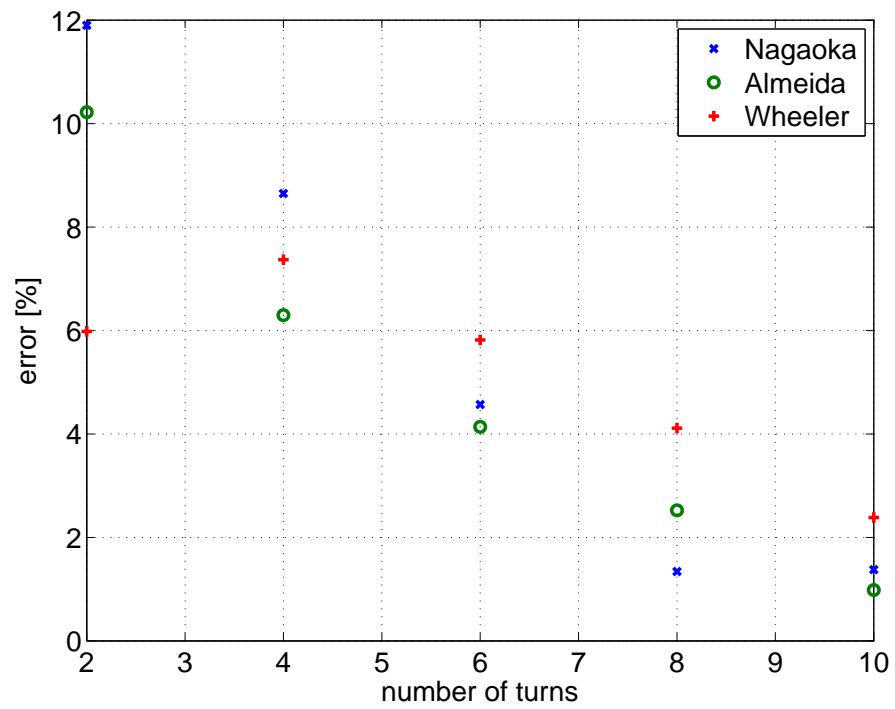


Figure A.0.5.: Relative error of the analytical calculations of Figure A.0.4 with respect to the calculation with Flux 2D.

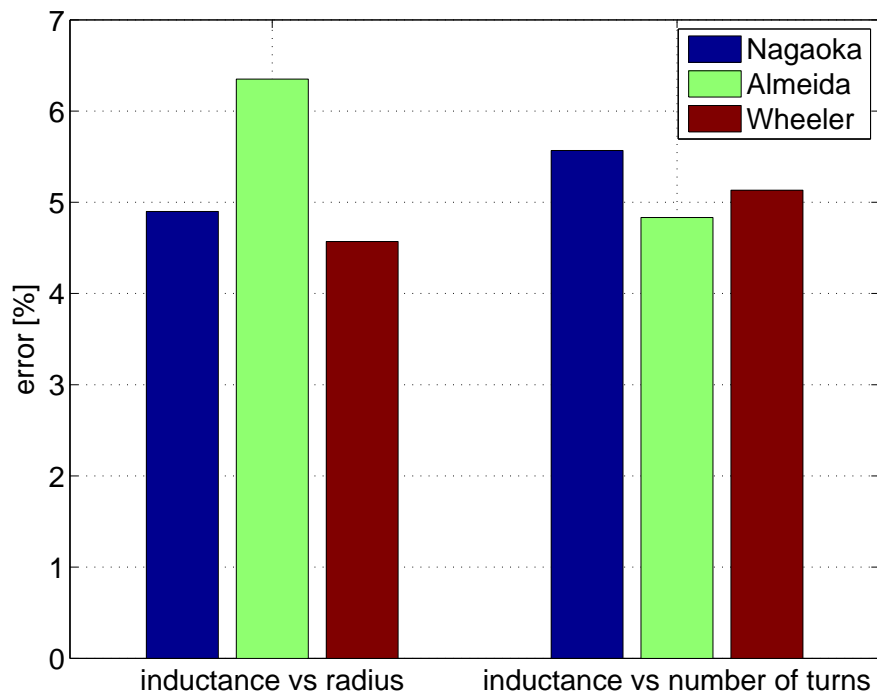


Figure A.0.6.: Average error of the analytical calculations with respect to Flux 2D for the self-inductance of a single-layer solenoid coil.



## B. Inductance of Planar Zig-zag Spiral Inductors with Uniform and Nonuniform Arms

*An analytical procedure for the calculation of the inductance of planar zig-zag spiral inductors is proposed. The procedure is based on the partial inductance concept and models the inductor as a series of a number of parts. The self-inductance of each individual part, which has the shape of a parallelogram, and the mutual inductance between any two parts of the inductor are determined. The inductance of a planar zig-zag spiral inductor can thus be obtained for any width, length and angle of the saw-tooth configuration. The procedure is validated with experimental measurements; the agreement between estimated and measured inductances is very good. Then, the inductances are analysed as a function of the main geometrical dimensions, particularly the spiral angle; also, spiral inductors with nonuniform zig-zag arms are considered. The calculated results of the self-inductance are compared with those obtained by a programme based on magnetoquasistatic analysis showing a good agreement.*

---

In this Appendix, an analytical procedure for the calculation of the inductance of a planar spiral inductor with saw-toothed shaped sides based on the partial inductance concept is presented. This geometry is derived from the spiral antenna with zig-zag arms [75] and its structure is shown in Figure B.0.1. This type of inductor can be of interest in several applications where there is a need to increase the total length of the inductor and its inductance without changing its external dimensions.

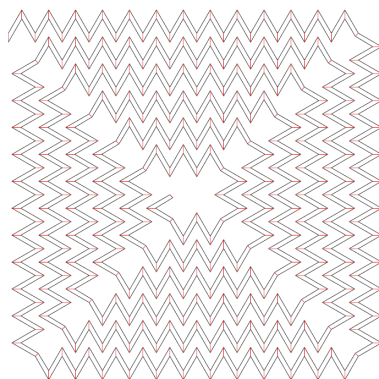


Figure B.0.1.: Planar zig-zag spiral inductor subdivided in  $N$  parts.

B. Inductance of Planar Zig-zag Spiral Inductors with Uniform and Nonuniform Arms

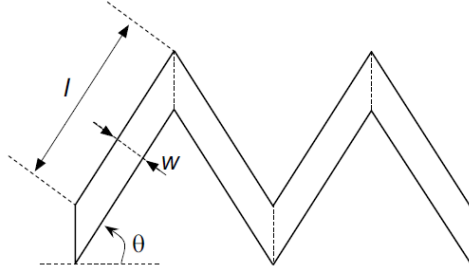


Figure B.0.2.: Particular of a single side with its geometrical dimensions.

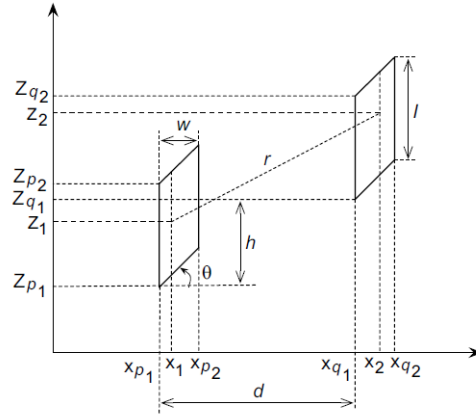


Figure B.0.3.: Two parallel thin parallelograms b).

The zig-zag spiral inductor has a constant cross section of width  $w$  and negligible thickness along its length, as shown in Figure B.0.2.

The angle of the spiral is  $\theta$ , with  $0 \leq \theta < \pi/2$ , and the length of each spiral element is  $l$ . The inductor may then be thought as a bundle of parallel filaments, each of width  $dx$  and carrying a current density constant along the length of each filament. The current density is then assumed uniform throughout the zig-zag spiral inductor. With reference to Figure B.0.3 the partial self-inductance of a thin parallelogram can be evaluated as a four-fold integral from the definition of the partial mutual inductance between two parallel thin parallelograms  $p$  and  $q$  each with a constant current density

$$M_{pq} = \frac{\mu_0}{4\pi} \frac{1}{w_p} \frac{1}{w_q} \times \int_0^{w_p} \int_0^{w_q} \int_0^{l_p} \int_0^{l_q} \frac{dx_1 dx_2 dz_1 dz_2}{\sqrt{(x_2 - x_1 + d)^2 + [z_2 - z_1 + (x_2 - x_1) \tan \theta + s]^2}} \quad (\text{B.0.1})$$

where  $\mu_0$  is the magnetic permeability of free space,  $w_p$ ,  $l_p$  and  $w_q$ ,  $l_q$  are the width

and the length of the parallelograms  $p$  and  $q$ , respectively,  $d = x_{q_1} - x_{p_1}$  and  $s = z_{q_1} - z_{p_1}$ . As the current density is assumed constant along the length of each filament, the partial mutual inductance between two filaments of the two parallelograms is given by Neumann's formula

$$M_f = \frac{\mu_0}{4\pi} \int_0^{l_1} \int_0^{l_2} \frac{dz_1 dz_2}{r} \quad (\text{B.0.2})$$

where  $r$  is the distance between two elements of length  $dz_1$  and  $dz_2$  of the two filaments of length  $l_1$  and  $l_2$ , respectively.

The partial self-inductance of a thin parallelogram can be found from (B.0.1) by performing the integration over the same area. The two parallelograms  $p$  and  $q$  are then the same, and thus letting  $w_p = w_q = w$ ,  $l_p = l_q = l$ ,  $d = 0$  and  $s = 0$  in (B.0.1) we get the expression for the partial self-inductance  $L_p = M_{pp}$  of a thin parallelogram as

$$L_p = \frac{\mu_0}{4\pi} \frac{1}{w^2} \int_0^w \int_0^w \int_0^l \int_0^l \frac{dx_1 dx_2 dz_1 dz_2}{\sqrt{(x_2 - x_1)^2 + [z_2 - z_1 + (x_2 - x_1) \tan \theta]^2}}. \quad (\text{B.0.3})$$

In general, the solution of the four-fold integration is obtained by introducing new variables  $u = x_2 - x_1$  and  $v = z_2 - z_1$  which yields the expression

$$L_p = \frac{\mu_0}{4\pi} \frac{1}{w^2} \int_0^w dx_1 \int_{-x_1}^{w-x_1} du \int_0^l dz_1 \int_{-z_1}^{l-z_1} \frac{dv}{\sqrt{u^2 + (v + u \tan \theta)^2}}. \quad (\text{B.0.4})$$

The partial self-inductance of a thin parallelogram of width  $w$  and length  $l$  is then

$$\begin{aligned} L_p = & \frac{\mu_0}{4\pi} \frac{1}{6w^2} \left[ 4t \left( w^3 + \frac{l^3}{F_5^3} \right) \log(F_5 - t) + 4w^3 F_5 + \frac{4l^3}{F_5^2} \right. \\ & - 2(F_1 + F_2) \left( w^2 + \frac{l^2}{F_5^2} \right) + 2w^2(3l + wt) \log\left(\frac{wt + F_1 + l}{w}\right) \\ & + 2w^2(3l - wt) \log\left(\frac{-wt + F_2 + l}{w}\right) + \frac{6wl^2}{F_5} \log\left(\frac{F_1 F_5 + F_3}{l}\right) \\ & \left. + \frac{6wl^2}{F_5} \log\left(\frac{F_2 F_5 + F_4}{l}\right) + \frac{2l^3 t}{F_5^3} \log\left(\frac{F_1 F_5 + F_3}{F_2 F_5 + F_4}\right) \right] \end{aligned} \quad (\text{B.0.5})$$

where

$$\begin{aligned} F_1 &= \sqrt{w(wt^2 + w + 2lt) + l^2}, \\ F_2 &= \sqrt{w(wt^2 + w - 2lt) + l^2}, \\ F_3 &= wt^2 + w + lt, \\ F_4 &= wt^2 + w - lt, \\ F_5 &= \sqrt{t^2 + 1}, \end{aligned}$$

and  $t = \tan \theta$ . It can be verified that (B.0.5) reduces to the expression of the self-inductance of a thin rectangle [60, 63, 76, 77] for  $t = 0$ .

It is not straightforward to find a closed form expression for the partial mutual inductance between any two parallel thin parallelograms  $p$  and  $q$  of the planar spiral inductor. An approximation can then be adopted for the parallelograms, which are represented as straight filaments. The segments forming the axis of the planar zig-zag spiral inductor

may be chosen as the filaments representing the parallelograms, as Figure B.0.4 shows. The partial mutual inductance between two parallelograms can then be calculated as the partial mutual inductance between two filaments, which is given by the Neumann's formula (B.0.2). Campbell [78] first proposed a general solution of the Neumann integral for any two straight wires with negligible thickness in any relative location in space. Here we propose the solutions in a form more suitable for implementation in a computer code. There are three possible configurations for any two filaments of a planar zig-zag spiral inductor: i) the filaments are parallel, ii) the filaments are incident at a point forming an angle to each other, iii) the filaments are perpendicular. The last case is the simplest as the partial mutual inductance between any two perpendicular filaments is always zero. The possible filament configurations are shown in Figure B.0.5(a) and (b).

### Partial mutual inductance between parallel straight filaments

The partial mutual inductance  $M_{pf}$  between any two parallel filaments  $AB$ ,  $ab$  in any relative position in space can be found from Neumann's formula (B.0.2), where  $r^2 = Pp^2 + (S - s)^2$ . With reference to Figure B.0.5(a),  $P \equiv A$ ,  $Pp$  is the common perpendicular of the two filaments,  $S$  and  $s$  are the distances from the common perpendicular  $Pp$  of the two elements  $dS$  and  $ds$  in the positive directions along  $AB$  and  $ab$ , respectively. From [78], we find

$$\begin{aligned}
 M_{pf} = & \frac{\mu_0}{4\pi} \left[ \sqrt{(pa - PA)^2 + Pp^2} - \sqrt{(pb - PA)^2 + Pp^2} \right. \\
 & - \sqrt{(pa - PB)^2 + Pp^2} + \sqrt{(pb - PB)^2 + Pp^2} \\
 & + (PA - pa) \log \left( \sqrt{(pa - PA)^2 + Pp^2} + pa - PA \right) \\
 & - (PA - pb) \log \left( \sqrt{(pb - PA)^2 + Pp^2} + pb - PA \right) \\
 & - (PB - pa) \log \left( \sqrt{(pa - PB)^2 + Pp^2} + pa - PB \right) \\
 & \left. + (PB - pb) \log \left( \sqrt{(pb - PB)^2 + Pp^2} + pb - PB \right) \right]
 \end{aligned} \tag{B.0.6}$$

that being  $PA = 0$  can be simplified as

$$\begin{aligned}
 M_{pf} = & \frac{\mu_0}{4\pi} \left[ \sqrt{pa^2 + Pp^2} - \sqrt{pb^2 + Pp^2} \right. \\
 & - \sqrt{(pa - PB)^2 + Pp^2} + \sqrt{(pb - PB)^2 + Pp^2} \\
 & - pa \log \left( \sqrt{pa^2 + Pp^2} + pa \right) \\
 & + pb \log \left( \sqrt{pb^2 + Pp^2} + pb \right) \\
 & - (PB - pa) \log \left( \sqrt{(pa - PB)^2 + Pp^2} + pa - PB \right) \\
 & \left. + (PB - pb) \log \left( \sqrt{(pb - PB)^2 + Pp^2} + pb - PB \right) \right].
 \end{aligned} \tag{B.0.7}$$

A particular case of this configuration occurs when the two filaments are aligned and offset. In this case,  $P \equiv A \equiv p$  and thus  $Pp = PA = 0$  so that (B.0.7) reduces to

$$M_{pf} = \frac{\mu_0}{4\pi} [-pa \log(2pa) - (PB - pa) \log 2(pa - PB) + pb \log(2pb) + (PB - pb) \log 2(pb - PB)]. \quad (\text{B.0.8})$$

## Partial mutual inductance between straight filaments incident at an angle

The general case of the partial mutual inductance  $M_{if}$  between any two coplanar filaments  $AB$ ,  $ab$  incident at an angle  $\theta$  that do not share a common point can be derived from Neumann's formula (B.0.2), where  $r^2 = S^2 - 2Ss \cos \theta + s^2$ . In fact, with reference to Figure B.0.5(b),  $P \equiv p$  and then  $Pp = 0$ ;  $S$  and  $s$  are the distances from the point  $P \equiv p$  of the two elements  $dS$  and  $ds$  in the positive directions along  $AB$  and  $ab$ , respectively. From [78], we get

$$M_{if} = \frac{\mu_0}{4\pi} \cos \theta \left[ pa \log \left( \sqrt{-2paPA \cos \theta + pa^2 + PA^2} - pa \cos \theta + PA \right) + PA \log \left( \sqrt{-2paPA \cos \theta + pa^2 + PA^2} - PA \cos \theta + pa \right) - pa \log \left( \sqrt{-2paPB \cos \theta + pa^2 + PB^2} - pa \cos \theta + PB \right) - PB \log \left( \sqrt{-2paPB \cos \theta + pa^2 + PB^2} - PB \cos \theta + pa \right) - PA \log \left( \sqrt{-2PApb \cos \theta + PA^2 + pb^2} - PA \cos \theta + pb \right) - pb \log \left( \sqrt{-2PApb \cos \theta + PA^2 + pb^2} - pb \cos \theta + PA \right) + pb \log \left( \sqrt{-2pbPB \cos \theta + pb^2 + PB^2} - pb \cos \theta + PB \right) + PB \log \left( \sqrt{-2pbPB \cos \theta + pb^2 + PB^2} - PB \cos \theta + pb \right) \right]. \quad (\text{B.0.9})$$

The case of two filaments starting from a common point is readily available from (B.0.9) letting  $P \equiv p \equiv A \equiv a$  and thus  $PA = pa = 0$ :

$$M_{if} = \frac{\mu_0}{4\pi} \cos \theta [-PB \log(PB(1 - \cos \theta)) - pb \log(pb(1 - \cos \theta)) + pb \log \left( \sqrt{-2pbPB \cos \theta + pb^2 + PB^2} - pb \cos \theta + PB \right) + PB \log \left( \sqrt{-2pbPB \cos \theta + pb^2 + PB^2} - PB \cos \theta + pb \right)]. \quad (\text{B.0.10})$$



Figure B.0.4.: Planar zig-zag spiral inductor with its axis.

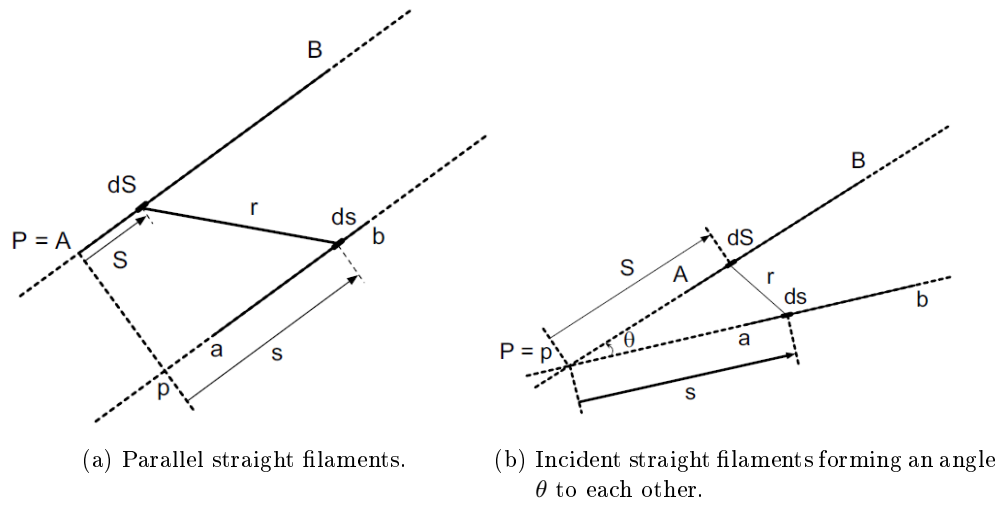


Figure B.0.5.: Configurations of any two filaments of a planar zig-zag spiral inductor.

## Results

The total inductance of a planar zig-zag spiral inductor is then calculated using (B.0.5) for the partial self-inductance of the individual parts of the inductor and (B.0.7), (B.0.9) for the partial mutual inductance between any two parts of the inductor. The procedure was implemented in a Matlab™ computer code. In the calculation we proceed through the elements of the spiral inductor in one of the two possible directions. For example, choosing the clockwise direction, we start from the part in the top left corner of the planar zig-zag spiral inductor (see Figure B.0.4). The zig-zag spiral inductor is defined through the overall dimension of the outer side,  $l_0$ , the width  $w$  and spacing  $s$  of the lands, the angle of the spiral,  $\theta$ , and the number of turns,  $n$ . According to the geometrical dimensions, the outer and inner contours of the spiral are built in a cartesian coordinate system, from which the axis is obtained. The axis is subdivided into segments, each one corresponding to an individual parallelogram of the zig-zag spiral inductor; the coordinates of the start and end points of each segment, as well as the angle the segment connecting the two points makes with the positive  $x$  axis, are collected in an array. A  $N \times N$  matrix of the partial self- and mutual inductances of the  $N$  spiral parts is then built. For each individual parallelogram of the spiral inductor, the partial self-inductance is calculated with (B.0.5). The partial mutual inductance between the straight filaments representing any two parallelograms of the spiral is calculated as follows. In case the filaments are parallel, the code calculates the projection of the point  $P \equiv A$  of the segment  $AB$  on the segment  $ab$  (see Figure B.0.5(a)) and calculates the partial mutual inductance with (B.0.7). If the two segments  $AB$  and  $ab$  belong to the same line, then the code calculates the partial mutual inductance with (B.0.8). For filaments incident at an angle different than  $\pi/2$ , the intersection between the lines connecting  $A$  and  $B$  and  $a$  and  $b$  is found (point  $P \equiv p$ , see Figure B.0.5(b)), and the partial mutual inductance is given by (B.0.9). If the filaments  $AB$  and  $ab$  are incident and share a common point (viz.,  $P \equiv p \equiv A \equiv a$ ), the partial mutual inductance is calculated with (B.0.10). Differently, the partial mutual inductance is equal to zero if the filaments are perpendicular. The partial self- and mutual inductances of the planar zig-zag spiral parts are then collected in a  $N \times N$  symmetric matrix  $\mathbf{L}_p$

$$\mathbf{L}_p = \begin{bmatrix} L_{p1} & M_{p12} & \cdots & M_{p1i} & \cdots & M_{p1j} & \cdots & M_{p1N} \\ M_{p12} & L_{p2} & \cdots & M_{p2i} & \cdots & M_{p2j} & \cdots & M_{p2N} \\ \vdots & \vdots & \ddots & \vdots & \ddots & \vdots & \ddots & \vdots \\ M_{p1i} & M_{p2i} & \cdots & L_{pi} & \cdots & M_{pij} & \cdots & M_{piN} \\ \vdots & \vdots & \ddots & \vdots & \ddots & \vdots & \ddots & \vdots \\ M_{p1j} & M_{p2j} & \cdots & M_{pij} & \cdots & L_{pj} & \cdots & M_{pjN} \\ \vdots & \vdots & \ddots & \vdots & \ddots & \vdots & \ddots & \vdots \\ M_{p1N} & M_{p2N} & \cdots & M_{piN} & \cdots & M_{pjN} & \cdots & L_{pN} \end{bmatrix} \quad (\text{B.0.11})$$

where  $L_{pi}$  is the partial self-inductance of the element  $i$ , and  $M_{pij}$  is the partial mutual inductance between the elements  $i$  and  $j$ . The sum of the elements of  $\mathbf{L}_p$  along any  $i$ th row or column yields the partial inductance of the  $i$ th part of the planar zig-zag spiral

## B. Inductance of Planar Zig-zag Spiral Inductors with Uniform and Nonuniform Arms

inductor; the sum of all the elements of  $\mathbf{L}_p$  yields the total inductance of the planar zig-zag spiral inductor

$$L_{ZSI} = \sum_{i=1}^M \sum_{j=1}^M M_{pij} \quad (\text{B.0.12})$$

The analytical calculations are validated by means of measurements carried out with an Agilent 4263B LCR impedance analyzer, at the operating frequency of 100 Hz. Seven planar zig-zag spiral inductor samples were fabricated with the photochemical etching technique. The characteristics of the samples are summarized in Table B.1. Samples I, II and III have the same overall dimension of the outer side, same land width and spacing between lands of adjacent turns; their angles are  $\pi/6$ ,  $\pi/4$  and  $\pi/3$ , respectively. With these geometrical parameters, the three samples have different number of turns (11, 9 and 6, respectively), and different number of parts (1056, 720 and 336, respectively). Samples IV, V and VI have the same overall dimension of the outer side and are designed in order to have the same number of turns and parts being their angles  $\pi/6$ ,  $\pi/4$  and  $\pi/3$ , respectively. To obtain this, they present different land width and spacing between lands of adjacent turns. Sample VII was built with a larger outer dimension than all other samples and an angle of  $\pi/3$ . Samples I to VI are shown clockwise from the top left in Figure B.0.6. The calculations and measurements of the inductance of the planar zig-zag spiral inductors are collected in Table B.1; as it can be noticed, the comparison shows a very good agreement. Table B.2 shows the comparison between the partial self-inductance values of each part of the considered planar zig-zag spiral inductors obtained with the exact expression (B.0.5),  $L_{\text{exact}}$ , and approximated with the self-inductance of a rectangle,  $L_{\text{rectangle}}$ . It can be noticed that the use of the exact expression (B.0.5) allows a minor error in the calculation of the total inductance of the planar zig-zag spiral inductor. As it can be expected, the difference between the partial self-inductance of a parallelogram calculated with (B.0.5) and that of a rectangle increases with the angle of the parallelogram, as Table (B.3) shows.

### Inductance VS Spiral angle (Nonuniform Zig-zag Arms)

The results presented in this section are given in order to analyse the variation of the inductances as a function of the main geometrical dimensions, in particular the spiral angle. The developed procedure was implemented in a Matlab™ computer code and the calculations of the self-inductance were validated with the FastHenry programme [79], a multipole-accelerated 3D inductance extraction programme based on magnetoquasistatic analysis.

In Table B.4, the comparison between the self-inductance values obtained with the proposed procedure,  $L_{ZSI}$ , and FastHenry,  $L_{ZSI, FH}$ , for two different types of planar zig-zag spiral inductors with different outer dimension, land width and spacing are reported for various spiral angles. With reference to this table,  $n$  is the number of turns,  $N$  is the number of elements for each zig-zag spiral,  $l_o$  is the outer dimension of the inductor,  $w$  and  $s_l$  are the width of the land and the spacing between adjacent lands, respectively, and

Table B.1.: Comparison between the total inductance values obtained with (B.0.12),  $L_{ZSI}$ , and with experimental measurements,  $L_{ZSI,m}$ .

| Sample | $n$ | $N$  | $l_0$<br>[mm] | $\theta$ | $w$<br>[mm] | $s$<br>[mm] | $L_{ZSI}$<br>[ $\mu H$ ] | $L_{ZSI,m}$<br>[ $\mu H$ ] |
|--------|-----|------|---------------|----------|-------------|-------------|--------------------------|----------------------------|
| I      | 11  | 1056 | 60            | $\pi/6$  | 1.0         | 1.2         | 3.34                     | 3.5                        |
| II     | 9   | 720  | 60            | $\pi/4$  | 1.0         | 1.2         | 2.51                     | 2.6                        |
| III    | 6   | 336  | 60            | $\pi/3$  | 1.0         | 1.2         | 1.54                     | 1.5                        |
| IV     | 12  | 1248 | 80            | $\pi/6$  | 1.0         | 1.7         | 5.35                     | 5.7                        |
| V      | 12  | 1248 | 80            | $\pi/4$  | 1.0         | 1.2         | 5.54                     | 5.6                        |
| VI     | 12  | 1248 | 80            | $\pi/3$  | 0.7         | 0.9         | 6.88                     | 6.4                        |
| VII    | 14  | 1680 | 130           | $\pi/3$  | 0.9         | 1.1         | 14.13                    | 13.5                       |

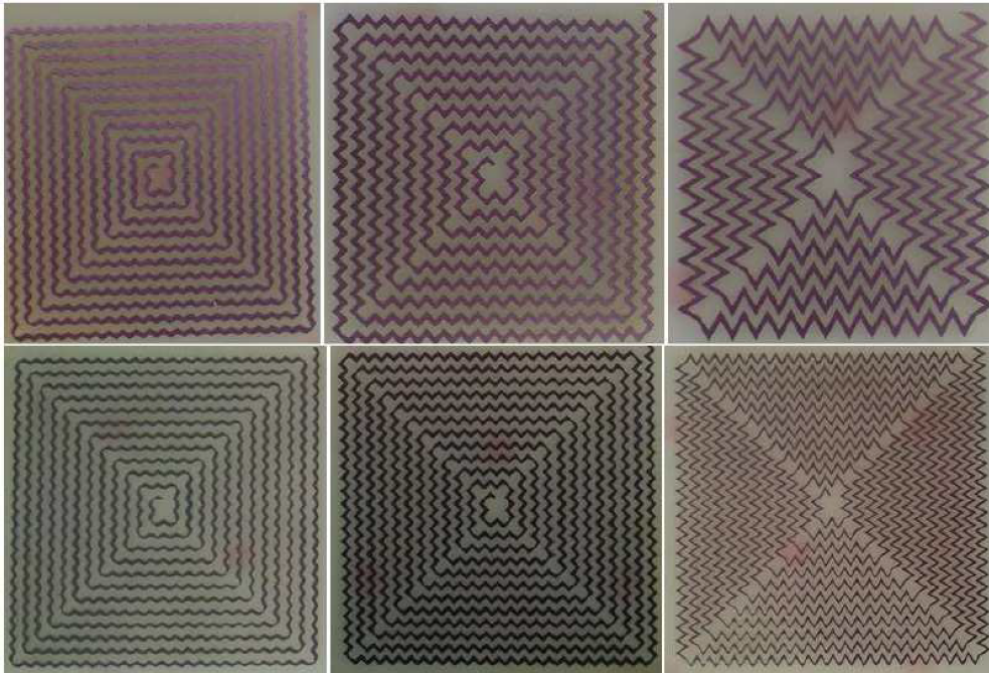


Figure B.0.6.: Samples I to VI of planar zig-zag spiral inductors of Table B.1.

B. Inductance of Planar Zig-zag Spiral Inductors with Uniform and Nonuniform Arms

Table B.2.: Comparison between partial self-inductance values of each part of the planar zig-zag spiral inductor obtained with the exact expression (B.0.5),  $L_{\text{exact}}$ , and approximated with the partial self-inductance of a rectangle,  $L_{\text{rectangle}}$ .

| Sample | $l_0$<br>[mm] | $\theta$ | $w$<br>[mm] | $l$<br>[mm] | $L_{\text{exact}}$<br>[nH] | $L_{\text{rectangle}}$<br>[nH] |
|--------|---------------|----------|-------------|-------------|----------------------------|--------------------------------|
| I      | 60            | $\pi/6$  | 1.0         | 1.47        | 0.516                      | 0.523                          |
| II     | 60            | $\pi/4$  | 1.0         | 2.2         | 0.911                      | 0.935                          |
| III    | 60            | $\pi/3$  | 1.0         | 4.4         | 2.35                       | 2.42                           |
| IV     | 80            | $\pi/6$  | 1.0         | 1.8         | 0.695                      | 0.703                          |
| V      | 80            | $\pi/4$  | 1.0         | 2.2         | 0.911                      | 0.935                          |
| VI     | 80            | $\pi/3$  | 0.7         | 3.2         | 1.73                       | 1.78                           |
| VII    | 130           | $\pi/3$  | 0.9         | 4.35        | 2.32                       | 2.39                           |

Table B.3.: Partial self-inductance [nH] of parallelograms of different dimensions calculated with (B.0.5) as a function of the angle  $\theta$ .

| $\theta$       | $w = 1, l = 10$<br>[mm] | $w = 1, l = 20$<br>[mm] | $w = 2, l = 20$<br>[mm] |
|----------------|-------------------------|-------------------------|-------------------------|
| $\arctan(0.0)$ | 7.06                    | 5.74                    | 14.11                   |
| $\arctan(0.5)$ | 7.05                    | 5.72                    | 14.1                    |
| $\arctan(1.0)$ | 7.03                    | 5.68                    | 14.06                   |
| $\arctan(1.5)$ | 7.00                    | 5.62                    | 13.99                   |
| $\arctan(2.0)$ | 6.95                    | 5.54                    | 13.91                   |
| $\arctan(2.5)$ | 6.91                    | 5.45                    | 13.81                   |
| $\arctan(3.0)$ | 6.85                    | 5.36                    | 13.71                   |
| $\arctan(3.5)$ | 6.80                    | 5.25                    | 13.59                   |
| $\arctan(4.0)$ | 6.73                    | 5.15                    | 13.47                   |

Table B.4.: Comparison between the self-inductance values obtained with the proposed procedure,  $L_{ZSI}$ , and with FastHenry,  $L_{ZSI, FH}$ .

| Sample | $n$ | $N$  | $l_0$<br>[mm] | $w$<br>[mm] | $s_l$<br>[mm] | $\theta$ | $L_{ZSI}$<br>[ $\mu H$ ] | $L_{ZSI, FH}$<br>[ $\mu H$ ] |
|--------|-----|------|---------------|-------------|---------------|----------|--------------------------|------------------------------|
| I      | 11  | 44   | 50            | 1.0         | 1.2           | 0        | 2.52                     | 2.38                         |
| II     | 11  | 1056 | 50            | 1.0         | 1.2           | $\pi/6$  | 2.82                     | 2.85                         |
| III    | 11  | 1056 | 50            | 1.0         | 1.2           | $\pi/4$  | 2.97                     | 2.97                         |
| IV     | 11  | 1056 | 50            | 1.0         | 1.2           | $\pi/3$  | 3.55                     | 3.23                         |
| V      | 11  | 44   | 100           | 2.0         | 2.4           | 0        | 5.03                     | 4.76                         |
| VI     | 11  | 1056 | 100           | 2.0         | 2.4           | $\pi/6$  | 5.65                     | 5.70                         |
| VII    | 11  | 1056 | 100           | 2.0         | 2.4           | $\pi/4$  | 5.95                     | 5.95                         |
| VIII   | 11  | 1056 | 100           | 2.0         | 2.4           | $\pi/3$  | 7.09                     | 6.47                         |

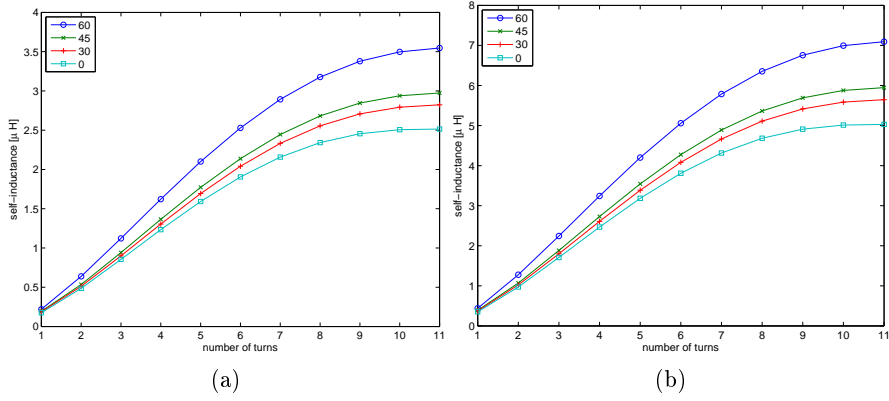


Figure B.0.7.: Self-inductance values of the inductors listed in Table B.4. (a) Samples I-IV, (b) Samples V-VIII.

Table B.5.: Mutual inductance and coupling coefficient values obtained with the proposed procedure for some sample configurations.

| Sample 1 | Sample 2 | $M$<br>[ $\mu H$ ] | $ k $ |
|----------|----------|--------------------|-------|
| V        | V        | -0.094             | 0.019 |
| VI       | VI       | -0.090             | 0.016 |
| VII      | VII      | -0.104             | 0.018 |
| VIII     | VIII     | -0.115             | 0.016 |
| VIII     | VI       | -0.091             | 0.014 |

B. Inductance of Planar Zig-zag Spiral Inductors with Uniform and Nonuniform Arms

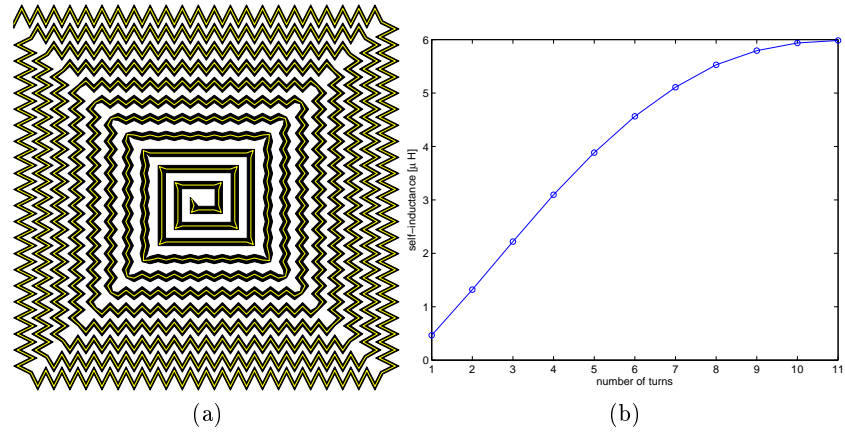


Figure B.0.8.: Nonuniform planar zig-zag spiral inductor. (a) Layout (b) Self-inductance as a function of the turn number.

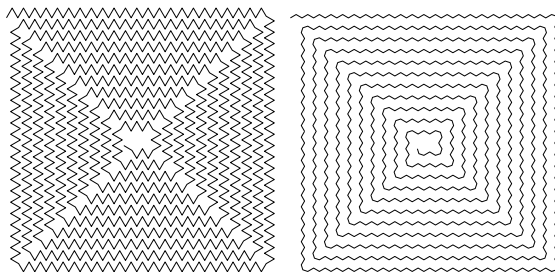


Figure B.0.9.: Layout for the mutual inductance calculation between samples VIII and VI.

$\theta$  is the spiral angle. The self-inductance values obtained with the proposed procedure are thus in good agreement with those obtained by FastHenry. As it can be noted, the values of the self-inductance significantly increase with the spiral angle: for example, for the inductor with  $l_o = 50$  mm,  $L_{ZSI}$  changes from about  $2.52 \mu\text{H}$  to  $3.55 \mu\text{H}$  for  $\theta = 0$  and  $\theta = \pi/3$ , respectively, with an increase of about 40%. The increase is also appreciable in Figure B.0.7, where the self-inductance values of the same inductors listed in Table B.4 are plotted as a function of the turn number. It can also be noticed that doubling the outer dimension, the inductance values also double.

Figure B.0.8(a) shows a planar zig-zag spiral inductor with nonuniform arms; the geometrical dimensions are the same of the samples V-VIII. The spiral angle varies linearly from  $\pi/3$  to 0 with steps of  $\pi/30$ . The self-inductance versus the turn number is plotted in Figure B.0.8(b). For  $n = 11$  the self-inductance obtained with the proposed procedure is  $5.98 \mu\text{H}$ , whereas the one obtained with FastHenry is  $5.75 \mu\text{H}$ . Hence, it is shown that the self-inductance increases significantly with the spiral angle (40% passing from  $\theta = 0$  to  $\theta = \pi/3$ ), with fixed outer dimension, land width and spacing and number of turns. The absolute value of the mutual inductance between zig-zag spiral inductors also increases with the angle, although the magnetic coupling is highest for  $\theta = 0$ .



# Bibliography

- [1] N. H., “The inductance coefficients of solenoids,” *Journal of Colloid Science*, vol. 27, pp. 18–33, 1909.
- [2] H. Wheeler, “Simple inductance formulas for radio coils,” *Proceedings of the Institute of Radio Engineers*, vol. 16, no. 10, pp. 1398–1400, Oct 1928.
- [3] A. F., *Calcoil, [Computer Software] version 2.0*, 2002.
- [4] W. C. Brown, “The history of wireless power transmission,” *Solar Energy*, vol. 56, no. 1, pp. 3 – 21, 1996, wireless Power Transmission. [Online]. Available: <http://www.sciencedirect.com/science/article/pii/S038092X9500080B>
- [5] J. Maxwell, *A treatise on electricity and magnetism*, ser. A Treatise on Electricity and Magnetism. Dover Publications, 1954, no. v. 1-2. [Online]. Available: <http://books.google.it/books?id=HbUPAQAAMAAJ>
- [6] N. Tesla, “System of transmission of electrical energy.” Mar. 20 1900, uS Patent 645,576. [Online]. Available: <http://www.google.com/patents/US645576>
- [7] —, “Apparatus for transmitting electrical energy.” Dec. 1 1914, uS Patent 1,119,732. [Online]. Available: <https://www.google.com/patents/US1119732>
- [8] J. L. Villa, J. Sallán, A. Llombart, and J. F. Sanz, “Design of a high frequency inductively coupled power transfer system for electric vehicle battery charge,” *Applied Energy*, vol. 86, no. 3, pp. 355 – 363, 2009. [Online]. Available: <http://www.sciencedirect.com/science/article/pii/S0306261908001359>
- [9] Z. Yang, W. Liu, and E. Basham, “Inductor modeling in wireless links for implantable electronics,” *IEEE Transactions on Magnetics*, vol. 43, no. 10, pp. 3851–3860, Oct 2007.
- [10] A. RamRakhyani, S. Mirabbasi, and M. Chiao, “Design and optimization of resonance-based efficient wireless power delivery systems for biomedical implants,” *IEEE Transactions on Biomedical Circuits and Systems*, vol. 5, no. 1, pp. 48–63, Feb 2011.
- [11] J. Lee and S. Nam, “Fundamental aspects of near-field coupling small antennas for wireless power transfer,” *IEEE Transactions on Antennas and Propagation*, vol. 58, no. 11, pp. 3442–3449, Nov 2010.

## Bibliography

- [12] Y. Jang and M. Jovanovic, "A contactless electrical energy transmission system for portable-telephone battery chargers," *Industrial Electronics, IEEE Transactions on*, vol. 50, no. 3, pp. 520–527, June 2003.
- [13] A. Kurs, A. Karalis, R. Moffatt, J. D. Joannopoulos, P. Fisher, and M. Soljacic, "Wireless power transfer via strongly coupled magnetic resonances," *Science*, vol. 317, no. 5834, pp. 83–86, 2007.
- [14] A. Karalis, J. Joannopoulos, and M. Soljacic, "Efficient wireless non-radiative mid-range energy transfer," *Annals of Physics*, vol. 323, no. 1, pp. 34 – 48, 2008, january Special Issue 2008. [Online]. Available: <http://www.sciencedirect.com/science/article/pii/S0003491607000619>
- [15] S. Ho, J. Wang, W. Fu, and M. Sun, "A comparative study between novel witricity and traditional inductive magnetic coupling in wireless charging," *IEEE Transactions on Magnetics*, vol. 47, no. 5, pp. 1522–1525, May 2011.
- [16] S. Cheon, Y.-H. Kim, S.-Y. Kang, M. L. Lee, J.-M. Lee, and T. Zyung, "Circuit-model-based analysis of a wireless energy-transfer system via coupled magnetic resonances," *IEEE Transactions on Industrial Electronics*, vol. 58, no. 7, pp. 2906–2914, July 2011.
- [17] M. Kiani and M. Ghovanloo, "The circuit theory behind coupled-mode magnetic resonance-based wireless power transmission," *IEEE Transactions on Circuits and Systems I: Regular Papers*, vol. 59, no. 9, pp. 2065–2074, Sept 2012.
- [18] W.-S. Lee, W.-I. Son, K.-S. Oh, and J.-W. Yu, "Contactless energy transfer systems using antiparallel resonant loops," *IEEE Transactions on Industrial Electronics*, vol. 60, no. 1, pp. 350–359, Jan 2013.
- [19] T. P. Duong and J.-W. Lee, "Experimental results of high-efficiency resonant coupling wireless power transfer using a variable coupling method," *Microwave and Wireless Components Letters, IEEE*, vol. 21, no. 8, pp. 442–444, Aug 2011.
- [20] T. C. Beh, M. Kato, T. Imura, S. Oh, and Y. Hori, "Automated impedance matching system for robust wireless power transfer via magnetic resonance coupling," *IEEE Transactions on Industrial Electronics*, vol. 60, no. 9, pp. 3689–3698, Sept 2013.
- [21] W. Niu, W. Gu, J. Chu, and A. Shen, "Coupled-mode analysis of frequency splitting phenomena in cpt systems," *Electronics Letters*, vol. 48, no. 12, pp. 723–724, June 2012.
- [22] J.-W. Kim, H.-C. Son, D.-H. Kim, K.-H. Kim, and Y.-J. Park, "Analysis of wireless energy transfer to multiple devices using cmt," in *Microwave Conference Proceedings (APMC), 2010 Asia-Pacific*, Dec 2010, pp. 2149–2152.
- [23] H. Haus and W. Huang, "Coupled-mode theory," *Proceedings of the IEEE*, vol. 79, no. 10, pp. 1505–1518, Oct 1991.

- [24] X. Wei, Z. Wang, and H. Dai, "A critical review of wireless power transfer via strongly coupled magnetic resonances," *Energies*, vol. 7, no. 7, pp. 4316–4341, 2014. [Online]. Available: <http://EconPapers.repec.org/RePEc:gam:jeners:v:7:y:2014:i:7:p:4316-4341:d:37856>
- [25] E. Shamonina, V. Kalinin, K. Ringhofer, and L. Solymar, "Magneto-inductive waveguide," *Electronics Letters*, vol. 38, no. 8, pp. 371–373, Apr 2002.
- [26] E. Shamonina, V. A. Kalinin, K. H. Ringhofer, and L. Solymar, "Magnetoinductive waves in one, two, and three dimensions," *Journal of Applied Physics*, vol. 92, no. 10, pp. 6252–6261, 2002. [Online]. Available: <http://scitation.aip.org/content/aip/journal/jap/92/10/10.1063/1.1510945>
- [27] L. Solymar and E. Shamonina, *Waves in Metamaterials*. OUP Oxford, 2009.
- [28] M. Wiltshire, J. Hajnal, J. Pendry, D. Edwards, and C. Stevens, "Metamaterial endoscope for magnetic field transfer: near field imaging with magnetic wires," *Opt. Express*, vol. 11, no. 7, pp. 709–715, Apr 2003. [Online]. Available: <http://www.opticsexpress.org/abstract.cfm?URI=oe-11-7-709>
- [29] C. Stevens, C. Chan, K. Stamatis, and D. Edwards, "Magnetic metamaterials as 1-d data transfer channels: An application for magneto-inductive waves," *IEEE Transactions on Microwave Theory and Techniques*, vol. 58, no. 5, pp. 1248–1256, May 2010.
- [30] C. Stevens, "Power transfer via metamaterials," *Computers, Materials and Continua*, vol. 33, no. 1, pp. 1–18, 2013.
- [31] —, "Magnetoinductive waves and wireless power transfer," *IEEE Transactions on Power Electronics*, vol. PP, no. 99, pp. 1–1, 2014.
- [32] B. Wang and K. H. Teo, "Metamaterials for wireless power transfer," in *Antenna Technology (iWAT), 2012 IEEE International Workshop on*, March 2012, pp. 161–164.
- [33] B. Wang, K. H. Teo, T. Nishino, W. Yerazunis, J. Barnwell, and J. Zhang, "Wireless power transfer with metamaterials," in *Antennas and Propagation (EUCAP), Proceedings of the 5th European Conference on*, April 2011, pp. 3905–3908.
- [34] C.-S. Wang, G. Covic, and O. Stielau, "Power transfer capability and bifurcation phenomena of loosely coupled inductive power transfer systems," *IEEE Transactions on Industrial Electronic*, vol. 51, no. 1, pp. 148–157, Feb 2004.
- [35] Z. N. Low, R. Chinga, R. Tseng, and J. Lin, "Design and test of a high-power high-efficiency loosely coupled planar wireless power transfer system," *IEEE Transactions on Industrial Electronics*, vol. 56, no. 5, pp. 1801–1812, May 2009.

## Bibliography

- [36] L. Sandrolini, U. Reggiani, and G. Puccetti, "Analytical calculation of the inductance of planar zig-zag spiral inductors," *Progress in Electromagnetics Research*, vol. 142, pp. 207–220, 2013.
- [37] C. Chan and C. Stevens, "Two-dimensional magneto-inductive wave data structures," in *Proc. 5th European Conf. on Antennas Prop. (EUCAP)*, April 2011, pp. 1071–1075.
- [38] R. R. A. Syms, I. R. Young, and L. Solymar, "Low-loss magneto-inductive waveguides," *Journal of Physics D: Applied Physics*, vol. 39, no. 18, p. 3945, 2006.
- [39] Y. Zhang, Z. Zhao, and K. Chen, "Frequency-splitting analysis of four-coil resonant wireless power transfer," *IEEE Transactions on Industry Applications*, vol. 50, no. 4, pp. 2436–2445, July 2014.
- [40] S. Mohan, M. del Mar Hershenson, S. Boyd, and T. Lee, "Simple accurate expressions for planar spiral inductances," *Solid-State Circuits, IEEE Journal of*, vol. 34, no. 10, pp. 1419–1424, Oct 1999.
- [41] D. Ellstein, B. Wang, and K. H. Teo, "Accurate models for spiral resonators," in *Radar Conference (EuRAD), 2012 9th European*, Oct. 2012, pp. 461–464.
- [42] Y. Cao, R. Groves, X. Huang, N. Zamdmmer, J.-O. Plouchart, R. Wachnik, T.-J. King, and C. Hu, "Frequency-independent equivalent-circuit model for on-chip spiral inductors," *Solid-State Circuits, IEEE Journal of*, vol. 38, no. 3, pp. 419–426, March 2003.
- [43] U.-M. Jow and M. Ghovanloo, "Design and optimization of printed spiral coils for efficient transcutaneous inductive power transmission," *Biomedical Circuits and Systems, IEEE Transactions on*, vol. 1, no. 3, pp. 193–202, Sept. 2007.
- [44] —, "Modeling and optimization of printed spiral coils in air, saline, and muscle tissue environments," *Biomedical Circuits and Systems, IEEE Transactions on*, vol. 3, no. 5, pp. 339–347, Oct. 2009.
- [45] A. Radkovskaya, O. Sydoruk, M. Shamonin, C. J. Stevens, G. Faulkner, D. J. Edwards, E. Shamonina, and L. Solymar, "Transmission properties of two shifted magnetoinductive waveguides," *Microwave and Optical Technology Letters*, vol. 49, no. 5, pp. 1054–1058, 2007. [Online]. Available: <http://dx.doi.org/10.1002/mop.22344>
- [46] L. Sandrolini, U. Reggiani, G. Puccetti, and Y. Neau, "Equivalent circuit characterization of resonant magnetic coupling for wireless transmission of electrical energy," *International Journal of Circuit Theory and Applications*, vol. 41, no. 7, pp. 753–771, July 2013. [Online]. Available: <http://dx.doi.org/10.1002/cta.1873>
- [47] A. Sample, D. Meyer, and J. Smith, "Analysis, experimental results, and range adaptation of magnetically coupled resonators for wireless power transfer," *Industrial Electronics, IEEE Transactions on*, vol. 58, no. 2, pp. 544–554, Feb 2011.

- [48] MATLAB, *version 8.0.0 (R2012b)*. Natick, Massachusetts: The MathWorks Inc., 2012.
- [49] C. Sonntag, E. Lomonova, and J. Duarte, "Implementation of the neumann formula for calculating the mutual inductance between planar pcb inductors," in *18th International Conf. on Electrical Machines, 2008. ICEM 2008*, Sept. 2008, pp. 1–6.
- [50] Scilab Enterprises, *Scilab: Free and Open Source software for numerical computation*, Scilab Enterprises, Orsay, France, 2012. [Online]. Available: <http://www.scilab.org>
- [51] J. C. for Guides in Metrology, "Jcgm 100: Evaluation of measurement data - guide to the expression of uncertainty in measurement," JCGM, Tech. Rep., 2008.
- [52] *Sonnet Software, version 14.54*. North Syracuse, NY: Sonnet Software Inc., 2014.
- [53] E. G. J. Power, S. Kelly and M. O'Neill, "An investigation of on-chip spiral inductors on a 0.6um bimos technology for rf applications," in *1999 International Conference on Microelectronic Test Structures*. Goteborg, Sweden: ICMTS 1999, March 15-18 1999, pp. 18–23.
- [54] B. S. S. Nemer and B. Bayard, "Modelling resonance frequencies of a multi-turn spiral for metamaterial applications," *Progress In Electromagnetics Research C*, vol. 20, pp. 31–42, 2011.
- [55] B. Wang, W. Yerazunis, and K. H. Teo, "Wireless power transfer: Metamaterials and array of coupled resonators," *Proceedings of the IEEE*, vol. 101, no. 6, pp. 1359–1368, June 2013.
- [56] G. Grandi, M. A. Kazimierczuk, M.K., and U. Reggiani, "Stray capacitances of single-layer solenoid air-core inductors," *Industry Applications, IEEE Transactions on*, vol. 35, no. 5, pp. 1162–1168, Sep./Oct. 1999.
- [57] U. Reggiani, G. Grandi, G. Sancineto, M. Kazimierczuk, and A. Massarini, "High-frequency behavior of laminated iron-core inductors for filtering applications," in *The 15th Annual IEEE Applied Power Electronics Conference and Exposition - APEC 2000*, vol. 2, Feb. 6-10 2000, pp. 654–660.
- [58] C. Neagu, H. Jansen, A. Smith, J. Gardeniers, and M. Elwenspoek, "Characterization of a planar microcoil for implantable microsystems," *Sensors and Actuators A: Physical*, vol. 62, no. 1-3, pp. 599–611, 1997. [Online]. Available: <http://doc.utwente.nl/14236/>
- [59] *Finite Element Method Magnetics, femm 4.2*. David Meeker, 2013.
- [60] A. E. Ruehli, "Inductance calculations in a complex integrated circuit environment," *IBM J. Res. Dev.*, vol. 16, no. 5, pp. 470–481, Sep. 1972.

## Bibliography

- [61] L. Sandrolini, U. Reggiani, and G. Puccetti, "Inductance characterization for flat spiral inductors with uniform and nonuniform zig-zag arms," in *The 30th International Review of Progress in Applied Computational Electromagnetics*, March 23-27 2014.
- [62] E. Rosa and U. S. N. B. of Standards, *The self and mutual inductances of linear conductors*, ser. Bulletin of the Bureau of Standards. U.S. Dept. of Commerce and Labor, Bureau of Standards, 1908.
- [63] C. Hoer and C. Love, "Exact inductance equations for rectangular conductors with applications to more complicated geometries," *J. Res. Nat. Bur. Stand. Sec. C: Eng. Inst.*, vol. 69C, pp. 127–137, 1965.
- [64] C. Lee, Y. Su, and S. Hui, "Printed spiral winding inductor with wide frequency bandwidth," *IEEE Transactions on Power Electronics*, vol. 26, no. 10, pp. 2936–2945, Oct. 2011.
- [65] S. Wang, "On the relationship between dielectric dissipation-factor and angular frequency," in *Properties and Applications of Dielectric Materials, 1991, Proceedings of the 3rd International Conference on*, vol. 2, July 1991, pp. 1080–1082.
- [66] C. Blair and J. C. Rautio, "Rfid design using em analysis," in *Applications and Technology Conference (LISAT), 2010 Long Island Systems*, May 2010, pp. 1–6.
- [67] G. Puccetti, U. Reggiani, and L. Sandrolini, "Experimental analysis of wireless power transmission with spiral resonators," *Energies*, vol. 6, no. 11, pp. 5887–5896, 2013.
- [68] A. Reatti and M. Kazimierczuk, "Comparison of various methods for calculating the ac resistance of inductors," *IEEE Transactions on Magnetics*, vol. 38, no. 3, pp. 1512–1518, May 2002.
- [69] M. Bartoli, N. Noferi, A. Reatti, and M. K. Kazimierczuk, "Modelling winding losses in high-frequency power inductors," *Journal of Circuits, Systems and Computers*, vol. 05, no. 04, pp. 607–626, 1995. [Online]. Available: <http://www.worldscientific.com/doi/abs/10.1142/S0218126695000370>
- [70] R. Wojda and M. Kazimierczuk, "Optimum foil thickness of inductors conducting dc and non-sinusoidal periodic currents," *Power Electronics, IET*, vol. 5, no. 6, pp. 801–812, July 2012.
- [71] M. Bartoli, N. Noferi, A. Reatti, and M. Kazimierczuk, "Modeling litz-wire winding losses in high-frequency power inductors," in *Power Electronics Specialists Conference, 1996. PESC '96 Record., 27th Annual IEEE*, vol. 2, Jun 1996, pp. 1690–1696 vol.2.
- [72] R. Wojda and M. Kazimierczuk, "Winding resistance of litz-wire and multi-strand inductors," *Power Electronics, IET*, vol. 5, no. 2, pp. 257–268, Feb 2012.

- [73] —, “Analytical optimization of solid round-wire windings,” *IEEE Transactions on Industrial Electronics*, vol. 60, no. 3, pp. 1033–1041, March 2013.
- [74] S. GS., “Proximity effect in systems of parallel conductors,” *Journal of Applied Physics*, vol. 43, no. 5, pp. 2196–2203, 1972.
- [75] P. F and R. T, “Spiral antenna with zigzag arms to reduce size,” Jul. 8 1969, uS Patent 3,454,951.
- [76] C. Paul, *Inductance: Loop and Partial*. Wiley, 2010.
- [77] Z. Piatek and B. Baron, “Exact closed form formula for self inductance of conductor of rectangular cross section,” *Progress In Electromagnetics Research M*, vol. 26, pp. 225–236, 2012.
- [78] G. A. Campbell, “Mutual inductances of circuits composed of straight wires,” *Phys. Rev.*, vol. 5, pp. 452–458, Jun 1915.
- [79] M. Kamon, M. Tsuk, and J. White, “Fasthenry: a multipole-accelerated 3-d inductance extraction program,” *IEEE Transactions on Microwave Theory and Techniques*, vol. 42, no. 9, pp. 1750–1758, Sept 1994.